

UNIVERSITY OF CALIFORNIA

SANTA CRUZ

**A SMALL SCALE REACTION WHEEL PROTOTYPE FOR ATTITUDE
STABILIZATION OF CUBESATS**

A thesis submitted in partial satisfaction
of the requirements for the degree of

MASTER OF SCIENCE

in

ELECTRICAL ENGINEERING

by

BRADLEY WATANABE

December 2013

The Thesis of BRADLEY WATANABE
is approved:

Professor Mark Karpenko
Naval Postgraduate School

Professor Renwick E. Curry

Professor Gabriel Hugh Elkaim, Chair

Tyrus Miller
Vice Provost and Dean of Graduate Studies

Table of Contents

List of Figures	vi
List of Tables	x
Abstract	xi
Acknowledgements	xii
1 Introduction	1
1.1 Motivation	1
1.1.1 Purpose of Satellites	1
1.1.2 Cost of Launch	2
1.1.3 Purpose of Attitude Control	4
1.2 Criteria/Specifications	4
1.2.1 Objectives & Scope	5
1.3 Literature Review	7
1.4 Evaluation and Prototyping	9
1.5 Thesis Structure	10
2 Background	11
2.1 Magnetic Field Actuators	11
2.1.1 Permanent Magnets Applications	15
2.1.2 Torquer Applications	15
2.2 Reaction Wheels	16
2.2.1 Reaction Wheel Applications	17
2.3 Control Moment Gyroscopes	18
2.3.1 Control Moment Gyroscope Applications	19
2.4 Actuation Summary	20
3 Hardware - Design Objectives	21
3.1 Size Constraints	21
3.1.1 Reaction Wheel Array Constraints	21

3.1.2	Motor Geometry	22
3.1.3	Orthogonal Reaction Wheel Configurations	22
3.1.4	Square Pyramid	24
3.1.5	Geometry Analysis	24
3.1.6	Brushless DC Motors	26
3.2	Candidate Flight Controllers	28
3.2.1	SLUGS	30
3.2.2	ArduPilot	31
3.2.3	MatrixPilot	32
3.2.4	Flight Controller Evaluation	32
3.3	Main Control System Architecture	33
3.3.1	Processors Specifics	35
3.3.2	Power Rails and Regulation	37
3.4	Shield Concept	39
3.4.1	Interchangeable Hardware	39
3.5	SENSOR Shield	40
3.5.1	SENSOR Shield Mating	42
3.6	Summary	43
4	Attitude Estimation	44
4.1	Transformation Matrix	47
4.2	Renormalization	49
4.3	Complementary Filter	50
4.3.1	Yaw Compensation	51
4.3.2	Roll/Pitch Compensation	52
4.3.3	Feedback Controller	54
4.4	Summary	55
5	Brushless DC Motor Control Shield	56
5.0.1	MOSFETs	57
5.0.2	High/Low Side Gate Drive	59
5.1	Current Sensing	60

5.1.1	Hall Effect Current Sensing	61
5.1.2	Shunt Resistor Current Sensing	62
5.1.3	High Side Current Sensing	63
5.2	Noise and Isolation	65
5.2.1	Noise	65
5.2.2	Isolation	67
5.3	BLDC Motor Commutation	69
5.3.1	DRV8332 Specific Motor Control	70
5.3.2	Reading the Hall Sensors	72
5.3.3	Speed Control	73
5.4	Summary	76
6	System Checkout & Evaluation	77
6.1	Power Requirements	77
6.2	Volume	78
6.3	Control Accuracy	80
6.3.1	Attitude Estimation Accuracy	81
6.3.2	Experimental Controller Design	83
6.3.3	Experimental Control Response	85
7	Conclusions & Future Work	90
7.1	Conclusions	90
7.2	Future Work	91
8	Appendix	93
8.1	AECS Pin Allocation	93
8.2	BLDC Specificaitons	95
8.3	Experimental Power Consumption	96
Nomenclature		97
References		99

List of Figures

1	The price/pound to launch a satellite from 1990-2000 [21].	2
2	Depiction of CubeSats as a secondary payload and possible ridesharing configurations, with the primary payload in blue and CubeSat launchers in yellow [39]. . .	3
3	CAD model of the Poly-PicoSatellite Orbital Deployer (P-POD) used to house and launch 1U - 3U CubeSats [33].	5
4	CAD models of the Colony I Bus and Attitude Controller.	7
5	CAD model of FalconSat-7 using the Boeing Colony II Bus [35].	8
6	CAD model of NASA's phoneSat 2.0, which operates using an Android phone [46].	9
7	Cross-sectional view of the control hardware testbed used to demonstrate attitude control about the yaw axis.	10
8	The Earth's Magnetic Field Declination lines [10].	11
9	The Earth's Magnetic Field intensity [10].	12
10	Image of a CubeSat Magnetic Torque Rod [7].	13
11	Application of the Conservation of Momentum is used to rotate the CubeSat (gray box) via control of the reaction wheel in blue.	17
12	CMG concept of operation: (a) direction of momentum vector L before gimballing; (b) torque output due to gimbol motion [62]	18
13	Images of Small Satellites CMGs	19
14	The control hardware was designed to fit within the Pumpkin CubeSat Skeletons [2].	22
15	Reaction Wheel Layout similar to that of MAI-101 used on the Colony I Bus [40].	23
16	Motor layout similar to that of SwissCube which allows the moment of inertia of the flywheel to be maximized [49].	24
17	Pyramid design with 4 reaction wheels all 45° off vertical allowing for a redundant actuator configuration.	25
18	Simplified diagram of a single pole BLDC motor showing how the coils interact with the rotor magnet (on the left). On the right, the flow of current is shown for each of the coils [50].	27

19	The SLUGS Autopilot with dual processors and the Analog Devices sensor cube [79].	30
20	A shield (blue) mounted on the ArduPilot (red) demonstrating that all the electronics do not need to be placed on the autopilot [25].	31
21	The MatrixPilot hardware options showing that only a limited number of chips are necessary for the control electronics.	32
22	Control hardware named the main board, which utilizes a header system to add supporting electrical shields	34
23	Main board architecture block diagram showing the AECS hardware in Fig. 22 and their connections with the Control and Sensor Shields.	35
24	Block Diagram of a generic linear regulator [90].	37
25	Equivalent functional diagram of a switching regulator [95].	38
26	Top of the SENSOR Shield board showing the sensor breakout boards (red); used to supply the supporting electronics to the SENSOR DSC	41
27	Main board hardware showing the mating connections between the sensor shield and main board.	42
28	CubeSat body frame coordinate system.	44
29	Space based coordinate systems [9]	45
30	Attitude Estimator Block Diagram showing the flow of data; extracting the rotation rate from the gyroscopes and converting the data into the system's orientation [86].	46
31	Diagram of the yaw rotation and error on the x-y plane (green) [86].	52
32	Diagram of roll and pitch. Pitch rotation is on the x-z plane (yellow) and roll rotation is on the y-z plane in (purple) [86].	53
33	BLDC Control Shield Block Diagram, showing the flow of data in the BLDC control loop.	56
34	Photo of the BLDC Control Shield with the main board mounted.	57
35	BLDC control with n-channel MOSFETs (a); showing how power is supplied to the motor using the high/low side MOSFETs (b)	58
36	Diagram of microcontroller (purple), High/Low Side Driver (blue), and MOSFETs illustrating the bootstrap capacitor [57].	60

37	Hall Effect sensors measure the current flowing through a wire by observing the magnetic field generated by the flow of current as described by Ampere's Law [75].	61
38	Hall effect sensor diagram showing how the introduction of a magnetic field (B) creates a differential voltage in the hall material [53].	62
39	High and low side shunt resistor current sensing diagrams showing that the difference between the two methods is the location of the shunt resistor with respect to the load [75].	63
40	High side current sensing block diagram showing the high voltage measured at the inputs of the OP Amp [75].	64
41	Simplified circuit exemplifying inductive kickback, when the switch is opened a large spike is generated by the inductor [30].	65
42	Example of inductive kickback, the inductive kickback creates the noise on the control signals [55].	66
43	A simplified block diagram showing the connections between the microcontroller and the BLDC motor.	67
44	Eagle Layout of the top BLDC Shield, showing an enlarged view of the mecca ground, indicated by the blue circle.	68
45	Image of the EC45 Flat Maxon Motor used on the hardware testbed. This motor was chosen due to the built in flywheel, making fabrication easier [38].	69
46	Simulated hall effect sensor signals produced by the control hardware, these signals were used to simulate the motor spinning and verify proper commutation of the motor's control signals.	71
47	PWM and reset signals using simulated hall sensor signals (Fig. 46).	72
48	Sample Pulse Width Modulation (PWM) signal [8].	74
49	Timing diagram showing hall sensors output and PWM signals [24].	75
50	Open loop reaction wheel speed response for a 9.6V step input.	75
51	Model of control hardware layout with reaction wheels and magnetic torquers, showing that ample space remains for the control hardware.	79
52	Different views of hardware depicting the flight control actuators (reaction wheels in Blue and Torquers in red).	79

53	Photo of the testbed used to demonstrate yaw control; showing the reaction wheel is mounted directly above the rotating axis to maximize the transfer of angular momentum.	80
54	Depiction of the estimated yaw angle in blue and the actual yaw angle in red. . .	82
55	Depiction of the estimated yaw angle error corresponding to Fig. 54.	82
56	Block diagram of the implemented yaw controller showing the feedback control loop implemented on the control hardware.	84
57	Diagram showing the three steps in the testbed variable analysis. Where step A is a 2° disturbance input in the clockwise direction, step B is a 14° disturbance input in the counter-clockwise direction, and step C is the regulating response to the disturbance inputs.	85
58	Experiment results showing the yaw orientation of the the testbed in response to a 14° disturbance input. The results show a steady state error of 2°	86
59	Experiment results showing the motor angular velocity showing that the motor is constantly decreasing in speed trying to reduce the steady state error to zero. .	87
60	Experiment results showing the motor current consumption which resembles the motor speed curve. From the diagram it can be seen that the motor is operating well below its maximum rating (23A)	87
61	Experiment results showing the feedback control signal commanded by the microcontroller. Similar to Fig. 59 - 60, it can be seen that the controller is trying to slow down the motor to reduce the steady state error.	88
62	Image of the testbed showing the slip ring and wires in yellow connected to the control hardware. The slip ring and wires cause the steady state error on the testbed.	89
63	Data comparing the applied duty cycle and the current consumption of the motor.	96

List of Tables

1	Table summarizing some small satellite actuators showing the accuracy of reaction wheels [91].	6
2	Summary of the CubeSat Reaction Wheel Array Design Criteria	7
3	Motor Geometry Summary	25
4	Reaction Wheel Summary	26
5	Clockwise Brushless DC Motor Commutation (high and low signals are reversed for counter-clockwise operation)	70
6	Clockwise Brushless DC Motor Commutation using DRV8332.	73
7	Summary of the Attitude Control System Criteria	77
8	Power Consumption Table	77
9	Space Sensors Power Consumption Table	78
10	AECS's Pin Allocation	93
11	EC45Flat Motor Pinout	95
12	Maxon EC45Flat Summary	95
13	Faulhaber 1509 Summary	95

Abstract

A Small Scale Reaction Wheel Prototype for Attitude Stabilization of CubeSats

by

Bradley Watanabe

This thesis has the objective of creating a reaction wheel based attitude control system for a 3U CubeSat. Conforming to the 3U CubeSat form factor, at least half of the 3U design will be available for the payload, leaving the other half for the flight hardware and electronics. The Main Control System (main board) was designed as a universal autopilot with fully adaptable hardware, making it possible to rapidly prototype control systems for a wide variety of platform. Since the Attitude Estimation and Control System (AECS) project is still in the prototyping stages, the main aboard was the ideal hardware platform to design the AECS project around.

This project aims to establish a functional prototype that can be used as a building block to a university grade reaction wheel based attitude control system. A few commercial reaction wheel based systems are available on the market. However, they limit the user to design around their attitude control algorithms when in reality it is more efficient to design the control system around the payload. It is believed that in order to advance the field of CubeSats, a more precise actuation system is required, hence the need for a reaction wheel based attitude control system. This allows the developer to add and remove hardware as designated by the mission objectives. Use of reaction wheels provides quicker and more accurate actuation enabling CubeSats to perform more complex tasks. The use of reaction wheels allows the platform to better handle disturbances.

The thesis demonstrates a fully integrated system with (1) accurate attitude estimation and (2) control of a single reaction wheel to manipulate the yaw orientation of the CubeSat mockup. It is shown that the system conforms to the 1.5U size constraints and operates within the average power absorption capacity of a 3U CubeSat solar array.

Acknowledgements

A special thanks to:

Gabriel Elkaim PhD

Ren Curry PhD

Mark Karpenko PhD

I. Michael Ross PhD

Robert Casey MS

Max Dunne BS

Taylor Watanabe BS

UC Santa Cruz

Naval Postgraduate School

I would like to extend my thanks to my thesis advisor and professor Gabriel Elkaim for this mentorship and introducing me to the fields of robotic and autonomous systems. It was Professor Elkaim that gave me the opportunity to pursue research into such an exciting field. To Ren Curry for his development of the SLUGS attitude control which aided in the development of the AECS algorithms, as well as his insight into space applications of the attitude estimation system. To Mark Karpenko for this guidance in the development of the AECS hardware and initial motivation for a CubeSat based reaction wheel attitude control system. He is also responsible for making me see the bigger picture and not getting caught up on the smaller details. To Michael Ross for providing a research environment committed to education and research at the Naval Postgraduate School in Monterey California. To Max Dunne and Robert Casey for their assistance in the hardware and software development. Without their expertise development of the AECS testbed would not have been possible. To Autonomous System Laboratory for their assistance with some many of the detail of this project. Without their expertise in the many fields that this thesis covers a functional testbed would not have been possible to fabricate. To friends and family without their support this thesis would have never been possible.

1 Introduction

This thesis aims to develop a prototype reaction wheel based Attitude Estimation and Control System (AECS) conforming to the constraints of a 3U CubeSat. CubeSat are constrained by their size, weight, and power intake. A few reaction wheel based CubeSats project have overcome these challenges some examples being the Pumpkin Colony I Bus, the Boeing Colony II Bus and NASA PhoneSat. Also companies such as SSBV [14] and Blue Canyon Technology [16] have developed an enclosed reaction wheel for use in CubeSats. That being said, it is the goal of this thesis to take the initial steps to conceive an off the shelf CubeSat Attitude Control System using reaction wheels. Reaction wheels were chosen because of the greater control torque and accuracy. However, magnetic torque rods are a popular actuator because of their small form factor and ease of operation.

1.1 Motivation

Over the past decade, CubeSats have become extremely popular because of their low launch and development costs. It is due to these low launch and development cost that individuals found other more elaborate uses for small satellites; for instance the Kestrel Eye project proposed by the US Army. The Kestrel Eye project aims to produce a satellite imaging constellation to relay visual data to ground based forces [93]. Satellite constellations for such applications could be exceedingly costly for larger satellites. However, CubeSat and other small satellites offer a cheaper solution in terms of launch and development costs.

1.1.1 Purpose of Satellites

According to the UCS¹, about a thousand operational satellites are orbiting the Earth [44]. These satellites have missions ranging from military applications to science to communication. However, even with their different applications most satellites have a few common characteristics: a Central Processing Unit (CPU), power source, communication module, and some form of attitude controller. Without any one of the four traits the satellite could be kept from completing its mission. The CPU is used for processing environmental data and executing the mission objective. This onboard processor is supported by the system power source, which

¹Union of Concerned Scientists

supplies the flight electronics and actuators. In space systems communication is extremely important, without which data collected during the mission cannot be relayed to the ground station. Attitude control is a necessary component of the satellite. Without attitude control satellites would be unable to complete their missions. Communications satellites are used to relay data, but without attitude control the satellite's antenna wont be pointing in the correct direction, disrupting communications. Research satellites can be used to observe neighboring galaxies, but without attitude control it would be impossible to point the satellite towards the object of interest. Most satellites rely on solar power and due to the material properties of solar cells, their efficiency is greatly reduced when not pointed directly at the Sun. Without the use of attitude controllers it would be impossible to orient the solar cells with the Sun.

1.1.2 Cost of Launch

Many satellites have been put into space, but this comes at great cost. Fig. 1 depicts the trends of cost per pound to get a satellite into space from 1990-2000. The average cost in 2000 to launch a satellite into space was about \$10,000/lb or about \$22,000/kg [21]. However, launch costs are fixed per launch, regardless of payload utilized. It is cost-effective to load the rocket to full capacity. An example of an actual launch was the Landsat Data Continuity Mission

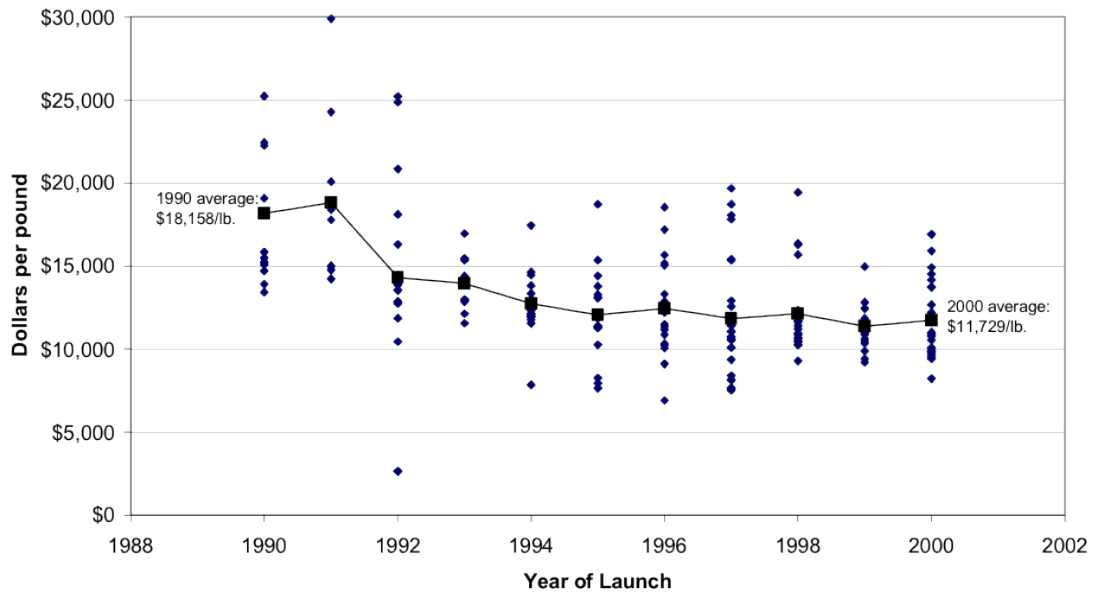


Figure 1: The price/pound to launch a satellite from 1990-2000 [21].

(LDCM). The LDCM was launched on February 11, 2013 using an AtlasV401 rocket, which had a payload capacity of 5,000kg while the LDCM weighs in at 2,623kg [29]. The estimated launch cost for the LDCM mission was estimated at \$90 Million [29]. If the LDCM was the only payload launched the cost per kg would be about \$34,000/kg. In order to minimize the launch cost a few options exist, (1) reduce the weight of the satellite and use a smaller rocket or (2) add another satellite to the rocket payload (known as ridesharing). Reducing the weight of the satellite is a tradeoff, since it reduces the amount of instruments that can be carried on the satellite. Conversely it diminishes the size of the rocket needed. Ideally, one would reduce the size of the satellite while keeping the same or similar capabilities. The other option, launching with other satellites, is an option more commonly explored because it distributes the burden of the launch cost among several satellites.

Reducing the size of satellites and ridesharing have led to increased interest in SmallSats including PicoSats, also known as CubeSats. CubeSats are restricted to a 10 cm x 10 cm x 10 cm form factor and are restricted to weights less than 1kg [68]. Due to their limited size and weight, they are much more economical to launch and are capable of launching on smaller rockets. Their small form factor also allows them to be added as a secondary payload on many rockets (see Fig. 2). Ridesharing is popular because of the extra payload capacity and the fixed cost of launch. By using SmallSats to utilize the extra payload capacity it becomes more cost effective to send satellites into space. But, what can CubeSats accomplish and what makes them

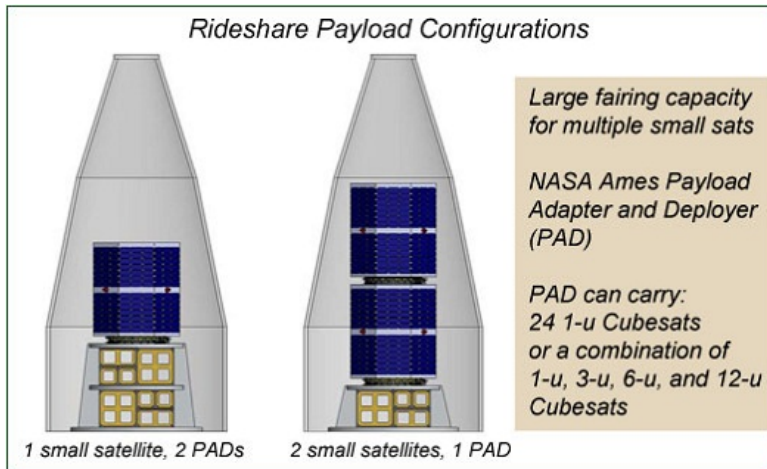


Figure 2: Depiction of CubeSats as a secondary payload and possible ridesharing configurations, with the primary payload in blue and CubeSat launchers in yellow [39].

different from space debris?

According to Dr. Jordi Puig-Suari, at the 2012 CubeSat Conference, CubeSats are a way of pushing the technological envelope [27]. By constricting the size of satellites, designers are required to find novel solutions to improve and reduce the size of satellite. One such example is using a metal roll up tape measure as an antenna [13]. This provides a cheap, compact and robust design for a satellite antenna.

1.1.3 Purpose of Attitude Control

Many CubeSat mission require some form of attitude stabilization or control. Attitude control provides the ability to command the orientation of a platform, in terms of its roll, pitch, and yaw. Attitude control is done with the use of Control Moment Gyroscopes, Reaction Wheels, Magnetic Torque Rods, Gravity Booms, etc. In larger satellites, Control Moment Gyroscopes or CMGs are the actuator of choice because of their larger torque to power ratio [94]. In smaller satellites actuators such as magnetic torque rods or torquers are the actuator of choice due to their small size, form factor, and simplicity. However, there is a tradeoff; the smaller torquers are not nearly as powerful as the larger CMG and on the order of ten times less accurate [91]. The torquers also have another disadvantage; they are only effective in Low Earth Orbit (LEO) and can disrupt the satellite's onboard sensors when activated.

Reaction wheels have a much smaller torque to power ratio compared to CMG's, but less torque is required due to the small size and mass of CubeSats. Using reaction wheels over CMG's reduces the mechanical complexity of the actuator. Only a few CubeSats have incorporated reaction wheels to date.

1.2 Criteria/Specifications

Any new hardware system for CubeSat attitude estimation is constrained by the form factor of the CubeSat, which also limits the power intake. Power is an issue because solar energy is the only source of power on the CubeSat and with a limited surface area this becomes a problem. Some CubeSats have such short operational lifetimes solar panels becomes less necessary, such as the QbX1 and QbX2 CubeSat which were operations for only 29 and 39 days respectively [88]. Other CubeSats like phoneSat 1.0 were not equipped with solar panels [88]. Solutions exist to increase the solar panel surface area, but the basic solar panel layout will be

used in evaluating the system power requirements. The power supplied by the solar panels is consumed primarily by the attitude control actuators: the torquers and reaction wheels. These specifications are explored in more detail in the following sections.

1.2.1 Objectives & Scope

Currently the constraints on CubeSats are dictated by the CubeSat launchers dimensional restrictions. CubeSats have been in development for over 10 years and several different CubeSat launchers have been developed. However, the original standards were developed by Cal Poly San Luis Obispo and Stanford University [68]. A CubeSat launcher called the Poly- PicoSatellite Orbital Deployer or P-POD was also defined in the CubeSat Standards, as seen in Fig. 3. CubeSats can be broken down into UNITS, which are 10 cm x 10 cm x 10 cm cubes. The P-POD is capable of hauling three 1U CubeSats or any other arrangement adding up to 3U. Recently several other manufactures have created their own CubeSat launchers. NASA has created a larger launcher capable of launching a 6U CubeSat. Even a 50U CubeSat launcher is being developed, called the QB50, set to launch in April 2015 [31].

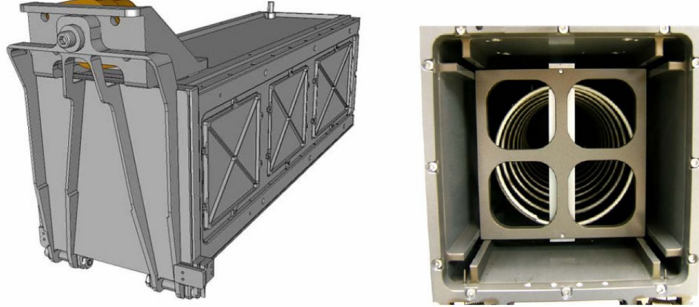


Figure 3: CAD model of the Poly-PicoSatellite Orbital Deployer (P-POD) used to house and launch 1U - 3U CubeSats [33].

Due to the size of the launchers, the size of many CubeSat missions have been and will be limited to 3U or smaller. The most popular sized CubeSats are the 1U and 3U versions [81]. Given these two options and the fact that an added attitude controller will require more space, this project is aimed to establish an attitude controller for a 3U CubeSat, dedicating 1-1.5U of the CubeSat to the attitude controller. The 1-1.5U is required because of the reaction wheels and their associated control electronics. This leaves 1.5-2U of available space for the CubeSat payload. It should be noted that the 1-1.5U dedicated to the attitude controller does not include

Method	Accuracy (deg)	Pros	Cons
Spin Stabilization	0.1-1	passive, simple, cheap	Inertially Oriented
Gravity Gradient	1-5	passive simple cheap	Central Body Oriented
Magnetic Torquers	1-2	cheap	slow, LEO only
Reaction Wheels	0.001-1	precise, fast slew	expensive, weight

Table 1: Table summarizing some small satellite actuators showing the accuracy of reaction wheels [91].

the batteries, this is assumed to be within the CubeSat payload.

The control hardware is designed to provide the maximum amount of accuracy, by using reaction wheels to orient the platform. A summary of some smallSat actuation methods [91] is summarized in Table 1, by Kristian Svartveit of NTNU. The most important comparison in Table 1 is between the magnetic torquers and reaction wheels. Magnetic torquers are currently a popular actuator due to their small size. However, reaction wheels offer greater torque and more precise control.

In order to prove that a reaction wheeled system is superior to a magnetic torque rod based attitude control system, it must be demonstrated that the accuracy of the reaction wheel system is greater than 1° . Magnetic torque rods only have an accuracy of $1-2^\circ$ while reaction wheels have a theoretical accuracy of $0.001-1^\circ$. If an accuracy of at least 1° is not achieved, then it will weaken the argument for reaction wheels. Evaluation of the control accuracy will only test the yaw axis due to the constraints of the testbed. While testing the attitude control system on Earth, forces and frictions not relevant while in space will be present, due to the limitations of the testbed. Due to these constraints, oversized actuators were chosen to compensate for the terrestrial limitations.

The AECS is also constraint on system power. Clyde-Space states, a 3U CubeSat can expect its solar panels to absorb 4.9W of power on average [54]. It will be the goal of this project to design a system that uses less than 4.9W. The 4.9W power goal was chosen because Clyde Space has calculated that their system is capable of collection 20.8W, therefore reaching the 4.9W goal allows the user to have an ample power reserve if the upgraded solar panel system is used. The power goals was evaluated using small high efficiency actuators; however, due to the limitation of the testbed, over sized and over powered motors will be used to demonstrate system control on the testbed. However, the smaller more efficient motors will be used for space

applications; therefore, the limitations on power will be more closely related to the attitude control hardware using the proposed high efficiency motors, not the testing motors. A summary of the design criteria can be found in Table 2

Design Criteria	Requirement
Power Consumption	< 4.9 Watts
Hardware Displacement	$\leq 1.5U$
Control Accuracy	$\leq 1^\circ$

Table 2: Summary of the CubeSat Reaction Wheel Array Design Criteria

1.3 Literature Review

At this time a few CubeSat reaction wheel systems show potential, specifically three projects from different manufacturers. Two of the projects are associated with the Colony Bus project [88] and the other part of NASA's CubeSat initiative [13]. The Colony I Bus has a long list of successful launches, the first launch being QbX1 and QbX2, which were launched using a Falcon 9 rocket in August 2010 [41]. The first Colony II Bus was launched using an Atlas V rocket on the NROL-36 mission in September 2012. Little information has been disclosed about these projects, but it is widely publicized that the Colony I Bus was a success [69].

The Colony I Bus was developed by Pumpkin Inc. [69], which is a major CubeSat supplier. The Colony I Bus was the first all-in-one 3U CubeSat system that incorporated a reaction wheel

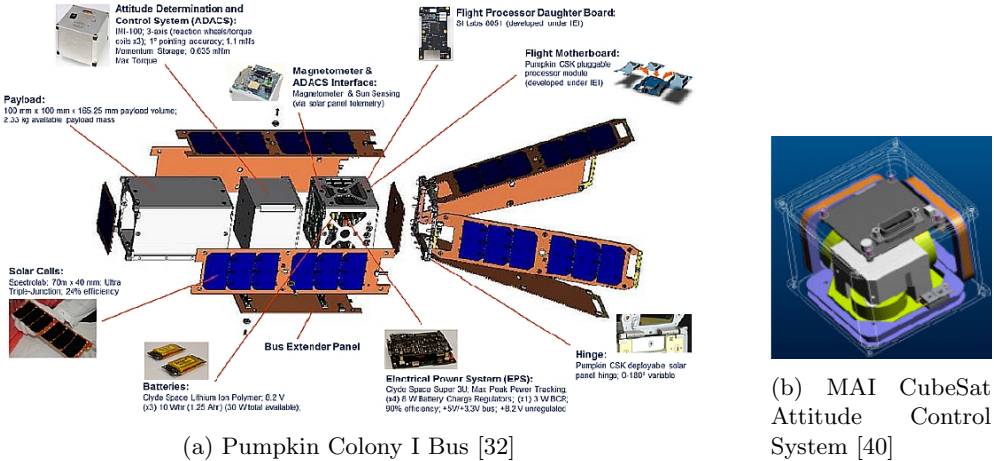


Figure 4: CAD models of the Colony I Bus and Attitude Controller.

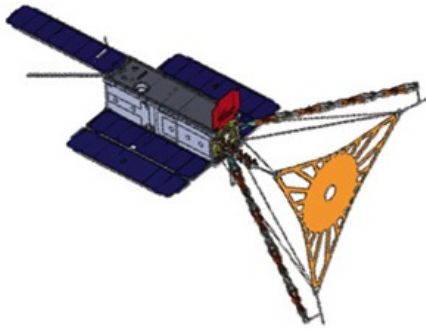


Figure 5: CAD model of FalconSat-7 using the Boeing Colony II Bus [35].

based attitude control system and central processor. Fig. 4a depicts the Colony I Bus, which can be broken down into three main parts: the payload, the attitude control system, and the flight electronics, all of which were placed within a 3U form factor. All of the flight electronics were standard off-the shelf Pumpkin products; however, the real innovation of this project was the attitude control system, which was developed by Maryland AeroSpace Inc. [40].

The Maryland AeroSpace MAI-201 is a full attitude control system with built in reaction wheels and magnetic torquers all in a small 1U design. A CAD model of the MAI-201 attitude control system can be seen in Fig. 4b. It communicates via RS-232 and is a complete plug and play solution. It is able to operate off a minimal 200mA and a single +12volt rail. The MAI-201 is capable of producing 5mNm of torque.

The successor to the Pumpkin Colony I Bus was the Boeing Colony II Bus, shown in Fig. 5. Unfortunately, very few specs for the Colony II Bus are available, but the federal government has the vision of launching twelve Colony I Buses and anywhere between twenty and fifty Colony II Buses [51]. Both buses are estimated at around \$250,000 per bus according to an NRO presentation in 2011 [51]. The Colony II Bus is rumored to have four reaction wheels and three magnetic torquers built into it occupying up to 1.5U of a 3U CubeSat, leaving 1.5U for the payload.

Last, but not least, is NASA AMES' phoneSat was launched in mid August 2013. The phoneSat is a 1U CubeSat that is controlled via an Android Nexus S phone. The developer believed that smartphones have all the processing power necessary to control a CubeSat. Smartphones are capable of packaging vast amounts of electrical hardware into a very small platform

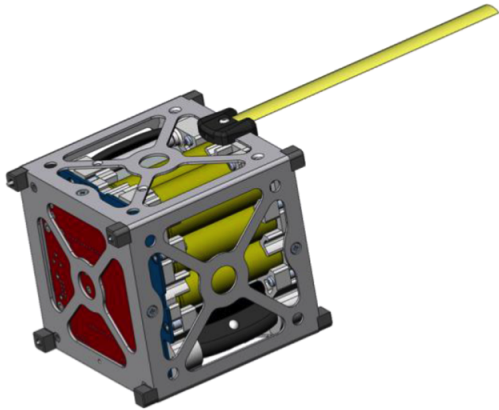


Figure 6: CAD model of NASA’s phoneSat 2.0, which operates using an Android phone [46].

and many have everything required to control a CubeSat. The sensors on a phone and the camera are all the sensors required for attitude control on a CubeSat. It is the idea of the developers of phoneSat to write an Android application to control phoneSat [46]. The phoneSat project best demonstrates the concept of CubeSats, to create a cheap off-the-shelf satellite.

In terms of attitude control, the phoneSat also has reaction wheels and magnetic torquers. Another point of interest is that phoneSat does not utilize inertia wheels on its reaction wheels. Instead, the motors are free spinning, which limits the satellite’s slew rate. The three projects mentioned are not the only attitude control systems being developed, but at this time these seem to have the most potential.

1.4 Evaluation and Prototyping

To assess and evaluate the performance of the attitude control system some simple analysis will be done. These tests will be used to evaluate the yaw component of the attitude controller. It is assumed that if yaw control and regulation can be demonstrated, the same method can be employed on the roll and pitch axes. Demonstration of yaw control will be done using the apparatus in Fig. 7, which allows free movement in the yaw plane, but restricts movement in the roll and pitch planes. Restriction movement to the yaw plane will be implemented with a ball bearing to reduce friction.

The testbed will be used to verify if the control hardware can precisely control and regulate the system actuators. Successful demonstration of the control hardware should show that the flight control hardware and the attitude estimator are working in sync. As previously

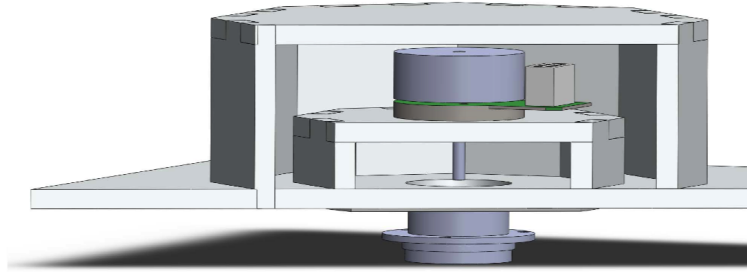


Figure 7: Cross-sectional view of the control hardware testbed used to demonstrate attitude control about the yaw axis.

mentioned, the control hardware being proposed is only a system prototype and not a completed space system; it lacks both roll and pitch control and the proper reference sensors. However, demonstration of the testbed will establish the foundation for a functional satellite attitude control system.

1.5 Thesis Structure

This thesis intends to lay the ground work for a reaction wheel-based CubeSat attitude control system by exploring the available satellite actuation systems (Section 2) to justify the use of reaction wheels. The CubeSat attitude actuators are then used to develop the required attitude control hardware and software, Sections 3 and 4, respectively. The attitude control software section (Section 4) characterizes the Direction Cosine Matrix attitude estimator for terrestrial prototyping and system testing. The attitude control hardware covers the mechanical and electrical designs for the attitude control system and explores the limitations placed on the system by the size constraints. Further hardware development can be located in Section 5, which details the actuator control hardware, the major design criteria, and the associated actuator control software (which describes the algorithms employed to control the on-board motors). The different aspects of the attitude control hardware and software are then consolidated in Section 6, where the attitude estimation software is used in conjunction with the actuator electronics used to control the orientation of the testing platform. Some conclusion and suggestion for future work are discussed in Section 7.

2 Background

Almost all existing satellites require attitude estimation and control. A wide variety of actuators exist to manipulate the attitude of the spacecraft. Of the available actuators, a few examples are: permanent magnets, magnetic torquers, reaction wheels, and Control Moment Gyroscopes (CMG). These actuators have all been implemented previously in CubeSat projects, but permanent magnets and magnetic torquers remain the most popular due to their small form factor, cost, and ease of operation. Each of the four actuators listed will be explored in more detail and evaluated for use on the Attitude Estimation and Control System (AECS). Evaluation of the actuators performance will be assessed on deployed CubeSats.

2.1 Magnetic Field Actuators

The Earth's magnetic field is quite complicated due to shifting of the Earth's molten iron core [37]. For this reason, a model is generated (the International Geomagnetic Reference Field (IGRF) model), which is updated every five years. The IGRF accumulates inclination, declination, vertical and horizontal magnetic field strengths. The IGRF models from 2010 are published on the National Oceanic and Atmospheric Administration (NOAA) webpage. A graphical model of the magnetic declination and the magnetic field intensity for 2010 is shown in Fig. 8 and 9, respectively.

The IGRF defines five parameters (inclination, declination, vertical and horizontal magnetic field strengths, and total field intensity) of the magnetic field. These parameters are used

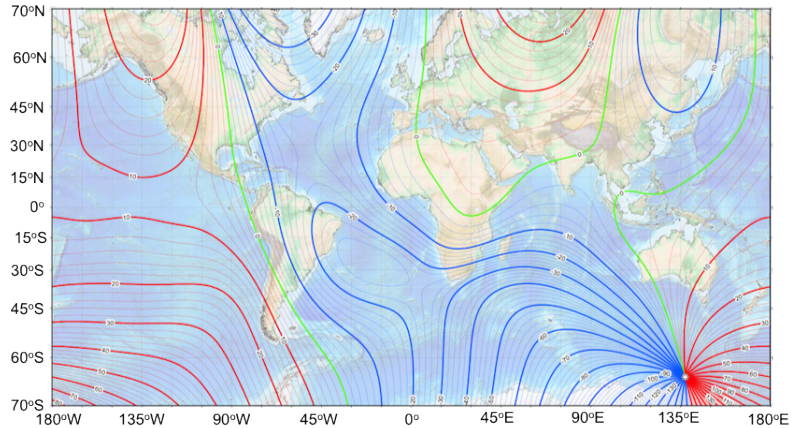


Figure 8: The Earth's Magnetic Field Declination lines [10].

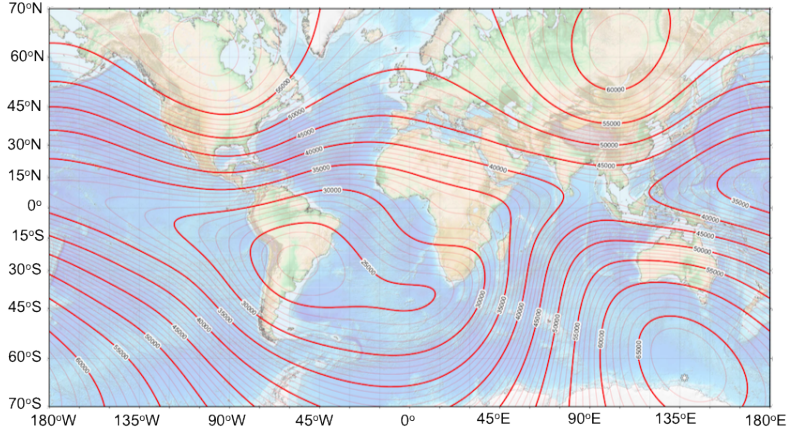


Figure 9: The Earth’s Magnetic Field intensity [10].

to describe the intensity and the direction of the magnetic field at any point on or near Earth, however only three independent parameters exist. The Declination is the difference in the angle between geographical north and magnetic north. The Inclination angle represents the angle created by the vertical component of the magnetic field. The horizontal and vertical intensity represents the magnitude of the magnetic field in the horizontal and vertical planes, respectively. The total intensity measures the total magnetic field in the horizontal and vertical planes. The total magnetic field intensity is not uniform as seen in Fig. 9. Using three of the independent parameters, a magnetic field vector can be created to describe any location on or above Earth. For instance the inclination, declination, total field intensity can be used to describe the magnetic field in the spherical coordinates.

Permanent magnet attitude stabilization utilizes Earth’s magnetic field and onboard magnets to orient the satellite. The permanent magnets are usually placed on two planes of the CubeSat to interact with the Earth’s magnetic field. During deployment of the CubeSat, the orientation and rotation of the CubeSat are unknown. This is due to the fact that CubeSats are usually the secondary or tertiary payload, meaning less importance is given to their orientation upon launch. Permanent magnets are useful because they permit the CubeSat to orient itself with the Earth’s magnetic field regardless of its initial orientation or rotation. Over time the CubeSat will completely orient itself with the Earth’s magnetic field. However, because the Earth’s magnetic field is non-uniform, the permanent magnets will create deviations in the CubeSat’s nominal orientation. Moreover, permanent magnets do not allow the CubeSat to

alter its orientation with respect to the Earth (only a single fixed orientation is possible) making permanent magnets less than ideal for applications where accurate motor control or pointing is necessary.

A magnetic torquer rod is another device that can interact with the Earth's magnetic field to orient a satellite. In contrast to a permeant magnet the magnetic torque rod or "torquer" is a coil of wire wrapped around either a metal or air core (see Fig. 10). The magnetic torquer works by supplying current to the coil, which generates a magnetic field. The direction of the magnetic field can be found by application of the right hand rule [65]. When power is applied to the torquer, it acts like a bar magnet, except that the magnetic moment generated by the torquer can be manipulated by altering the flow of current in either strength or polarity. This allows for active control of the spacecraft's orientation when a torquer on each of the spacecraft axes.

The interaction between the magnetic moment generated by the permanent magnet and the Earth's magnetic field is the same as the interaction between the torquer and the Earth's magnetic field. Both interactions are described using Eq. 1, where the torquer or permanent magnet's magnetic moment is represented by M and the Earth's magnetic field is represented by B . Eq. 1 states that the cross product of the magnetic moment and magnetic field is equal to the generated magnetic torque [47].

$$T_{mag} = m \times B \quad (1)$$

Eq. 1 shows that the Earth's magnetic field plays a significant role in the magnitude of the torque generated by the permanent magnet or torquer. For this reason, use of magnetic

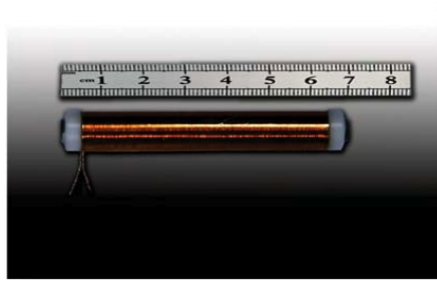


Figure 10: Image of a CubeSat Magnetic Torque Rod [7].

actuation is limited Low Earth Orbit (LEO). Eq. 2 begins by defining the Earth's magnetic potential (V), represented in spherical coordinates, with respect to the distance from the center of the Earth (r) and the Earth's dipole moment, $m = 7.94 \times 10^{22} Am^2$ [47]. The magnetic potential is then used in Eq. 3 to define the Earth's magnetic field, where the gradient is taken of the magnetic potential (Eq. 3 is a simplified model of the Earth's magnetic field). The gradient is taken with respect to the distance from the center of the Earth (r), the inclination angle (ϕ), and the rotation angle (θ).

$$V = \frac{\vec{m}\vec{r}}{4\pi r^3} \quad (2)$$

$$\begin{aligned} B &= -\mu \nabla V = -\mu_0 \left[\frac{\delta V}{\delta r} + \frac{\delta V}{\delta \phi} + \frac{\delta V}{\delta \theta} \right] \\ B_r &= -\frac{\mu_0 m}{2\pi r^3} \cos\theta \\ B_\phi &= -\frac{\mu_0 m}{4\pi r^3} \sin\theta \\ B_\theta &= 0 \end{aligned} \quad (3)$$

$$\begin{aligned} |B| &= (B_r^2 + B_\phi^2 + B_\theta^2)^{\frac{1}{2}} \\ &= \frac{\mu_0 m}{4\pi r^3} (4\cos^2\theta + (1 - \cos^2\theta))^{\frac{1}{2}} \\ &= \frac{\mu_0 m}{4\pi r^3} (1 + 3\cos^2\theta)^{\frac{1}{2}} \end{aligned} \quad (4)$$

The resulting magnetic fields are composed of a radial component (B_r) and an inclination component, (B_ϕ). No rotation component exists because the magnetic field potential is ideally uniform along constant latitude lines. As seen from the magnetic field Eq. 4, the magnitude of the magnetic field has a $\frac{1}{r^3}$ relationship, which measures that the magnitude of the magnetic field decreases rapidly as the distance from the center of the Earth increases. This is why magnetic attitude control is only effective for satellites operating in LEO (160km - 2000km) [20].

2.1.1 Permanent Magnets Applications

GeneSat-1 was a 3U CubeSat project whose mission was testing the effects of microgravity and space radiation on biological cultures [73][88]. The project was launched in December 2006 at an orbit of 460km and remained in orbit until August 2010. The primary attitude control system relied on permanent magnets to orient the spacecraft with the Earth's magnetic field. The satellite orbit and trajectory was simulated using orbital determination and magnetic field models [73]. Orbital determination is a way of predicting a satellite's orbit using force, environment, and other models predicting the satellite's interactions while in space [59][12].

Another application of permanent magnet attitude control is the CSSWE (Colorado Student Space Weather Experiment), which has been operational since September 2012 [88][63]. The spacecraft was placed in an elliptical orbit of 790km x 490km with a mission to study the Van Allen Radiation Belt [88]. Attitude stabilization was accomplished using permanent magnets to align the spacecraft with the Earth's magnetic field and hysteresis rods to dampen the oscillatory effect of the fluctuations in the Earth's magnetic field. A bar magnet with a magnetic moment of $m = 0.3\text{Am}^2$ and two hysteresis rods was able to stabilize the system with a settling time of less than seven days and an accuracy of $\pm 15^\circ$ [64].

2.1.2 Torquer Applications

Two projects that utilized magnetic torquers primary for attitude control are the Boeing CubeSat TestBed-1 (CSTB-1) and Tokyo Institute of Technology's CUTE-1.7+APD. The CSTB-1 uses four sun sensors and five 2-axis magnetometers to orient the 1U CubeSat at an altitude of 745km [88]. The CUTE CubeSat uses three magnetic torquer rods oriented in three orthogonal planes for attitude control [88]. The CUTE project uses a Personal Data Assistant (PDA) as the main operating module and the torquers for attitude control [88]. A coreless torquer coil was developed with a maximum magnetic dipole moment of $m = 0.037\text{Am}^2$ which is able to produce $1.1\mu\text{Nm}$ of torque with a drive current of 10mA [88].

2.2 Reaction Wheels

The reaction wheel functions by utilizing the principle of the Conservation of Angular Momentum, which states that the net angular momentum of a rotating body must stay constant if no external torque is applied [65] [45]. The reaction wheel spins a large mass, the flywheel, at a very high angular velocity. Torque is generated by the reaction wheel due to the moment of inertia of the flywheel and its acceleration, as expressed in Eq. 5.

$$\tau_{motor} = \alpha_{wheel} \cdot I_{wheel} \quad (5)$$

When torque is generated by the reaction wheel an equal and opposite torque is produced on the spacecraft causing rotation of the CubeSat. Fig. 11, depicts the rotation of the reaction wheel in the clockwise direction (blue) and the CubeSat's rotation in the counter-clockwise direction (black), where the red arrow denotes the axis of rotation. The rotation of the CubeSat is constrained by the conservation of angular momentum as expressed in Eq. 6.

$$\begin{aligned} I_{sat}\vec{\omega}_{sat} + \vec{h} &= 0 \\ I_{sat}\vec{\omega}_{sat} &= -\vec{h} \\ I_{sat}\vec{\omega}_{sat} &= -\sum_{i=1}^N \vec{a}_i I_{wheel} \omega_{wheel} \end{aligned} \quad (6)$$

Eq. 6 shows that the relationship between the angular velocity of the CubeSat and flywheel. This shows that the maximum speed of the CubeSat is proportional to the moment of inertia of the flywheel and the satellite body. Therefore, it is necessary to increase the flywheel moment of inertia to increase the CubeSat's maximum angular velocity.

Evaluation of the CubeSat's dynamics is achieved by taking the derivative of both sides of Eq. 6 with respect to time. In the case of the reaction wheel the torque is dictated by the maximum torque generated by the motor. Manipulation of the flywheel moment of inertia affects the angular acceleration, since the maximum torque remains constant. Increasing the moment of inertia decreases the effective acceleration of the reaction wheel. Consequently, the time required for the reaction wheel to reach full speed is increased for a given amount of torque demanded. This is a positive effect for reaction wheel systems as it decreases the frequency at

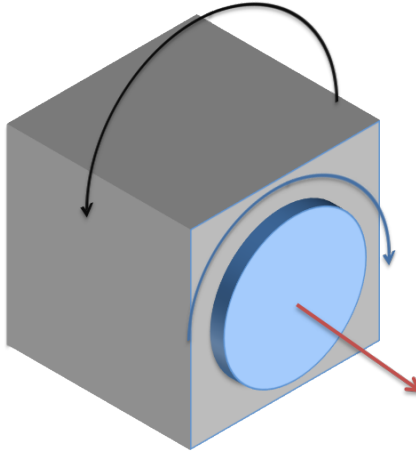


Figure 11: Application of the Conservation of Momentum is used to rotate the CubeSat (gray box) via control of the reaction wheel in blue.

which momentum dumping is required.

Momentum dumping is a method used to spin down the reaction wheels using external control torques [70]. A reaction wheel uses a change in its angular velocity to apply torque to the spacecraft. However, once the maximum angular velocity of the reaction wheel is reached the spacecraft is not able to apply additional torque in that direction. This can be expressed with the conservation of angular momentum seen in Eq. 6. Eq. 6 shows the relationship between the angular momentum of the satellite and momentum wheel. As the angular velocity of the momentum wheels changes, the angular velocity of the satellite will change proportionally. However, when the maximum angular velocity of the momentum wheel is reached, it is not possible to increase the angular velocity of the satellite. To apply more torque, the angular velocity of the reaction wheel must be reduced. However, reducing the angular velocity generates an angular acceleration and unwanted torque applied to the spacecraft. To counteract this unwanted torque, another opposing torque must be applied to the system by an external actuator. This can be done by using the torque generated by the torquers and the Earth's magnetic field to hold the orientation of the spacecraft constant while the reaction wheels are being spun down.

2.2.1 Reaction Wheel Applications

Use of reaction wheels as the primary Attitude Control System (ACS) is best exemplified by the Colony-I Bus project, specifically the QbX-1 and QbX-2 projects which were launched

in December of 2010. Both spacecraft were deployed in LEO at an altitude of 300km, giving them short operational lives averaging thirty-four days [88]. Attitude control was demonstrated using the Maryland Aerospace Inc. MAI-201 which incorporates reaction wheels and torquers for attitude control. The MAI-201 is capable of producing 0.635mNm of torque and operates using 2.4W on average [40]. Using the MAI ACS and “space dart” mode, attitude control was maintained with an accuracy within 5° [88]. Space Dart mode is a mechanical configuration of the spacecraft which uses the aerodynamic shape of the satellite and atmospheric drag at 300km to help orient itself passively. Using the space dart mode in conjunction with active reaction wheel control, allows the satellite to fine tune its orientation in LEO.

2.3 Control Moment Gyroscopes

The Control Moment Gyro or CMG employs a gimbaled angular momentum vector to manipulate the satellite’s orientation. The CMG consists of a large circular flywheel, which rotates at a constant speed. The CMG differs from the reaction wheel, which uses a change in speed of the flywheel to generate torque. However, CMG torque is generated by gimballing the flywheel in a direction perpendicular to the axis of rotation.

Fig. 12a, depicts a flywheel rotating about the angular momentum vector in the counter clockwise direction, this is essential to the gyroscopic effect. Application of Newton’s Second Law for Rotation states that the sum of the torques applied to the system are equivalent to the change in angular momentum ($\frac{dL}{dt}$) as expressed in Eq. 7 [65]. If no torque is applied to the system the angular momentum will remain constant. As expected, the flywheel will continue rotating in the same direction and no Torque Vector will be generated as depicted in Fig. 12a.

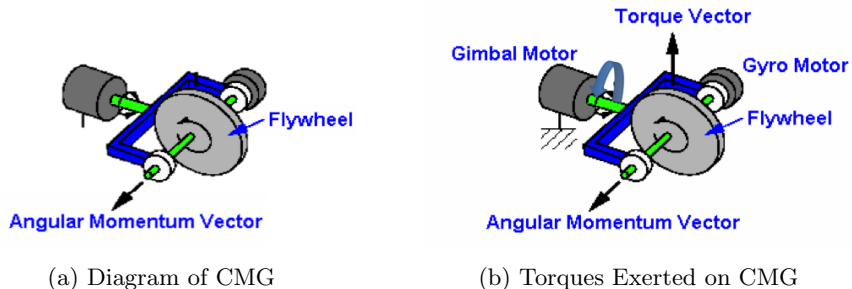


Figure 12: CMG concept of operation: (a) direction of momentum vector L before gimballing; (b) torque output due to gimbol motion [62]

$$\Sigma\tau = I\alpha = \frac{d\mathbf{L}}{dt} \quad (7)$$

However, if the CMG is rotated in the counter clockwise direction as depicted by the blue arrow in Fig. 13, then an associated torque vector is generated perpendicular to the axes of rotation. Application of the torque means that the angular momentum of the flywheel is no longer constant and the Angular Momentum Vector will begin to move in the direction of the torque vector [76]. In Fig. 13, this is depicted as a clockwise rotation about the gimbal axis. Once the GMC stops gimbaling, torque is no longer applied to the system and in accordance with Newton's seconds law of rotation, the angular momentum is no longer changing. This is observed as a stop in the rotation of the CMG about the gimbal axis.

Control Moment Gyro require a more complex mechanical architecture and often a larger form factor which has made them unpopular for CubeSats. In general, the high cost, large volume, and increased complexity make it difficult to implement CMGs in CubeSat projects.

2.3.1 Control Moment Gyroscope Applications

Despite the challenges listed above, small satellite Control Moment Gyros have been developed by Honeybee Robotics and can be seen in Fig. 13b. The CMG is capable of accelerating “a 24-kg satellite at 3deg/s²” and occupies a volume of 125cm³ [18]. This device might be too large for most CubeSat projects, but demonstrates the possibility of a CubeSat CMG system. The SwampSat project is a 1U CubeSat developed by the University of Florida with the mission of developing a CubeSat CMG system [48]. The University of Florida have developed a single



(a) SwampSat CMG [88]



(b) Honeybee Robotics [18]

Figure 13: Images of Small Satellites CMGs

gimbaled CMG which is configured in SwampSat as a pyramid of four CMGs. These CMGs are capable of producing 0.8mNm of torque and require 3W (peak power), see Fig. 13a [48]. The SwampSat has not yet been launched.

2.4 Actuation Summary

Of the four actuation methods, described in this chapter, the reaction wheel system was chosen for the prototype hardware due to higher accuracy and lower power consumption as compared to the CMGs. Reaction wheel projects like the Colony I Bus have shown the functionality of CubeSat reaction wheel systems, demonstrating a control torque of 0.635mNm while consuming 2.4W [40]. Given the tradeoff between the CMG and reaction wheels systems, the reaction wheels seem to be superior due to the reduced mechanical complexity of the system. In comparison with the permanent magnetic and magnetic torquer systems, reaction wheel systems are able to produce significantly greater amounts of torque. This is due to the weak interaction between the Earth's magnetic field and the magnetic dipole moment generated by the permanent magnet or magnetic torquer. The Earth's magnetic field decrease as the satellite travels higher in altitude.

3 Hardware - Design Objectives

The AECS hardware need to be evaluated to determine the amount of space available to the control electronics. The control electronics also need to be selected such that they are able to measure the attitude and control the actuators. The system controller is designed to be a general purpose Attitude Estimation and Control System (AECS) with CubeSat based design criteria. The attitude control electronics can best be described as a hardware configurable development board. The hardware is designed with versatility in mind, making it possible to use this AECS on a large range of platforms. This is its major advantage compared to the other AECS that will be discussed later. This is accomplished by employing a shield concept similar to that commonly found in the Arduino architecture [4].

The design process has three major goals: size, power vs. performance, and versatility. These three factors played a large role in the design of the attitude control electronics and in the evaluation of existing FSC. As mentioned in the Introduction, the size of the control hardware is limited by the size of the CubeSat, while power and performance are limited by the intake of power from the solar panels.

3.1 Size Constraints

The size of the attitude control electronics are constrained by the size and configuration of the components and actuators implemented by the attitude control system. The attitude control system requires hardware components including reaction wheels and torque rods, which occupy a significant amount of the available space. During the prototyping phase, some hardware configurations were investigated to estimate the available space for the flight control hardware. Configurations with three and four reaction wheels will be modeled for completeness.

3.1.1 Reaction Wheel Array Constraints

The design and size limitations placed on the attitude control hardware are dictated by the limitations of a 1U CubeSat. CubeSat design specifications were originally proposed by Stanford and Cal Poly San Luis Obispo in 2002 [68]. Fig. 14a, is a commercial product following the CubeSat standards, created by Pumpkin Inc [2]. The goal of the attitude control system is to fit within the space provided by the Pumpkin CubeSat shell. Modeling of potential component

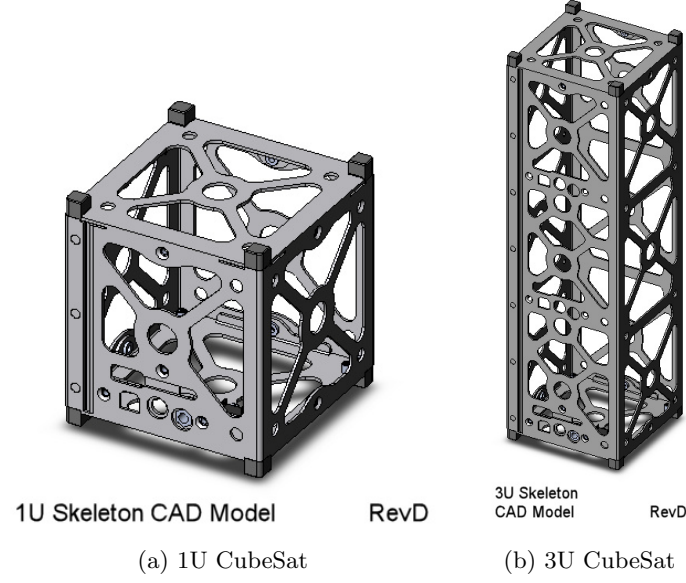


Figure 14: The control hardware was designed to fit within the Pumpkin CubeSat Skeletons [2].

layouts was preformed to evaluate the size constraints.

3.1.2 Motor Geometry

When evaluating the Reaction Wheel Array (RWA) geometries, several parameters were taken into consideration. First, actuation must be performed on all three axes. Without three dimensions of actuation, controlling orientation in all three axes is impossible. Another consideration is the idea of redundancy, if one of the motors fails, will the CubeSat be stranded or will it be able to continue operating? To better evaluate the need for a redundant system it is important to account for the lifespan of the CubeSat. If the CubeSat only needs to operate for a short period of time, a redundant system might not be necessary. The final parameter employed to evaluate the mechanical layout is the space remaining for the electronics, power supply, sensors, and any other CubeSat peripherals. These parameters are implemented to evaluate the proposed designs.

3.1.3 Orthogonal Reaction Wheel Configurations

Among the surveyed CubeSat RWA geometries, the standard three wheel orthogonal motor configuration seems to be the most common. An example of this configuration can be found in Fig. 15. This diagram is based on the CAD model of the MAI-201 attitude control

system created by Maryland Aerospace Inc. (MAI) [40]. This system has three reaction wheels oriented in three different axes (x, y, and z). For reference, this design will be designated as the Small Wheel (SW) Configuration.

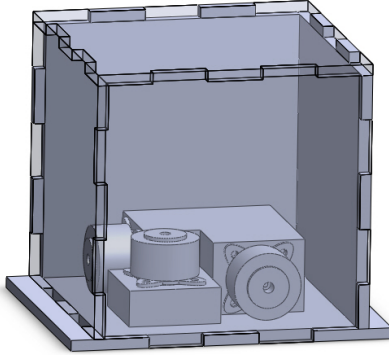


Figure 15: Reaction Wheel Layout similar to that of MAI-101 used on the Colony I Bus [40].

The SW configuration is able to control all three the orientation axes due to the perpendicular orientation of the reaction wheels. Perpendicular reaction wheels provide for a simple control algorithm. For example maneuvering about the x-axis only requires the use of the x-axis actuator. This design layout lacks redundancy because the system is not able to recover if one of the motors is damaged or fails. For example, if the x-axis motor fails the satellite will no longer be able to actuate about the x-axis.

The SW configuration trades off redundancy and momentum storage in order to provide more space for the flight electronics. This configuration provides the greatest volume for the flight electronics (250cm^3). But, has the smallest flywheels moment of inertia ($I = 8.96 \times 10^{-7}\text{kgm}^2$) as compared to other configurations. The moment of inertia for this configuration is calculated assuming the flywheel of a 18.5mm diameter constructed using 304 stainless steel with a density, $\rho = 8000 \text{ kg/m}^3$ [1].

A similar design configuration is based on the SwissCube reaction wheel architecture [49], which utilizes a much larger flywheel, designated as Big Wheel (BW). The BW configuration utilizes three orthogonal reaction wheels that are much larger than that of the previous SW design. The reaction wheels have been placed on three orthogonal planes of the housing unit as

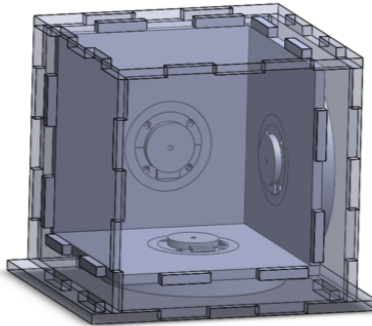


Figure 16: Motor layout similar to that of SwissCube which allows the moment of inertia of the flywheel to be maximized [49].

depicted in Fig. 16. The three flywheels are placed on the outer walls to increase the flywheel radius and volume for the flight electronics (6cm x 6cm x 6cm). The larger flywheel design also generates a much greater moment of inertia of $I = 6.53 \times 10^{-5} \text{ kgm}^2$. Recall that increasing the moment of inertia of the flywheel increases the amount of momentum stored within the reaction wheel system. This increases the angular velocity of the satellite and decreases the frequency of momentum dumping as described in the Section 2.2: Reaction Wheels.

3.1.4 Square Pyramid

The Square Pyramid geometric scheme is a more versatile design that provides a component of redundancy. In this particular design, the actuators are all on the bottom of the CubeSat (see Fig. 17). This was done to create the most space for the electronics. As depicted in the Fig. 17, four actuators are placed in the four corners of the CubeSat. As mentioned earlier, the orientation of the motors is redundant; if a single motor becomes inoperable the others can compensate. This will reduce the performance, but the mission can still be accomplished. This geometric configuration provides about 200cm^3 of space allocated for the flight electronics. However, due to the addition of an extra reaction wheel, the dimensions of the flywheel and subsequently, the moments of inertia are smaller; $I = 3.57 \times 10^{-6}\text{kgm}^2$ per wheel.

3.1.5 Geometry Analysis

Table 3 provides an overview of the different motor orientations or geometries mentioned earlier in this Section. From the earlier discussion, only the Pyramid design allows for reaction

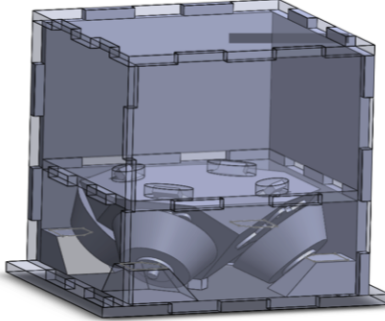


Figure 17: Pyramid design with 4 reaction wheels all 45° off vertical allowing for a redundant actuator configuration.

wheel redundancy. However, the operational lifetime and cost should be taken into account. For the evaluation of the prototype, the operational lifetime is assumed to be six months. Justification for the operational lifetime can be found in Section 3.2: Flight Controllers. Assuming a six month operational lifetime, the importance of a redundant system is reduced. A shorter operational lifetime gives less time for the system to fail. Since deployment of CubeSats are relatively cheap (\$50k), it could be more cost effective to deploy a second CubeSat, than develop a hardened satellite. The deemphasis of the reaction wheel redundancy places a larger emphasis on the available space for the flight electronics. The SW design provides the most space, but the BW design was chosen due to its larger momentum storage capabilities.

For comparison the BW design is compared with two other reaction wheel systems. A wheel created at Saint Louis University by Sanjay Jayaram [61] and a reaction wheel created by Espen Oland from Narvik University College [83]. The reaction wheels created by Sanjay Jayaram and Espen Oland were chosen because of their similar design constraints.

It should be noted that certain assumptions were made about the motor used by Oland. It was assumed that he employed the same motor as did Jayaram. Some of the dimensions published by Mr. Jayaram were inconsistent, and these assumptions simplify the analysis.

Table 3: Motor Geometry Summary

Geometry	volume (cm^3)	Wheel Moment of Inertia (kgm^2)	Redundancy
Small Wheel	247.39	8.96×10^{-7}	no
Big Wheel	210.65	653×10^{-7}	no
Square Pyramid	197.61	35.7×10^{-7}	yes

Table 4: Reaction Wheel Summary

Parameter	AECS	Nano Wheel	Oland
Motor Torque (mNm)	0.51	0.8	0.8
Moment of Inertia (kgm^2)	6.7788×10^{-5}	2.7288×10^{-5}	1.4786×10^{-5}
Motor Max Speed ($\frac{rad}{s}$)	1539	1696	1696
Max Momentum (Nms)	0.104	0.046	0.025

The St. Louis University design, which will be designated to as the Nano Wheel, uses a Faulhaber 1516 Brushless DC motor. This is very similar to the motor used by AECS, which uses the Faulhaber 1509. The 1516 is a little larger and has a little more torque. These assumptions are based on some figures presented within the papers [61] [83]. A summary of the results can be found in Table 4. Based on the parameters in Table 4 it can be seen that the parameters for the Big Wheel and Nano Wheel are comparable.

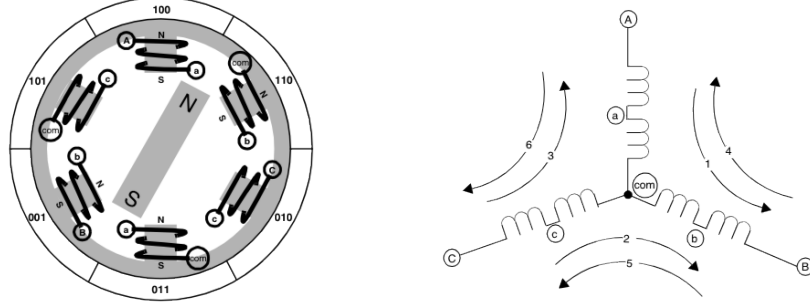
3.1.6 Brushless DC Motors

To evaluate the torque generated by the three reaction wheel configurations, the specifics of the motors must be discussed. The reaction wheel geometries were evaluated using the Faulhaber 1509 Brushless DC motor. A Brushless DC (BLDC) motor was chosen primarily due to its high efficiency, reduced power consumption, and higher speed range (giving a larger speed range for the reaction wheel) [96].

Using a BLDC motor has its advantages. Due to the fact brushes are not used, less maintenance is required. BLDC motors are also better at accelerating and decelerating compared to brushed motors because of lower rotor inertia. In addition, they have a linear speed/torque curve similar to a brushed motor. On the down side, BLDC motors are more complicated to use due to the required electrical commutation.

In order to move the BLDC motor, special commutation needs to be performed in order to energize the coils within the motor. Fig. 18 depicts a simplified version of the BLDC motor and the internal coils. The image on the right of Fig. 18 is a simplified version of the internal magnets and coils. Notice the image has six coils each labeled with a binary code. The binary code represents the Hall Effect Sensor state. Commutation is accomplished by switching current through the appropriate coil.

Commutation is accomplished by sequentially changing the flow of current in each of the



(a) Diagram of the rotor magnet and motor coils.

(b) Diagram of the Y configuration of the motor coils.

Figure 18: Simplified diagram of a single pole BLDC motor showing how the coils interact with the rotor magnet (on the left). On the right, the flow of current is shown for each of the coils [50].

coils. In this example, if counter-clockwise rotation is desired, then the next south polarity coil will be “101” followed by “001” and so on.

The diagram in Fig. 18b depicts the coils within the motor. The coils are configured in a Y configuration, with three legs: A, B, and C. If the Hall Effect sensors read state “100”, terminal A must be connected to ground and terminal B connected to V_{cc} . This leaves terminal C disconnected in a high impedance state. This allows current to flow in the correct direction and generates the correct magnetic field. In this case, current will flow from terminal B to terminal A as shown in Fig. 18b, depicted by arrow 4. Specifics about the BLDC control hardware can be found in Section 5: Control Shield.

The Faulhaber 1509 BLDC motor was chosen for the AECS platform because of its small form factor and high efficiency. However, this comes at a cost, limited motor torque ($\tau = 0.92\text{mNm}$) [60]. As previously mentioned, as the moment of inertia of the flywheel is increased, the angular acceleration generated by the motor is decreased (keeping the maximum torque constant). References to the moments of inertia of the three potential reaction wheel designs can be found in Table 3. This comparison shows that the moment of inertia is greatest in the BW configuration and is smallest in the SW configuration. This means that momentum dumping will be required less frequently for the BW configuration and most frequently for the SW configuration. Momentum dumping is required for reaction wheel system, but the process hinders the actuation of the satellite while the reaction wheel’s momentum is being dumped: it

is best to limit the momentum dumping process as much as possible.

Due to the limited amount of momentum storage generated by the Pyramid and SW designs and the minimal difference in space for the flight electronics, the BW design was chosen for further development. This means that all size constraints will be referenced to this design. Therefore, the flight electronics are limited to a 6 x 6 x 6 cm volume. The hardware limited to this space includes: three BLDC motor drivers, an attitude estimator, and three magnetic torquers and their control electronics. The three motor drivers are necessary for control of the three reaction wheel motors and the attitude estimator is necessary to calculate the platform's orientation. The magnetic torquers are necessary for momentum dumping.

3.2 Candidate Flight Controllers

Evaluation of the flight control processor covers both space rated and terrestrial microcontrollers. Space rated systems offer application specific advantages, such as radiation protection. On the other hand, terrestrial microcontrollers provide a readily available development system at reduced cost. To evaluate all of the various options, environmental and mission considerations must be explored.

Another altitude related obstacle is the International Space Station (ISS) which maintains an altitude of roughly 335km - 400km [87]. Taking these factors into account, the assumed deployment altitude will be 350km, which gives an operational lifetime of about six months [87]. This altitude was chosen to avoid the main body of the ISS and conform to the space debris policy while maximizing the operational lifetime of the CubeSat. As the secondary or tertiary payload CubeSats are placed in an orbit where they will not affect the primary payload, usually at an altitude lower than the primarily payload.

The operational experimentation time of four projects will be evaluated: GeneSat-1, CSTB-1, QbX1, and QbX2. GeneSat-1 studied the effects of radiation and microgravity on bacteria, taking one hundred experimental hours to complete [88]. Data collection and transfer to the ground station extended the mission to twenty-one days. CSTB-1 took four months to complete its operational goals and QbX1 and QbX2 were only operational for about a month due to their low altitude. This demonstrates that a six month operational lifetime should be sufficient for most CubeSat projects.

Another important consideration is exposure to space radiation; it is believed that radi-

ation was the cause of failure in the CUTE-1.7+APD project [88]. Space radiation near Earth is concentrated in the Van Allen Belt which is located between 1,000km - 60,000km. Radiation is trapped in this region due to the Earth's magnetic field [19]. Due to the short operational lifetime of the project and deployment below the Van Allen Radiation Belt, less emphasis needs to be placed on the use of radiation-hardened electronics. Due to the cost it was decided radiation hardened electronics will not be used. Instead the electronics will be embedded behind the actuators and batteries. It was decided that if a failure occurs it would be more cost effective to launch a new CubeSat.

Evaluation of space flight control systems will cover examples of implemented CubeSat microcontrollers which are commercially available solutions. Some commercially available solutions include: NanoMind A712D, Q6, and Pumpkin Pluggable Processor Modules. The NanoMind controller occupies a 96 x 96mm surface area [7] which is too large for the Big Wheel design. In fact, all three commercial products are too large to fit within the available space defined by the Reaction Wheel Array. The NanoMind controller also requires a six to ten week lead time before it can be received from the manufacturer. In addition to the several months lead time, each system costs about \$6000 while some terrestrial autopilots cost much much less [2] [7] [17]. The NanoMind controller uses an ARM7 processor which allows for Pulse Width Modulated (PWM) signals needed to control the BLDC motors. The Q6 controller utilizes a Xilinx FPGA, which requires a substantial amount of power, about 1W [7]. Finally, the Pumpkin Pluggable Processor Module comes in three choices of processors (PIC, MSP430, C8051), all of which are commonly found in terrestrial autopilots.

The CUTE-1.7+APD used consumer electronics, namely, a Hitachi Personal Data Assistant (PDA) for system control [88]. The PDA is able to package several electronics into small form factors, but does not produce the appropriate PWM signals to control the BLDC motors (more specifics of BLDC motor control are described in the Section 5: Control Shield). Other projects used readily available microprocessors, such as the PIC18 on the GeneSat project [73]. Terrestrial autopilots use similar microprocessors but are also additionally outfitted with inertial sensors and necessary control hardware to operate electric motors.

The three major terrestrial autopilots being compared include: the SLUGS [77] [78] [79], the ArduPilot [42], and MatrixPilot [36] [43]. These three autopilots were all very influential in the design of the attitude control hardware developed in this thesis.

3.2.1 SLUGS

The Santa Cruz Low-cost UAV GNC System (SLUGS) autopilot was designed by Mariano Lizarraga [79] and the UCSC Autonomous System Laboratory as a fixed winged UAV autopilot. The SLUGS autopilot was designed as an easy to use research platform capable of rapid control algorithm prototyping. The SLUGS system employs a Matlab based embedded coding environment created by Lubin Kerhuel [72], which utilizes Matlab's Simulink blockset to create a visualized program environment. This visual programming method allows for a more structured and easier to follow programming method.

Due to the fact that it is based in Matlab, it is easily adaptable to simulations, making the transitions between a simulation to functional autopilot seamless. Fig. 19 depicts the SLUGS hardware with dual processors and the large Analog Devices sensor cube. The SLUGS hardware implements two processors (dsPIC33F), one dedicated to the flight control algorithm and the other dedicated to sensors and attitude estimation. As a research platform, a dual processor design allows for more systematic testing and increased processor resources for experimental algorithms.

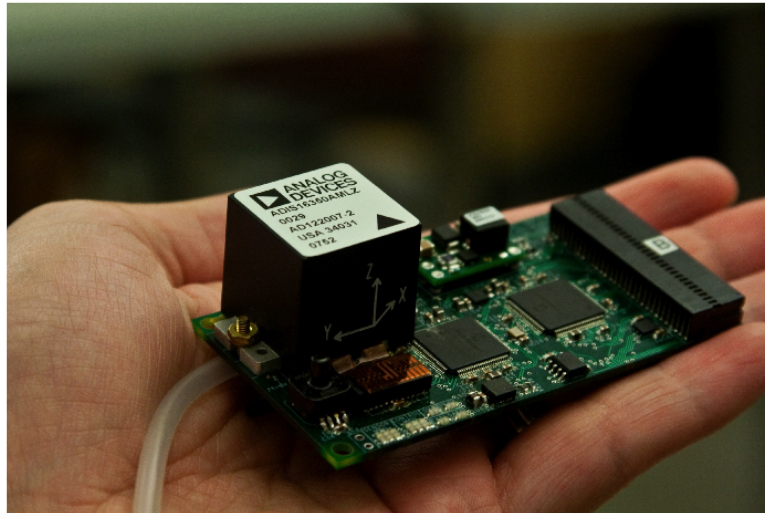


Figure 19: The SLUGS Autopilot with dual processors and the Analog Devices sensor cube [79].

The small form factor, visual programming language, and dual processor design makes SLUGS an ideal research platform for many autonomous aircraft. However, due to the limitations placed on the platform for size, some other functions were sacrificed. The SLUGS hardware platform, with its large dsPIC33F processors, only allows access to a small subset of the pins

available on the processors, some of which are extremely valuable to other platforms. For instance, the Quadrature Encoder Interface (QEI), which can be employed to calculate reaction wheel speed with the use of an encoder, is not easily accessible.

Even through the limitations on size cripple the SLUGS hardware on other platforms, it allows for a very powerful and versatile fixed wing UAV autopilot. Many of the advantages of SLUGS, such as the dual processor design, power regulation, and debugging LED bank were incorporated into the AECS.

3.2.2 ArduPilot

The ArduPilot is a popular commercial autopilot built by 3D robotics. The ArudPilot has a lot of support, due to the popularity of the Arduino platform. The ArduPilot is the closest of all the autopilots to being ready to fly out of the box. Within a few days, one could have this platform up and running (one of the perks of using a commercial platform). The ArduPilot also utilizes a shield architecture shown in Fig. 20. This shield architecture allows for a more versatile set of hardware. Older versions of the ArduPilot employs different shields to accomplish different tasks.



Figure 20: A shield (blue) mounted on the ArduPilot (red) demonstrating that all the electronics do not need to be placed on the autopilot [25].

Even with the shield architecture, this platform has its limitations. The ArduPilot is only equipped with a single processor, which should be enough for most applications, but does not have the added versatility and expandability of the dual processor design.

3.2.3 MatrixPilot

Finally, the MatrixPilot designed by William Premerlani [36] comes in two versions, a version designed by Nick Arsov (AUAV3) [28] (Fig. 21a) and the UDB5 from SparkFun (Fig. 21b) [43]. The AUAV3 employs the less powerful dsPIC30F, while the UDB5 uses the same dsPIC33F found on SLUGS. The AUAV3 has a much smaller form factor, making it easier to fit into smaller systems. The difference between the two platforms is the UDB5 has all the sensors built into it, while the AUAV3 requires a shield to add the sensors. The MatrixPilot has a large following and support from gentlenav [36] and DIY Drones [34].

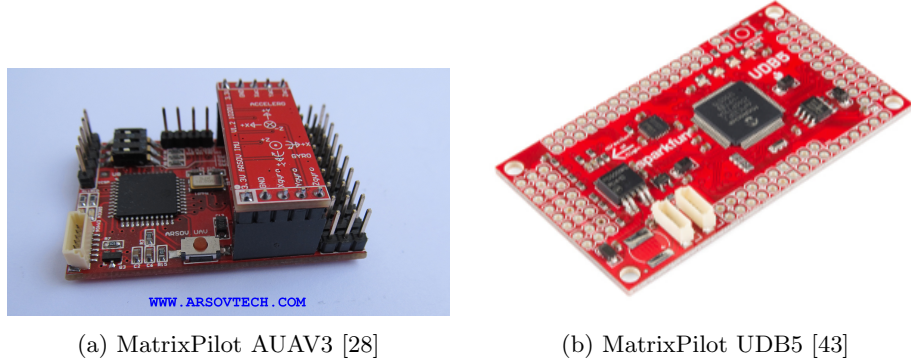


Figure 21: The MatrixPilot hardware options showing that only a limited number of chips are necessary for the control electronics.

The problem with this autopilot is that it lacks the versatility to fit the CubeSat application. The MatrixPilot, like SLUGS, has been developed as an aircraft autopilot. Both autopilots lack the general functions that are required for satellites, making it a less than favorable match for the control hardware. However, the removable sensor design is useful for the present application as this gives the user the ability to update the sensors as new and improved versions are developed.

3.2.4 Flight Controller Evaluation

The previous evaluation of various other FCS shows that none of the evaluated system conform to all the design criteria: size, power, environment and mission requirements. The NanoMind requires a three month lead time and costs about a quarter of the launch cost. Cost is also an issue for the Q6 and Pumpkin Pluggable Processor Modules. When comparing the operational lifetime of the system versus the cost of the project, it puts these solutions at a

disadvantage, especially for the Pumpkin Pluggable Processors (which were used on Colony I [88]). Note that the Pumpkin Pluggable Processors are outfitted with the same processors as SLUGS and the MatrixPilot.

The CUTE project used a PDA as the flight controller running a Windows operating system, but no PWM port is present for BLDC motor control [88]. The GeneSat project used a PIC18 as the flight controller which greatly reduces the development cost as compared to the commercial products, but lacks the computational power of similar terrestrial autopilots. It was discovered that the terrestrial autopilots were better suited for the control of a reaction wheel system due to their small form factor and accessibility. Unfortunately, the terrestrial autopilots are too specialized for aircraft and would be extremely difficult to convert to space applications. For this reason, it was decided that it would be best to develop a system more specifically tailored to the CubeSat reaction wheel application.

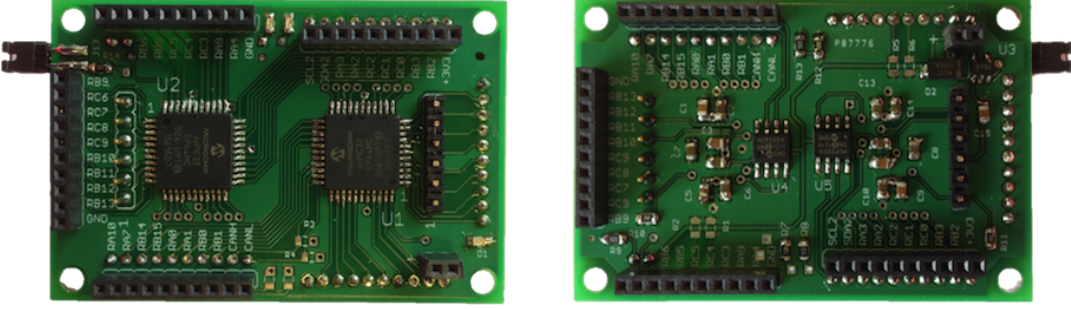
When designing the AECS hardware, several of the design aspects from the previously mentioned autopilots were taken into account. The AECS platform utilizes the dual processor design implemented on SLUGS. The processor of choice is the dsPIC33E, a 140Mhz processor employing only a fraction of the power of the dsPIC33F used on SLUGS.

From the ArduPilot, the AECS platform utilizes the shield concept making the platform much more versatile. Rather than making an autopilot for a single application, the platform is able to interchange its peripheral interface to fit any necessary application. This is extremely important for a system prototype because it allows for rapid development of hardware.

3.3 Main Control System Architecture

As mentioned in the previous section, the hardware developed in this thesis utilizes several design aspects from several different commercial autopilots. Of these features, the shield design is the most important to the AECS project. The shield design converts a general purpose development board into a specialized attitude control system. The Main Control System (main board) can be best described as a simple development board housing two Digital Signal Processor (DSP) units and power regulation. The limited amount of accessories allows for a smaller form factor as seen in Fig. 22a and 22b. The main board is only 6cm wide and 4cm tall making it smaller than most of the autopilots described in the Section 3.2: Flight Controllers.

The Main Control System is designed with two digital signal processors, one is dedicated



(a) Top of main board

(b) Bottom of main board

Figure 22: Control hardware named the main board, which utilizes a header system to add supporting electrical shields

to actuation control and another dedicated to sensors and attitude estimation. The actuation control processor is seen on the right side of Fig. 22a and is labeled U1. Similar to the SLUGS naming convention this processor is called the Control Digital Signal Controller or Control DSC for short. The pins on the Control DSC are all connected to the bottom of the main board. Header pins are employed to connect the main board to the control or sensor shields, like a sandwich. The control shield is on the bottom and sensor shield is on the top of the main board. Fig. 22a depicts the SENSOR DSC headers, while Fig. 22b depicts the CONTROL DSC headers.

The header design is utilized so all of the pins for both processors can be easily accessed. Along with the increased surface area, the shields are designed with rapid development in mind. This allows for rapid development of the shield rather than full flight control system, decreasing the production time of the system. Since each shield has access to all the pins on the processor, the potential for each shield is limited only by current technology.

The main board architecture is represented in Fig. 23, which also shows the flow of data between the main board and shields. The main board depicted in the middle of Fig. 23 houses the CONTROL and SENSOR DSCs. Both processors communicate via an Inter-Integrated Circuit (I^2C) communication bus. This is a master-slave communication architecture in which the master (SENSOR DSC) initiates all conversations to the slave (CONTROL DSC). This communication bus is only used for the two DSP controllers, to relay attitude data.

Communication with the control shield is limited to the CONTROL DSC. The control shield houses all the BLDC control electronics. The control shield is also used for power regula-

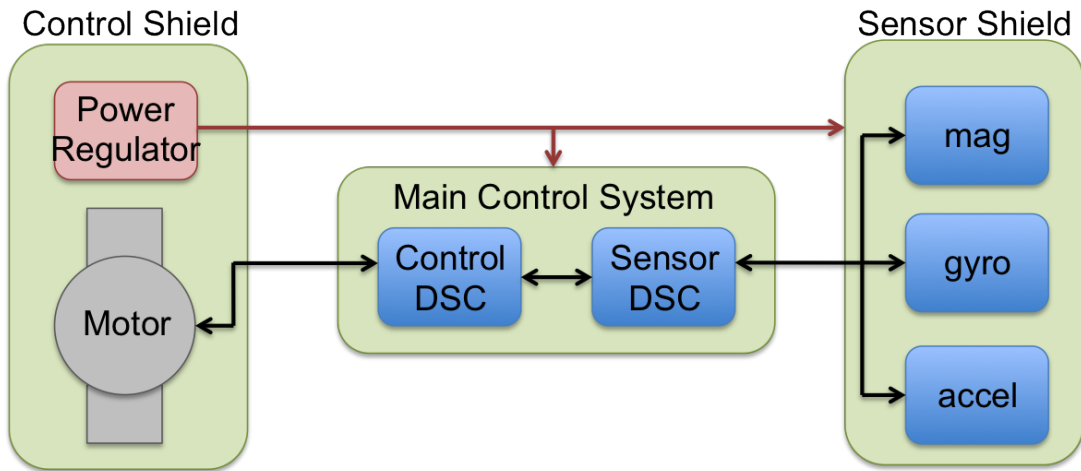


Figure 23: Main board architecture block diagram showing the AECS hardware in Fig. 22 and their connections with the Control and Sensor Shields.

tion and supplies power to the main board and sensor shield (as indicated by the red arrows in Fig. 23), it should be noted that each board (control shield, sensor shield, and main board) has its own on board power regulator. However, the regulator on the main board should be disabled if the main board is being used with either the control or sensor shield. Communication with the sensor shield is limited to the SENSOR DSC via a dedicated I²C bus. This bus is used primarily for communication between the SENSOR DSC and the inertial measurement sensors (accelerometer, magnetometer, and gyroscope), shown in Fig. 23. Terrestrial sensors are used do to cost, because it will not be testing in space.

3.3.1 Processors Specifics

The system is designed as a research platform on a remote system, so the efficiency and speed of the processor is vital to perform complex tasks. However, as the speed of the processor is increased, the power consumption increases proportionally. A balance between the performance and power draw is needed.

To get a better understanding of the performance required for the processors, an important task will be evaluated: attitude estimation. The attitude estimation process consists of four major steps, which are described in more detail in the Section 4: Attitude Estimation. First, the processor must read in data from the sensors. Once the data has been read, the data must be propagated to update the attitude estimator. This step involves matrix multiplication and

addition. Once the attitude estimator has been updated, it must be corrected for gyro drift that is present on the sensor data. This step involves filtering the gyro data to compensate for gyro drift. This process is repeated every 20ms. This high update rate is required to continuously update the orientation of the CubeSat.

The time it takes to perform this process is dependent upon the mathematical operations that are taking place and the data types of the mathematical operations. All of these factors must be taken into account when selecting a processor. Attitude Estimation using the Direction Cosine Matrix (DCM) requires thirty-six floating point multiplication operations and three trigonometric functions [52]. On the Microchip dsPIC, a float multiplication function requires 109 instructions, while arccosine and arcsine function require 478 and 363 instructions respectively [22]. This equates to roughly 5k instructions per attitude propagation. The filter process described in Section 4: Attitude Estimation requires thirty multiplications, eighteen additions/subtractions, nine divisions, and three square roots. This requires approximately 10k instruction. Assuming it takes 1ms to acquire and process the sensor data, a minimum 800kHz instruction cycle is necessary to complete the attitude estimation process within the 20ms period.

Taking the these parameters into account the dsPIC33E processor was chosen. This processor is a Digital Signal Processor, similar to the dsPIC33F employed on the Pumpkin Pluggable Processor, SLUGS and the MatrixPilot, but it is a newer version that is capable of processing speeds of 70 MIPS, with a typical power consumption of 41mA [26]. The dsPIC33F is only capable of 40MIPS at a current consumption of 84mA [23]. This means that the dsPIC33E can operate at twice the speed of the dsPIC33F while consuming half the amount of power. On the other hand, the ATXMEGA16A4 is capable of performing at about 32MIPS at an astonishingly low current consumption of 5mA [5].

From this comparison, the ATMEL processor is superior in terms of power efficiency, but the dsPIC33E has two features that makes it the processor of choice. The dsPIC33E has pin remapping capabilities, in which almost any peripheral can be mapped to almost any pin on the processor. This is important on a small processor because of the limited number of pins, which allows the user to select the peripheral they require rather than a peripherals they do not need. The other feature is the Digital Signal Processing Engine on the dsPIC33. This allows for optimized mathematical computation that will greatly reduce the time required for mathematical operations.

3.3.2 Power Rails and Regulation

The AECS hardware has several electrical devices that require regulated power, such as the on-board processors and processor peripherals. On the other hand the power supply for the Faulhaber 1509 Brushless DC motor does not need to be finely regulated due to the fact that electric motors are electrically noisy to begin with. Due to their noisy nature, the motors can be directly connected to the battery or power supply.

Other supply voltages required are a regulated +5 and +3.3 voltage rails. These two voltage rails are necessary for the attitude control hardware. The +5 voltage rail is used for the CAN bus and current sensor, however the remaining integrated circuit operate off the +3.3 voltage rail, including the processors, sensors.

In order to keep the current draw of the regulator low, a combination of switching and linear regulators are employed. Switching regulators are much more efficient than linear regulators, but they produce a much noisier output signal. This signal might be acceptable for some integrated devices, but devices like wireless communication modules and processors require a cleaner power supply.

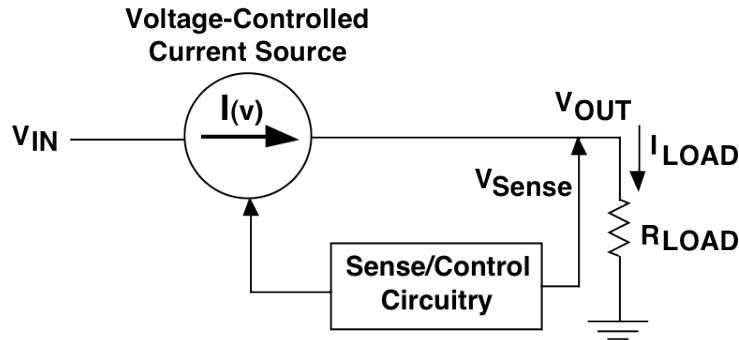


Figure 24: Block Diagram of a generic linear regulator [90].

Linear regulators are relatively simple devices that supply a stable DC output voltage by dissipating excess power. Since the linear regulator acts like a voltage-controlled voltage divider, the excess power is dissipated as heat energy as heat. In terms of the example, +7 of the +12 input volts are converted into heat energy. If 1A is being drawn by the load, 7W would be converted into heat energy. This is the reason why linear regulators have problems with efficiency. Therefore, it is necessary to reduce the amount of power converted into heat energy.

This can be done by reducing the input voltage.

One method of reducing the input voltage is to utilize the high efficiency of switching regulators. A switching regulator, as the name implies, switches the input signal on and off at an extremely high rate. Fig. 25, is a simplified depiction of the switching regulator. In this circuit, when the switch is closed, current rushes into the inductor, where it is stored as a magnetic field. Then, when the switch is opened, the magnetic field in the inductor collapses while trying to sustain the voltage across the inductor. The inductor creates a negative voltage on the left side of the inductor, which is squashed by the diode. On the right side, a positive voltage charges the capacitor, which then outputs a voltage at the output terminal.

The switching regulator is considered a high efficiency device because the circuit elements such as the diode, inductor, and capacitor ideally have no energy loss. However, in practice these circuit elements dissipate energy, but compared to resistive elements their losses are negligible. By opening and closing the switch at high frequencies, energy is transferred to the output producing an output proportional to the duty cycle. The output voltage is lower because of limited current flow due to the magnetic field created by the inductor. As the inductor charges, a magnetic field is generated opposing the flow of current. This properly reduces the input voltage without dissipating energy.

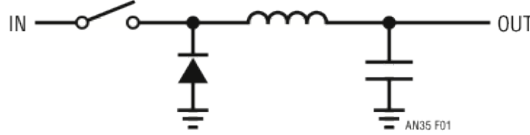


Figure 25: Equivalent functional diagram of a switching regulator [95].

The switching regulator unfortunately has a drawback. It creates digital noise on the signal. Digital noise refers to the high frequency fluctuations present on the output signal, which could cause problems for sensitive devices such as sensors and processors. Therefore, it is common practice to employ both switching and linear regulators. The switching regulator reduces the supply voltage from the battery (+12V) down to a much lower value (+5V). This voltage is then input into the linear regulator to supply to the sensitive circuitry, a voltage of +3.3V. By reducing the battery voltage from +12V to +5V, the amount of energy dissipated into heat is greatly reduced, conserving power.

3.4 Shield Concept

The shield concept is adapted from the Arduino shield paradigm. The shields allow for specialization of a generic hardware platform. The hardware is developed to be a generic flight control system for use in any autonomous platform. By adding a shield (control or sensor shield), the main board can be converted into a platform specific control system.

The autopilot hardware for land based platforms, such as cars, require elements such as forward and backward motor control, distance measurement, steering control, etc. Air-based systems (including satellites), on the other hand, require different sensors to measure their speed and position. Most platforms use GPS for position (satellite need unlocked GPS units to operate above the 60k altitude limit or faster than 999 knots [11]), but ground-based systems might be deployed in areas where GPS is obscured; in aerial platforms this is not an issue. The actuators and actuation for ground and air systems are different. Airplane platforms are not able to fly backwards or stop in midair. Due to these different dynamics, it is understandable that a single hardware platform is insufficient for every type of vehicle.

Some similarities exist between air and ground based platforms, which can be exploited. One such example is an attitude control system that is not dependent upon GPS. This allows for indoor testing of the attitude control system without creating a mock GPS signal. Testing satellites or aircraft is expensive and difficult to do, but testing ground vehicles is relatively simple. Creating a system that can be deployed on various vehicle platforms, makes it easier to test some of the functions specific to satellites or CubeSats.

Creating shields specific for the platform and the application allows the user to create a specialized platform using only the peripherals necessary for their application, thereby reducing the size of the autopilot. These specializations are necessary in space-limited applications such as the CubeSat. Shield specialization is advantageous over autopilot hardware specialization because the core components of the design always stay the same; the performance, software architecture, and hardware layout are always consistent.

3.4.1 Interchangeable Hardware

The shields are built around the concept of interchangeable hardware. By incorporating the interchangeable hardware into the AECS platform, the pin remapping feature on the

dsPIC33E microcontroller can be utilized. Microchip Inc. has developed a remappable peripheral system that allows the user to map the peripheral functions, such as the CAN BUS, UART, Input Capture, etc. to almost any pin on the microcontroller. The remappable peripheral system is utilized by the shields in that all of the remappable pins are routed to the shields. This allows for access to almost all peripherals available on the microcontroller. Thus, each shield is capable of completing a variety of different tasks. Utilizing the remappable pins allows access to several peripherals without making each pin on the microcontroller available. The interchangeable hardware feature of the platform design allows for quick development and testing, allowing the user to readily change the peripheral hardware as required.

During the development of the CubeSat hardware and software, the platform underwent several changes. These changes ranged from the power regulation requirements to the changes in motor control hardware. By using the shield system, it was possible to change design aspects without completely scrapping the CubeSat or main board designs. In the initial stages, the Faulhaber 1509 motor was going to be used for testing, but it was believed that a larger, more powerful motor would be better suited to test the attitude control algorithms on the ground. This change was made by developing a new control shield (all other hardware remained the same), therefore, reducing the development time and cost significantly.

3.5 SENSOR Shield

The shield system has a single application, providing the peripheral electronics for the CONTROL and SENSOR DSCs. More information on the control shield can be found in Section 5: BLDC Motor Control Shield. This section will cover the aspects related to the sensor shield. The sensor shield is designed to attach sensors to the SENOSR DSC. The SENSOR DSC calculates the attitude of the CubeSat Platform. Specifics of the attitude estimation software can be found in Section 4. The sensor shield provides the necessary hardware for the SENSOR DSC to interface with the sensors, allowing for the orientation to be measured.

The orientation of the CubeSat Platform is estimated using microelectromechanical systems (MEMS) gyroscopes that measure the rotation rate of the platform. This value can then be integrated to produce the rotation angle. Other sensors are used to provide reference vectors to compensate for errors in the gyro measurement. Due to the integration of the gyroscope signal, any error in the gyro measurement will be accumulated and grow over time. For this

reason, reference vectors are needed to calculate the error in the gyroscope signal.

Due to the fact the developed AECS hardware will not be deployed in orbit, terrestrial reference sensors will be used. Popular sensors for attitude error estimation are accelerometers, GPS, and magnetometers [86]. The GPS and magnetometer are commonly used to measure the direction or yaw orientation of the platform. GPS provides a position and velocity component, whereas the magnetometer provides a measure of the Earth's magnetic field [52]. The accelerometer uses the Earth's magnetic field as a reference to determine its yaw orientation. The magnetometer uses the Earth's gravitational field as a reference to correct for error in the roll and pitch estimates [52] [85] [89].

The sensor shield utilizes a gyroscope, accelerometer, and magnetometer for attitude estimation. These sensors were not placed directly onto the sensor shield, but instead breakout boards were used. This allows for easy assembly and replacement if a sensor broke. The sensor breakout boards are the RED boards shown in Fig. 26. The sensor shield uses Inter-Integrated Circuit (I^2C) communication equipped sensors, allowing for easy replacement of sensor hardware if necessary. An extra sensor header is added to the sensor shield allowing for extra sensor breakout board to be connected to the shield, as indicated by the red circle in Fig. 26.

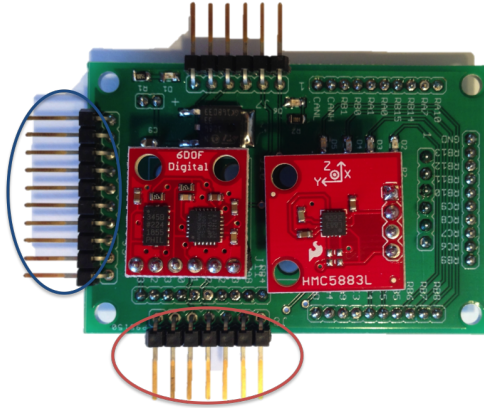


Figure 26: Top of the SENSOR Shield board showing the sensor breakout boards (red); used to supply the supporting electronics to the SENSOR DSC

In order to utilize the pins available on the SENSOR DSC, ten remappable Digital I/O pins are also mapped to the sensor shield. During the testing phases, this header is utilized as a communication port, which is used to relay the status of the SENSOR DSC. The Digital I/O port is indicated by the blue circle in Fig. 26.

3.5.1 SENSOR Shield Mating

The sensor shield is employed as a hardware platform for the SENSOR DSC and is utilized by mating the sensor shield to the top of the main board. Fig. 27a, depicts the bottom layer of the sensor shield. The colored circles in Fig. 27a, correspond to the colored circles in Fig. 27b. These are the mating headers for the sensor shield.

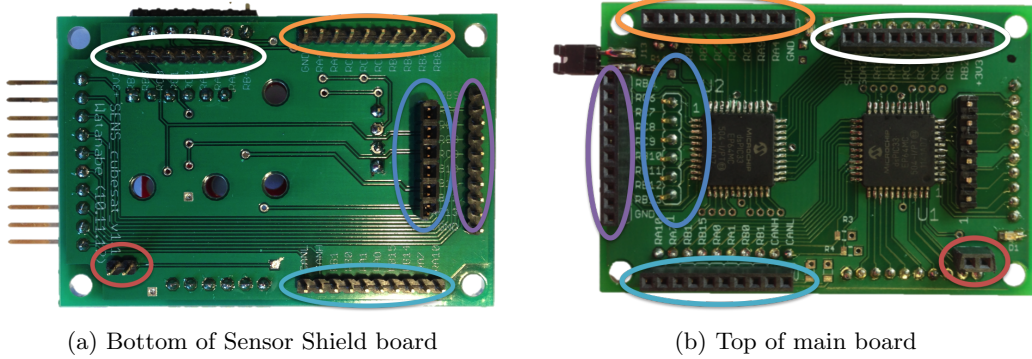


Figure 27: Main board hardware showing the mating connections between the sensor shield and main board.

The small two pin headers in RED are the power headers, these are used to supply a +5V source from the main board to the sensor shield. This is used to power the on-board regulator for the sensor shield. The regulator is used to isolate the digital sensor power supply from other components. This design choice was made in case actuators are directly connected to the main board. Adding the extra regulator to the sensor shield improves the noise performance of the sensors.

The BLUE header, which is larger than the others is used for programming purposes. If the main board does not use the sensor shield, this header is used to program the SENSOR DSC, but if the sensor shield is mated with the main board this header is blocked. Therefore, the programming header is routed on the sensor shield so the user can access the program header while the sensor shield is connected.

The remaining headers are all used for the SENSOR DSC peripherals. The SENSOR DSC is a forty-four pin microcontroller, with thirty-six digital/peripheral pins, all of which are routed through these four headers. Routing all the digital/peripheral pins through these headers give the sensor shield access to all the functionality of the SENSOR DSC.

3.6 Summary

To summarize, the electronics and actuators used to support the attitude control system must fit within the size limitation of the CubeSat specifications. CubeSats are divided into units, where one UNIT (1U) is a 10 cm x 10 cm x 10 cm cube that must contain all parts of the satellite during lift off (see Fig. 14). The flight control electronics and actuators have all been placed within a 1U CubeSat form factor. The actuators of the attitude control system occupy a significant amount of space, only leaving a volume of 210cm³ for the control electronics.

The attitude control system is also limited in power consumption. Since a satellite is a remote system, it is impossible to perform maintenance on the system. It is estimated that in total the control electronics excluding actuators will require 1W of power and that 5W will be harvested from the solar panels. As a research platform, it is important to emphasize the processor performance of the system. For this reason, the dsPIC33E was chosen because of its clock frequency and low power consumption. This processor also has many peripherals making it easy to adapt to many different applications, and flexible for research and development.

4 Attitude Estimation

Attitude defines the orientation of the body frame with respect to a reference coordinate system. Unfortunately, the attitude of the body frame cannot be measured, it must be estimated using an attitude estimator. The estimator uses multiple sensor measurements to define the best estimate of the orientation. Several attitude parameterization methods exist to describe the rotation between the body and the reference frames, such as Euler Angles, the Direction Cosine Matrix (DCM), and Quaternions. For more details about these methods see [52]. Our prototype uses the DCM to describe the attitude of the CubeSat. The body frame of the CubeSat is defined in Fig. 28. Fig. 28 depicts the z-axis protrudes from the top, and the x and y axes protrude from perpendicular faces of the CubeSat.

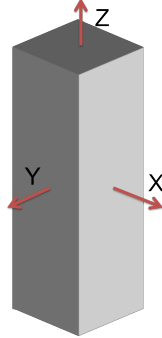


Figure 28: CubeSat body frame coordinate system.

The local body frame described in Fig. 28 is then compared to a space reference frame. Several reference frames exist for different space applications. Earth Centered Earth Fixed (ECEF) and the Orbital Coordinate systems are just a few [67]. The ECEF coordinate system places the origin of the coordinate system at the center of the Earth, with the x-axis pointing towards the Aries constellation and the z-axis protruding North towards the North Star as depicted in Fig. 29a. The x, y, and z axes of the satellite are then measured with respect to the ECEF coordinate system. The roll, pitch and yaw axes can also be represented in Fig. 28 as rotation about the x, y, and z axes respectively. An attitude estimation algorithm is then used to represent rotations between the ECEF frame and the satellite body.

In order for the attitude of the satellite to be estimated, sensor measurements are required to identify the orientation of the satellite with respect to the reference coordinate frame. Several

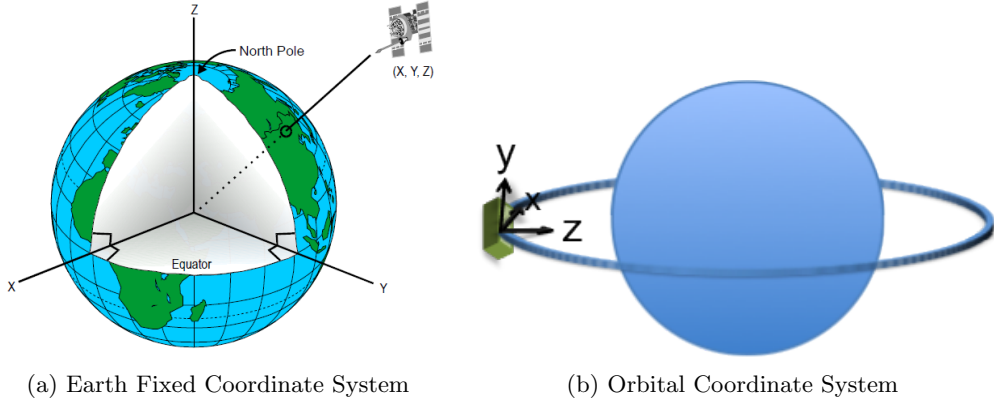


Figure 29: Space based coordinate systems [9]

sensors exist specifically for space applications, such as star, Sun, and Earth (limb) trackers, which detect the presence of the previously specified objects. For instance, star trackers can be employed to orient the satellite with respect to Aries and the North Star in the ECEF coordinate system.

As our prototype focused primarily on the development of the attitude control hardware, the prototype system does not employ the satellite coordinate system or the associate satellite sensors. This will be left for future revisions of the system via a new sensor shield. This choice was made due to the fact the prototype cannot be tested in space, making use of satellite sensors such as star trackers cost prohibiting. Instead, a conventional aircraft coordinate system and sensors will be implemented due to the availability of sensors and cost considerations. The goal of the attitude estimation algorithm is to aid in the demonstration of precise attitude control. Even though the reference sensors and coordinate systems are dissimilar in aircraft and space vehicles, the general attitude estimation algorithms are similar in that they both must estimate the orientation of the vehicle with respect to a reference frame. Therefore, demonstration of an attitude control system employing aircraft coordinate systems and reference sensors is applicable to the overall goal of this project.

As previously mentioned, the purpose of the prototype testbed is to demonstrate the functionality of the attitude control system. Evaluation of the attitude control system involves measuring the orientation of all three axes, even though the testbed is limited to yaw axis orientation control. The full 3D attitude is being extracted to measure the computational load placed on the SENSOR DSC. The North-East-Down (NED) coordinate system was used

along with inertial sensors such as accelerometers and magnetometers. Adaptations to other coordinate systems can easily be done utilizing the general DCM algorithm implemented on the AECS platform (the Direction Cosine Matrix (DCM)). The DCM is a rotation matrix converting the sensor orientation readings from the reference coordinate system to the body frame.

The attitude control algorithm described in this section follows the approach specified by Premerlani and Bizard [86]. The DCM uses of gyroscopic sensors to measure the rotation rate of the platform. This measured rotation rate is then propagated to update the DCM. The general architecture of the attitude estimation algorithm can be located in Fig. 30, which shows the flow of data. In Fig. 30, data originates from the gyroscopes and flows into the transformation matrix. The output is a 3x3 matrix, the DCM (R_i^b), which translates from the inertial frame (Earth Coordinate System) to the body frame (cubesat platform), from which the Euler angles can be extracted: roll, pitch, and yaw. The Euler angles are a very intuitive way of presenting the orientation of the platform. This output is called the open loop orientation. In an ideal situation where the gyroscope signals are perfect (no noise), the open loop solution would perfectly track the attitude. Gyroscopes however, are not perfect and an error signal is accumulated over time.

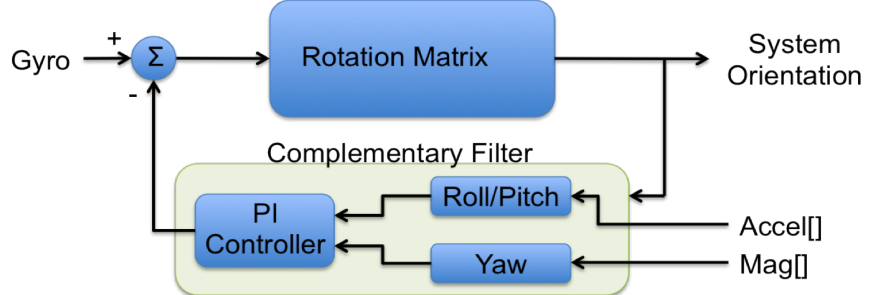


Figure 30: Attitude Estimator Block Diagram showing the flow of data; extracting the rotation rate from the gyroscopes and converting the data into the system's orientation [86].

For this reason a closed loop attitude estimator is implemented. Closing the loop means that the generated DCM is compared with other sensors. By comparing the DCM with other sensors, an error term can be generated. In order to generate the error, at least two independent references are required. Once the error has been calculated, a Proportional Integral (PI) feedback controller is employed to compensate for the gyro drift in the DCM. This process is repeated, and over time, the error decreases.

The general algorithm for computing the DCM with gyros is to assume that the gyros produce no errors generating a preliminary estimate of the DCM. Once the preliminary estimate has been found, the next step is to account for gyro errors. This is done with the renormalization of the DCM and the drift cancellation. Attitude estimation can thus be summarized into three steps: (1) use gyro data to update the DCM (section 4.1), (2) reorthonormalize the DCM (section 4.2), and finally (3) use the complementary filter to compensate for errors (section 4.3).

4.1 Transformation Matrix

The Direction Cosine Matrix is a transformation matrix that transforms one coordinate system, the inertial frame (c_i), to another coordinate system, the body frame (c_b). The body frame is the x, y, and z-axis of the CubeSat, and the inertial frame is the x, y, and z-axis of the Earth coordinate system. The transformation matrix or DCM is represented by R_i^b and is used to transform the vector c_i to the vector c_b . This can be written as:

$$c_b = R_i^b c_i$$

$$c_b = \begin{bmatrix} x_b \\ y_b \\ z_b \end{bmatrix} \quad R_i^b = \begin{bmatrix} r_{xx} & r_{yx} & r_{zx} \\ r_{xy} & r_{yy} & r_{zy} \\ r_{xz} & r_{yz} & r_{zz} \end{bmatrix} \quad c_i = \begin{bmatrix} x_i \\ y_i \\ z_i \end{bmatrix} \quad (8)$$

The columns of the DCM represent the mapping from the inertial frame axes to the body frame and the rows are the mapping from the body frame axes to the inertial frame [52]. The DCM can also be used to transform the body frame to the inertial frame by utilizing the transpose of R_i^b , since $R^T = R^{-1}$.

Propagation is the integration of the parameterization method (in this case the DCM). Several methods for propagation exist including Forward Euler and the Matrix Exponential [52]. An approximation of the Matrix Exponential was used to propagate the DCM. However, the full propagation equation can be found in Eq. 9 [58] [52]. This shows that the updated DCM is a function of the Matrix Exponential of the rotation rate anti-symmetric matrix expressed in

Eq. 10 and the previous DCM [58] [52]. The generic Matrix Exponential is expressed in Eq. 11 [80].

$$R(k + \Delta T) = e^{-[\omega_x]\Delta T} R(k) \quad (9)$$

$$e^{A\Delta T} = I + A\Delta T + \frac{\Delta T^2}{2!} + \dots \quad (10)$$

$$[\omega_x] = \begin{bmatrix} 0 & -\omega_z & \omega_y \\ \omega_z & 1 & -\omega_x \\ -\omega_y & \omega_x & 1 \end{bmatrix} \quad (11)$$

An rough approximation of the DCM defined in Eq. 9 can be made if it is assumed that ΔT is small and the value of ΔT^i is zero for all $i \geq 2$. This simplifies the DCM equation such that $e^{A\Delta T} = I + A\Delta T$. This rough approximation is expressed in Eq. 12 [86]. This simplification effects the DCM, making it lose its orthonormal property. Therefore, the DCM equation needs to be reorthonormalized as expressed in Section 4.2: Renormalization.

The two error terms (e_y and e_{rp}) in Eq. 13 represent the yaw and roll/pitch errors respectively. These errors are generated from the complementary filter, as seen in Fig. 30, and are subtracted from the gyroscope input. The first term, $\omega_i(t)dt$, of Eq. 13 is the rotation rate measured by the gyroscopes multiplied by the time step (dt). The time step dt is constrained by the update rate of the sensors and the approximation $\sin(\theta) = \theta$. For simplicity the sensors update rates were synchronize; setting the upper limit of dt to 75Hz. This is the update rate of the slowest sensor, the magnetometer.

$$\mathbf{R}(t + dt) = \mathbf{R}(t) \begin{bmatrix} 1 & -d\theta_z & d\theta_y \\ d\theta_z & 1 & -d\theta_x \\ -d\theta_y & d\theta_x & 1 \end{bmatrix} \quad (12)$$

$$d\theta_i = \omega_i(t)dt - e_y - e_{rp} \quad i = x, y, z \quad (13)$$

The approximation $\sin(\theta) = \theta$ must be valid in order to use Eq. 12. A system update rate of 50Hz was chosen to satisfy both requirements and allow 20ms for the SENSOR DSC to complete the attitude calculations. For completeness the approximation $\sin(\theta) = \theta$ will be evaluated. The rotation rate of a typical CubeSat could be approximately $5^\circ/\text{s}$, which is comparable to a “fast” satellite slew. This means that the estimated change in the orientation angles can be approximately 0.1° in 20ms. Evaluating $\sin(\theta)$ for the yaw angle $\theta = 0.1$, shows that the assumption is valid, as seen in Eq. 14.

$$\sin(0.1) = 0.09983 \quad (14)$$

4.2 Renormalization

Once the DCM has been updated using Eq. 12, it starts to accumulate errors and the DCM is no longer orthonormal. To emphasize the point, assume that $R(0)$ is the Identity Matrix and all three of the gyros measure a rotation rate of 0.01rad/s , given a sampling rate of $dt = 20\text{ms}$, at time $t = 1$, this gives a $d\theta_x = d\theta_y = d\theta_z = 0.0002$. $\mathbf{R}(1)$ is given in Eq. 15.

$$R(1) = \begin{bmatrix} 1 & -0.0002 & 0.0002 \\ 0.0002 & 1 & -0.0002 \\ -0.0002 & 0.0002 & 1 \end{bmatrix} \quad (15)$$

Observing Eq. 15, it is evident that the norm of the rows and columns are no longer unity. To correct this, two steps are required: first the DCM needs to be made orthogonal and second it needs to be normalized. In order to make sure the DCM orthogonal the dot product and cross product are utilized. The dot product of two vectors, \vec{a} and \vec{b} is defined as $\|a\|\|b\|\cos(\theta)$. This property can be applied to the \vec{x} (first column) and \vec{y} (second column) columns of the DCM, which should be performed every time the DCM is updated. As demonstrated in Eq. 15, the change in the \vec{x} and \vec{y} vectors are minimal due to the short sample time dt . Therefore, it is assumed $\|x\| \cong \|y\| \cong 1$. This means the dot product of \vec{x} and \vec{y} becomes $\vec{x} \cdot \vec{y} = \cos(\theta)$. The dot product can be used as a measure of error and will be defined by Eq. 16.

$$e_n = \vec{x} \cdot \vec{y} = \cos(\theta) \quad (16)$$

$$\begin{aligned}\vec{X}_{ortho} &= x - \frac{e_n}{2}y \\ \vec{Y}_{ortho} &= y - \frac{e_n}{2}x\end{aligned}\tag{17}$$

The error term can then be used to normalize the \vec{x} and \vec{y} vectors by subtracting the error term from both the \vec{x} and \vec{y} vectors, creating a new vector called \vec{X}_{ortho} and \vec{Y}_{ortho} , respectively. Eq. 17 shows the equations for both \vec{X}_{ortho} and \vec{Y}_{ortho} [86]. In the \vec{X}_{ortho} equation, the \vec{x} vector is being subtracted by half the error term times the \vec{y} vector, creating two orthonormal vectors. This leaves only \vec{Z}_{ortho} , this vector can be obtained using the cross product, as seen in Eq. 18 [86].

$$Z_{ortho} = X_{ortho} \times Y_{ortho}\tag{18}$$

Earlier it was assumed the magnitudes of X_{ortho} , Y_{ortho} , and Z_{ortho} were equal to one; however, this was proven to only be an approximation in Eq. 15, so over time, the error will accumulate and this assumption will no longer hold. Therefore, it is important to normalize the DCM so this approximation will stay valid. The \vec{X}_{ortho} , \vec{Y}_{ortho} , and \vec{Z}_{ortho} vectors need to be normalized every DCM update cycle to keep the assumption used for the orthogonality calculation valid ($\|x\| \cong \|y\| \cong 1$). The general equation to normalize the orthogonal vectors can be found in Eq. 19. This method requires the use of a square root operation which will slow down the attitude estimator, costing an additional 493 instruction cycles [22]. The additional computational load is not an issue due to the high operating frequency of the SENSOR DSC.

$$\begin{aligned}\hat{v} &= \frac{v}{\|v\|} \\ \|v\| &= \sqrt{v_1^2 + v_2^2 + v_3^2}\end{aligned}\tag{19}$$

4.3 Complementary Filter

The complementary filter is used to (1) measure the orientation error and (2) compensate for it with a feedback controller. Without these two components the system is “open loop”, meaning it is not capable of self-correction. While describing the rotation matrix, it was assumed that the system was open loop and implemented with perfect sensors that are accurate and produce no noise. In reality these issues need to be addressed, and the complementary filter is

one popular method.

The complementary filter is conceptually very simple. It compares at least two references with two different characteristics, for example, the gyroscopes and magnetometer. The gyroscopes produce a high frequency output of the rate of rotation, whereas the magnetometer produces an absolute reference with respect to the Earth's magnetic field. The Earth's magnetic field vector changes slowly over time, but is assumed to be constant, making it ideal as a reference signal. Having an inertially stable reference vector allows the gyroscopic drift to be measured. The accelerometer is used because it estimates gravity vector which is an absolute references. The gyro drift is measured by the drift detector, which has been broken up into two parts: Yaw Compensation and Roll/Pitch Compensation. It is broken into two parts based on the sensors being used, the magnetometer and accelerometer respectively.

4.3.1 Yaw Compensation

Yaw is the rotation about the z-axis and is depicted in Fig. 31 as the angle ψ . The reference vector for yaw compensation is measured by the magnetometer because it projects a reference vector onto the x-y plane. The magnetometer generates a vector containing the x, y, and z components in the vector **mag[]**. The **mag[]**, is a measure of the magnetic field in the body frame. The magnetic field vector is used to find the actual orientation of the x-axis of the body frame. This is represented in Fig. 31 as the COG vector (Course Over Ground). The x-axis of the body frame as estimated by the DCM is represented as X_b and X_{bp} , the projection of the body frame onto the x-y plane. The error in the body frame's x-axis orientation is then measured as $\psi_e = \psi_m - \psi$, where ψ_m is the yaw angle measured by the magnetometer and ψ is the yaw angle estimated by the DCM.

Instead of measuring the projection of the body frame in the x-y plane, the cross product can be used to measure the error, ψ_e . In order to solve for the error, the cross product must be taken between the projection of the magnetic field vector COG and the x-axis of the body frame X_b . The magnetic field vector is described by **mag[]** and the x-axis of the body frame is described by the first column of the DCM. When the cross product of COG and X_b is taken, the result is a component about the z-axis. Therefore, the cross product is the rotation error

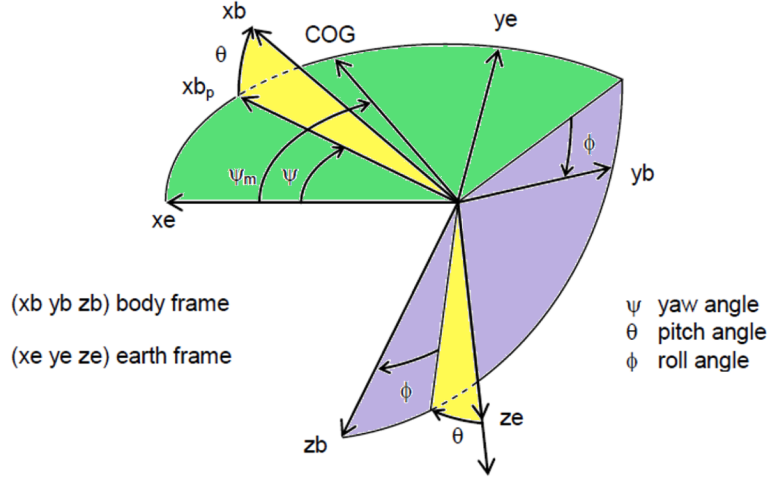


Figure 31: Diagram of the yaw rotation and error on the x-y plane (green) [86].

about the z-axis also known as yaw error, expressed in Eq. 20 [86].

$$\psi_e = COG \times Xb \quad (20)$$

4.3.2 Roll/Pitch Compensation

Roll/pitch compensation is very similar to yaw compensation except that the accelerometer will be used as the reference rather than the magnetometer. Similar to yaw compensation, roll/pitch compensation uses the cross-product to evaluate the error vector (θ_e). However the yaw and roll/pitch compensation differ in that the magnetometer directly measures the magnetic field, whereas the accelerometer measures acceleration minus gravity, as expressed in Eq. 21 [52]. The gravity vector (g) can be estimated by subtracting the inertial acceleration (a_i) from the measured acceleration (a_m). The inertial acceleration can be estimated by evaluating the cross product of the angular velocity (provided by the gyroscopes) and the velocity, as expressed in Eq. 22 [86]. Error in the gravity estimate can be seen in Fig. 32 as $\Delta\theta$ (gravity pitch error) and $\Delta\phi$ (gravity roll error).

$$a_m = a_i - g \quad (21)$$

$$g = a_i - a_m$$

$$a_i = \omega \times v \quad (22)$$

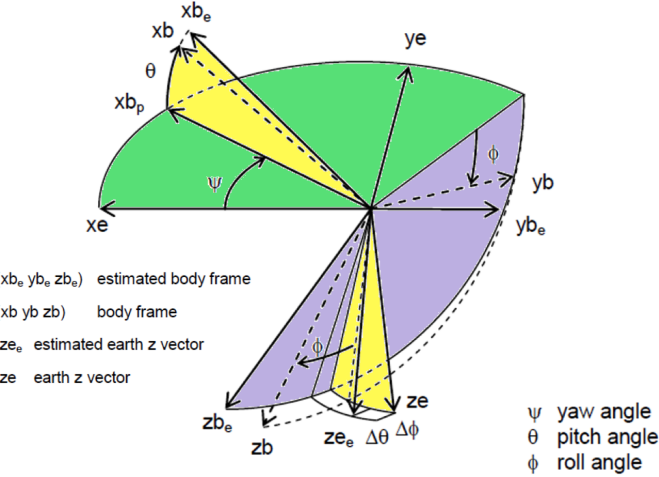


Figure 32: Diagram of roll and pitch. Pitch rotation is on the x-z plane (yellow) and roll rotation is on the y-z plane in (purple) [86].

Fig. 32 shows the actual platform orientation as X_b , Y_b , and Z_b as determined with the aid of the reference sensors (magnetometer and accelerometer). The pitch angle (θ) is the angle between Z_b and Z_e (z-axis Earth Frame) on the x-z plane shown in yellow. The error in the pitch angle is represented as the projection of the angle between Z_{b_e} (DCM estimate of the z-axis of the body frame) and Z_b (z-axis of the Actual Orientation) projected on the x-z plane. The pitch error can also be observed between X_b and X_{b_e} (as seen in Fig. 32). The roll angle (ϕ) is the projection of the angle between the Z_b and Z_e vectors on the y-z plane as shown as the purple region. The error in the roll angle is a measure of the angle between Z_{b_e} and Z_b on the y-z plane. The roll error can also be observed between Y_b and Y_{b_e} (as seen in Fig. 32).

The roll/pitch error is measured by evaluating the cross product of the normalized gravity vector Z_e and the z-axis of the body frame Z_b , as expressed in Eq. 23 [52] [86]. Evaluation of the cross product produces an error vector (θ_e) perpendicular to Z_e and Z_b . Ideally the error vector should align with the x-axis of the body frame. Misalignment between the two vectors is the roll/pitch error.

$$\theta_e = Z_e \times Z_b \quad (23)$$

4.3.3 Feedback Controller

With the error in the Direction Cosine Matrix accounted for by the drift detector, the feedback controller can now remove the errors from the estimated attitude signal. The feedback controller functions by taking a fraction of the error and feeding it back into the system. The error term is subtracted from the input (the gyroscope reading) and a new compensated input is applied to the DCM (R_i^b), as seen in Fig. 30 and Eq. 13. The DCM update equation (Eq. 13) has been manipulated to represent the feedback control input. In Eq. 24 the yaw and roll/pitch errors have been replaced by the PI control signals [86].

$$d\theta_i = \omega_i(t)dt - \epsilon_p(t) - \epsilon_i(t) \quad i = x, y, z \quad (24)$$

$$\begin{aligned} \epsilon_p(t) &= K_p * (\psi_e + \theta_e) \\ \epsilon_i(t) &= \epsilon_i(t-1) + K_i * (\psi_e + \theta_e) * dt \end{aligned} \quad (25)$$

The implemented feedback controller is a PI or Proportional Integral controller. The proportional term provides a linear feedback term that is proportional to the error generated by the system. Manipulation of the proportional term affects the damping ratio and natural frequency of the system response. The integral term allows for bias rejection, driving the steady state error to zero.

In accordance with William Premerlani, a single PI controller was used for the roll/pitch and yaw correction. Premerlani states that given enough time, the integrators would saturate if two separate PI controllers were used [86]. For this reason, a single PI controller is used for the roll/pitch and yaw controller. These vectors are represented as θ_e and ψ_e for the roll/pitch and yaw error vectors, respectively. Eq. 25 shows the equations for the proportional and integral error terms [86]. In the proportional term, the two error vectors are added together and then multiplied by a scalar, K_p , the proportional gain. The integral term adds the roll/pitch and yaw and multiplies them by the time step, dt. This is then multiplied by the integral gain (k_i)), which is the error term for the current time step and adds this to the previous error. Finally, the adjustment vector is composed of the $\epsilon_p(t)$ and the $\epsilon_i(t)$ vectors, as expressed in Eq. 24.

4.4 Summary

This chapter described an attitude estimation scheme suitable for verifying the performance of the control electronics developed in this thesis. The attitude estimator was divided into three steps: (1) use gyro data to update the DCM, (2) orthonormalize the DCM, and (3) use the complementary filter to compensate for errors. The DCM updates every 20ms, as dictated by the sensors. Every time the DCM is updated it must be made orthogonal and normalized to satisfy the requirement of the DCM update equation. The orthonormalized DCM is then compared to the reference sensors by the complementary filter. The complementary filter then applies a compensations term to the DCM to remove errors generated by the gyro bias and drift. Over time the errors generated by the DCM decease to improve the accuracy of the estimate.

5 Brushless DC Motor Control Shield

The Brushless DC control shield is designed to connect to the BLDC control electronics to the main board. Fig. 33 is a block diagram of the BLDC control shield. The control shield signals originate at the CONTROL DSC, which is connected to the High/Low Drivers. The High/Low Driver are employed to translate the TTL level logic of the microcontroller to the high voltage signals necessary to operate the MOSFETs. The MOSFETs are used as a switch to supply power to the motor. The motor is commutated by the signals generated by the microcontroller. Built-in Hall Effect sensors sense the position of the rotor. These sensor signals are fed back into the microcontroller, thereby simplifying commutation. The hardware blocks in Fig. 33 have been divided into three categories representing the hardware block's location within the BLDC control architecture. The CONTROL DSC is located on the main board while the BLDC control hardware (High/Low Divers and FETs) is located on the BLDC shield. The hall sensors are embedded within the BLDC motor, itself. Each of the blocks in Fig. 33 will be described in more detail in the following sections.

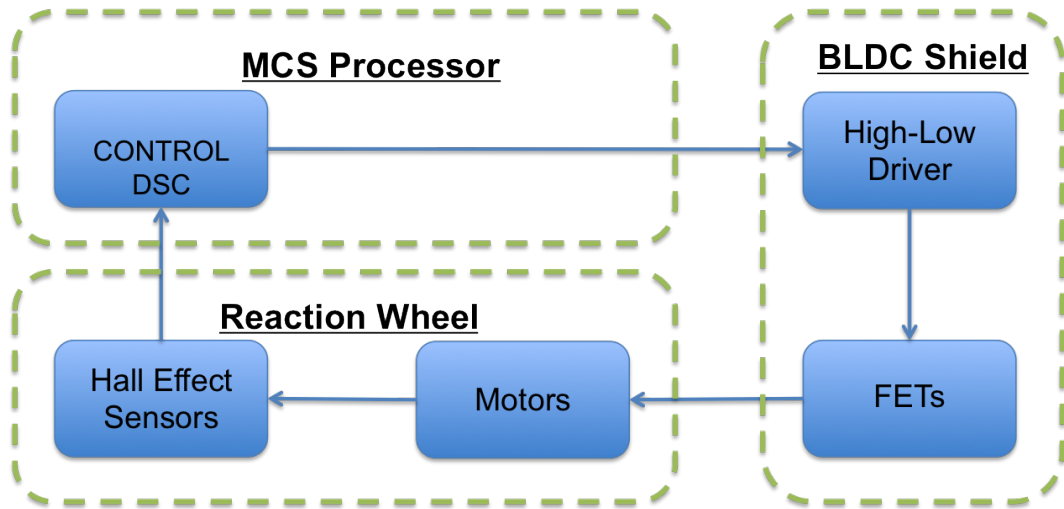


Figure 33: BLDC Control Shield Block Diagram, showing the flow of data in the BLDC control loop.

The main board is shown in Fig. 34 (red dashed lines) mounted on the developed control shield hardware. The components making up the reaction wheel control loop are indicated in Fig. 34 along with other necessary support electronics. The motor connector is an eight pin

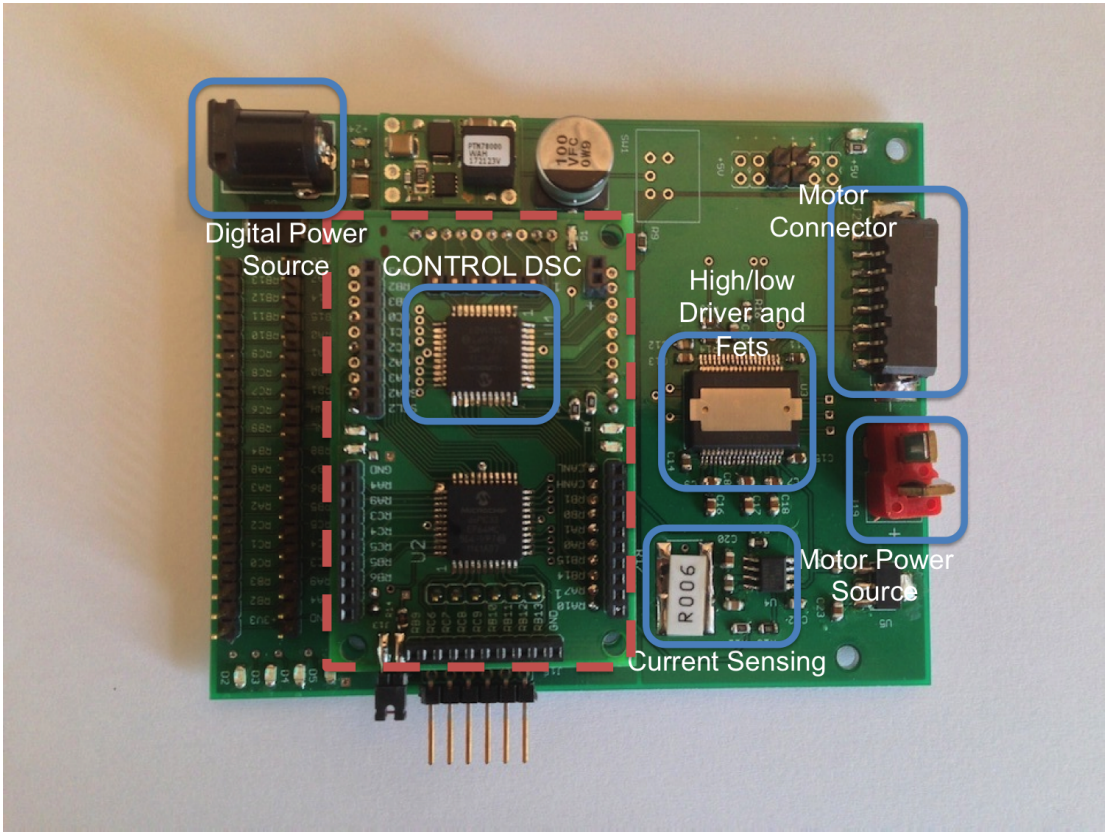


Figure 34: Photo of the BLDC Control Shield with the main board mounted.

connector used to transfer three motor control signals, three hall sensors signals, power and ground to the reaction wheel. Logic level shifting and power amplification is done within a signal chip, that converts the CONTROL DSC signals into +24V motor control signals. The CONTROL DSC is located on the main board, which uses pin headers to transfer data between the BLDC shield and the main board. The current sensing circuitry is used to measure the power consumption of the motor and separate power sources are used to power the motor and digital electronics. This was done to help isolate the noise generated by the BLDC motor.

5.0.1 MOSFETs

In order to apply the electrical power to each of the motor terminals MOSFETs are employed. When the MOSFET is operating in the triode region it behaves as a variable resistor that is controlled by a voltage input on the gate of the transistor [66]. In motor driving applications, MOSFETs are driven hard into the “fully enhanced” range, where they are simply

on (low impedance) or off (high impedance). However, the MOSFET can also be used as a digital switch if only ON or OFF signals are transmitted to the gate. MOSFETs come in two different types: N-channel and P-channel MOSFET. Both devices perform similar tasks except that the input of the P-channel is inverted and P-channel devices are typically slower than their N-channel counter-parts. A diagram of an N-channel MOSFET is shown in Fig. 35a. Fig. 35a depicts the Drain, D, and Source, S.

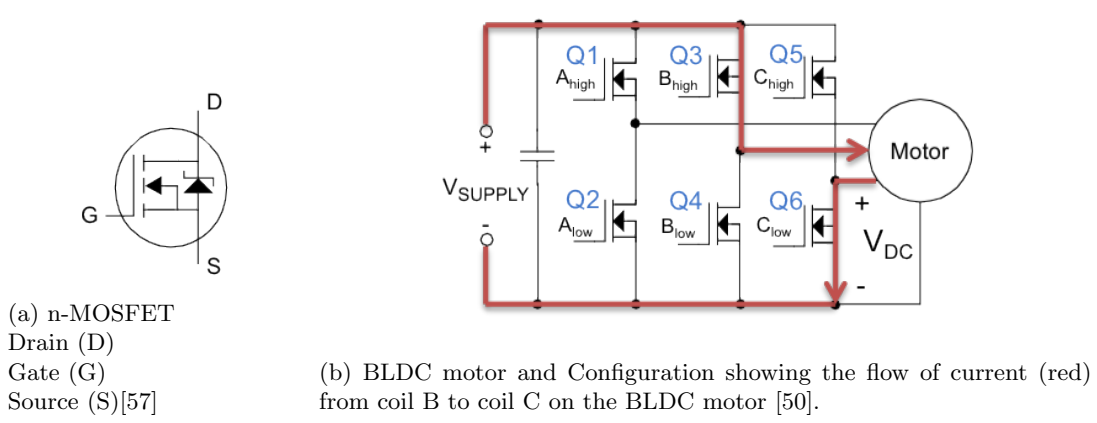


Figure 35: BLDC control with n-channel MOSFETs (a); showing how power is supplied to the motor using the high/low side MOSFETs (b)

MOSFETs can be used in a configuration similar to that of Fig. 35b in order to drive the BLDC motor. In this configuration, two MOSFETs are employed for each terminal of the motor, where the high side MOSFETs (Q1, Q3, Q5) connects the Drain (D) to the power supply and the Source (S) to the terminal of the motor. The low side MOSFETs (Q2, Q4, Q6) connects the Drain (D) to the terminal of the motor and the Source (S) to ground. If terminal B is meant to be powered, Q3 will be turned ON and Q4 turned OFF. Similarly, if terminal C is to be grounded, Q5 is turned OFF and Q6 is turned ON. In the case that the terminal A is disconnected, both Q1 and Q2 will be turned OFF, as depicted by the red arrow in Fig. 35b. Both Q1 and Q2 should never be activated at the same time, or a short circuit will be created, damaging the circuitry. Additional logic can be implemented to ensure that Q1 and Q2 are never activated at the same time.

5.0.2 High/Low Side Gate Drive

The BLDC control hardware requires six MOSFETs (three pairs), one pair for each motor coil. Each of these MOSFETs is controlled by the microcontroller. In the case of the control hardware, the dsPIC33E controls the MOSFET pairs. The control hardware requires $V_{supply} = +24V$, as dictated by the Maxon EC45Flat motor since the EC45Flat motor was used for preliminary testing. More specifics about the EC45Flat motor can be found in the Appendix.

A voltage of +24 volts is required to fully turn ON the High Side MOSFET. This large voltage is required because the MOSFET acts like a variable resistor, where the resistance decreases as the gate voltage increases towards the Drain voltage. If the gate voltage is not equal to the Drain voltage, a large resistance is seen between the Drain and Source which uses the available power to drive the motor. The microcontroller, however, operates on +3.3V or +5V, which is insufficient to turn ON the MOSFETs. For this reason, Gate Drivers are normally used to boost the microcontroller signal to a voltage capable of turning ON the High Side MOSFETs.

The Low Side MOSFETs have a similar problem, which is described using the example below. If the next commutation sequence requires current to flow from Terminal B to Terminal C. Current will flow from V_{supply} through the High Side MOSFET on Terminal B through the motor and out of terminal C. Fig. 35b depicts the MOSFETs associated with coils A, B, and C. The current flowing from Terminal B to C is also depicted by the RED arrow. In this scenario, current flows through the Low Side MOSFET on Terminal C, which creates a voltage on the Drain of the Low Side MOSFET. Therefore, in order to turn ON the Low Side MOSFET a Gate voltage that is greater than or equal to the Drain Voltage (depicted as V_{DC}) must be applied, otherwise the Low Side MOSFET will not completely turn ON. For the reason just stated, a Low Side Driver is also generally necessary to operate the MOSFETs.

The High Side Driver works by utilizing a bootstrap capacitor (C_{boot}), as seen in Fig. 36. The bootstrap capacitor is placed between the bias voltage and source of the high side MOSFET, pin VS. When the low side MOSFET (Q2) is turned ON and the high side MOSFET (Q1) is turned OFF, the voltage on pin VS is at ground potential, $VS = 0$. When this happens, the bootstrap capacitor begins to charge to the voltage, V_{bias} . Then, when the high side MOSFET (Q1) is turned ON and the low side MOSFET (Q2) is turned OFF, the voltage on pin VS begins to rise ($VS = V_{cc}$). As the voltage on pin VS rises to V_{cc} , the charge stored on C_{boot} stays

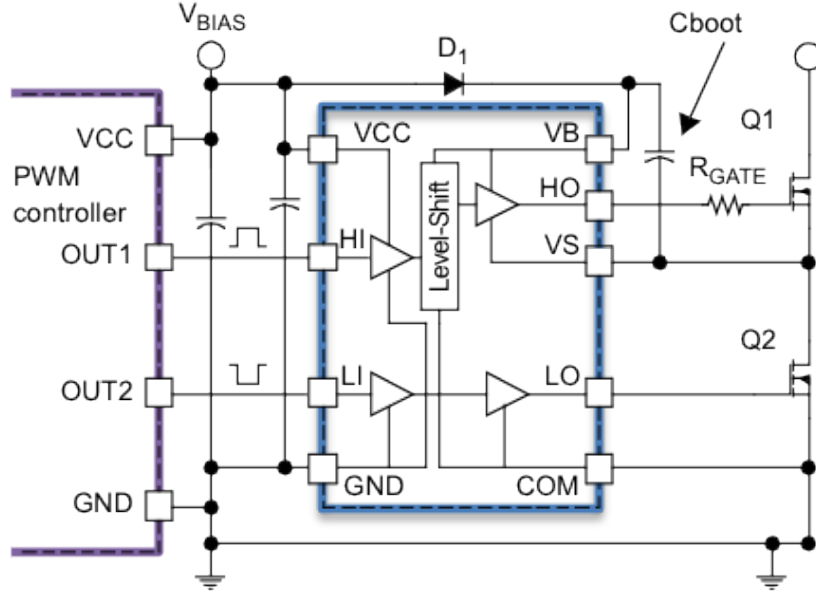


Figure 36: Diagram of microcontroller (purple), High/Low Side Driver (blue), and MOSFET-illustrating the bootstrap capacitor [57].

constant due to the presence of the diode (D1). Due to the fact the charge on C_{boot} is not able to discharge, voltage accumulates on pin VB, such that $VB = V_{C_{boot}} + VS$ (where $V_{C_{boot}} = V_{bias}$ and $VS = V_{cc}$). The voltage stored across the bootstrap capacitor is then used as an offset voltage. This is necessary because the voltage on pin VS is now equal to the power supply. In order to turn ON Q1 a larger voltage than V_{cc} must be applied to the gate, which is provided by the bootstrap capacitor. For example, if the $V_{bias} = 10V$ and Q1 is connected to a 12V power supply, when Q1 is turned ON $VS = 12V$. However, since the bootstrap capacitor has been charged with a 10V potential, meaning the voltage on VB ($VB = V_{C_{boot}} + VS$) is equal to 22V. The high side gate voltage is 22V which is sufficient to turn on Q1. All of the high side MOSFETs must be operated in the same way.

5.1 Current Sensing

In order to monitor the BLDC motor power consumption, or to operate the BLDC motor in current controlled mode a measure of the motor current must be measured too. There exist three popular techniques to measure the current: (1) Hall Effect sensors, (2) current-sensing transformers, and (3) a shunt resistor [75]. The shunt resistor method uses a very precise

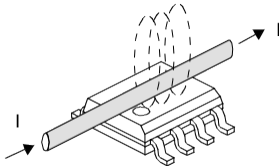


Figure 37: Hall Effect sensors measure the current flowing through a wire by observing the magnetic field generated by the flow of current as described by Ampere's Law [75].

resistor and the current flowing through it is measured indirectly by measuring the voltage across the resistor and applying Ohm's Law. The transformer method uses a transformer to transfer power to an isolated circuit where the current can be measured across a resistor. The Hall Effect sensor method measures the magnitude and direction of the magnetic field created by the current flowing through the wires or circuit board traces. Further analysis into the Hall Effect sensor and shunt resistor methods is done below. The transformer method was not explored because a larger form factor is required for its implementation.

5.1.1 Hall Effect Current Sensing

The Hall Effect current sensing method measures the induced voltage generated by the Hall Material embedded in the Hall Effect Sensor. The Hall Effect sensor is a device that utilizes the principle of the Hall Field that is created by a magnetic field. As current flows through the wire over the Hall Effect Sensor, a proportional magnetic field is created, (Ampere's Law). Fig. 37 depicts current flowing through a wire over a Hall Effect sensor. The flow of current generates a magnetic field as depicted by the dashed lines encircling the wire. This magnetic field generates an associated hall voltage, which is a function of the magnetic field strength.

The Hall Effect can be explained using the Lorentz Force which is defined as, $F_m = qv \times B$ [71], where F is the Lorentz Force, q is the charge of the electron, v is the velocity of the electron, and B is the magnetic field. This is depicted in Fig. 38, where constant current is applied across the Hall Material. The applied current creates a flow of electrons against the flow of current. In Fig. 38 current is flowing in a clockwise direction, so the electrons will flow in a counter-clockwise direction. Then, when a magnetic field (\mathbf{B}) is applied the Lorentz Force is created. The Lorentz Force is perpendicular to the velocity of the electrons (which are flowing in a counter-clockwise direction) and the magnetic field (which is going upwards through the Hall

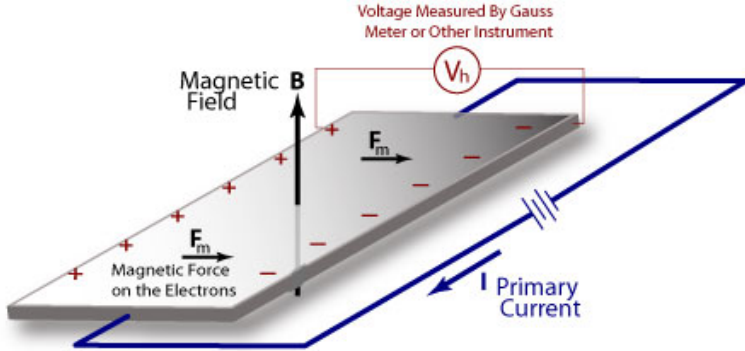


Figure 38: Hall effect sensor diagram showing how the introduction of a magnetic field (B) creates a differential voltage in the hall material [53].

Material). A Lorentz Force is created which forces the electrons to the right and the holes to the left of the Hall Material. A hole is defined as an absence of an electron and is associated with a positive charge [71]. Formation of the holes on the left side of the material and electrons on the right side creates a voltage differential, called the Hall voltage., which can be measured.

Hall Effect current sensors provide isolation between the motor and digital circuitry. This isolation can help to reduce the noise on the system and prevents unwanted errors. However, Hall Effect sensors were not implemented due to the potential for magnetic interference generated by reaction wheel the motors and magnetic torquers which are part of the attitude control system.

5.1.2 Shunt Resistor Current Sensing

The shunt resistor current measuring method was chosen because of its ease of implementation and overall accuracy. As compared to the Hall Effect approach high side and low side current sensing is done by measuring the voltage differential across a the shunt resistor (R_{SENSE}). The differential current can then be calculated using the equation $V_{SENSE} = I * R_{SENSE}$. This equation depicts that the larger the value of R_{SENSE} the more sensitive the output voltage is to a change in I . However, for larger values of R_{SENSE} , more power is dissipated, as shown by Eq. 26. Therefore, consideration needs to be taken when selecting the value of R_{SENSE} .

$$P = I^2 R_{SENSE} \quad (26)$$

A few different shunt resistor implementations exist, where the shunt resistor is positioned

either before the load (high side) or after the load (low side). Fig. 39 is a block diagram of the high and low side current measurement schemes. The two schemes each have their own disadvantages. The high side measurement circuit requires more expensive amplifiers. This is due to the fact that the input voltages to the amplifier are much larger. A disadvantage for the low side current sensor is that it affects the Back EMF. This is a potential issue if Back EMF sensing is being employed to perform commutation of the BLDC motor. In general, high side current sensing is preferred and it was used here.

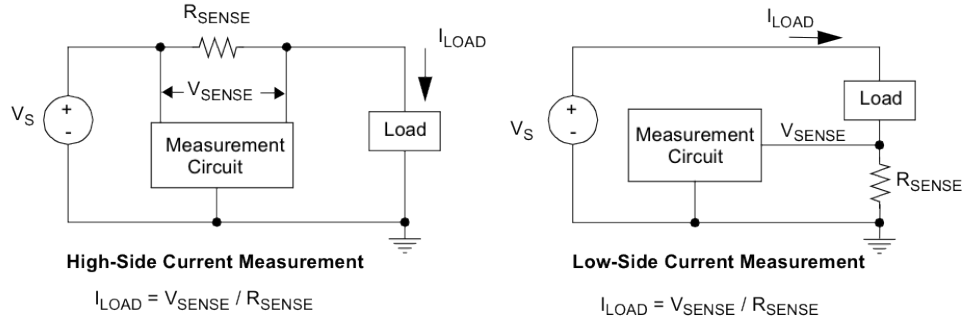


Figure 39: High and low side shunt resistor current sensing diagrams showing that the difference between the two methods is the location of the shunt resistor with respect to the load [75].

The resistance value (R_{SENSE}) must be extremely accurate. Any lack of precision in the resistance value will impact the precision of the current measurement. For this reason, a high precision resistor, of at least one percent tolerance is required.

5.1.3 High Side Current Sensing

High side current sensing as depicted in Fig. 40 shows the shunt resistor (R_{SENSE}) between the power supply and the load. In the case of the control hardware, the load is the Brushless DC motor. The high side current sensor utilizes a differential amplifier to measure the current. The differential voltage is measured across the R_{SENSE} resistor. The block diagram in Fig. 40 also shows that current in front of the R_{SENSE} resistor travels through the voltage divider connected to the positive input terminal. Therefore, the voltage on the positive input terminal of the OP-Amp is equal to $V_S \frac{R^*}{R_{IN} + R^*}$. On the other side of the R_{SENSE} resistor, a voltage is being input into the negative terminal of the differential amplifier. The negative input

voltage is defined in Eq. 27.

$$\begin{aligned}\frac{V_{load} - V_+}{R_{IN}} &= \frac{V_+ - V_{out}}{R^*} \\ V_{SENSE} &= V_s - V_{load} \\ V_{out} &= -V_{SENSE} \times \frac{R^*}{R_{IN}}\end{aligned}\tag{27}$$

The high side current sensing method measures the current through the load (I_{LOAD}) because the current flowing through the load is the same current flowing through the R_{SENSE} resistor. As described in Eq. 27, the current flowing through R_{SENSE} creates a voltage on the negative input terminal. As seen from Eq. 27, the voltage levels on the positive and negative input terminals can be extremely large. These large voltages require a high voltage OP-Amp with high sensitivity. A high level of sensitivity is necessary because the voltage differential between the positive and negative input terminals is extremely small.

The small input differential can be observed in Eq. 27. In Eq. 27, the output voltage is equal to V_{SENSE} times a specified gain ($\frac{R^*}{R_{IN}}$). As the gain is increased, the effects of noise on the signal increases as well. If the gain is too large the signal noise will adversely affect the output. The best way to increase sensitivity without increasing the effects of noise is to increase the value of R_{SENSE} . However, increasing the value of R_{SENSE} increases the power consumption of the current sensing circuitry. Therefore, a small value of R_{SENSE} must be chosen, usually around 1-10mΩ.

In order to convert the output voltage of the OP-Amp into a current reading, an Analog to Digital Converter (ADC) must be used. The ADC (on the CONTROL DSC) reads in the

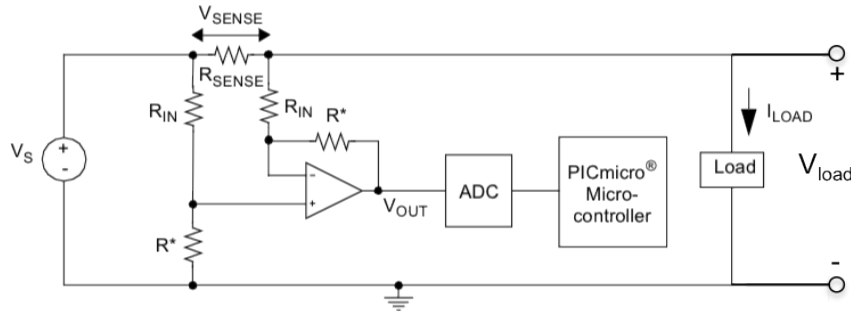


Figure 40: High side current sensing block diagram showing the high voltage measured at the inputs of the OP Amp [75].

analog output of the OP-Amp and converts it into a digital signal. Once the signal has been read, the output voltage must be converted to a current value. This is performed using Eq. 28, which takes the digital value from the ADC and converts it back into a current value using Ohm's Law.

$$I_{Load} = \frac{V_{out}}{R_{SENSE}} \frac{R_{in}}{R^*} \quad (28)$$

5.2 Noise and Isolation

5.2.1 Noise

A serious issue related to motor control is the electrical noise created by the motors. The noise created by the motor is called inductive kickback, which is generated by the windings of the motor. The electrical noise is generated during the switching phase, when the coils are switched from an active (high impedance) state to an inactive state and vice versa.

Inductive kickback can be described using a simple circuit, like the one in Fig. 41. Fig. 41 shows a power supply connected to an inductor that is being controlled by a switch. When the circuit is closed, the inductor starts to charge and a magnetic field is generated within the inductor. The magnetic field generated by the inductor is created by the voltage differential across the inductor, where the voltage drop across the inductor is equal to the battery voltage. When the switch is opened, the battery is no longer supplying the inductor. The inductor collapses its magnetic field in order to maintain the voltage differential across itself. This rush causes current to flow back towards the switch at a very high voltage. However, the inductor is not able to maintain this voltage for long, and generates a high voltage spike commonly seen as a spark when the switch is opened. This high voltage spike is inductive kickback. This can

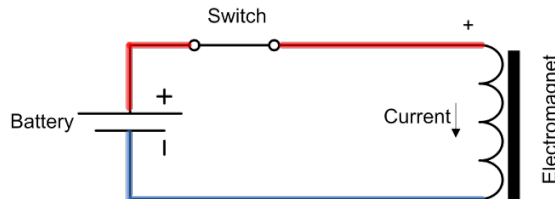


Figure 41: Simplified circuit exemplifying inductive kickback, when the switch is opened a large spike is generated by the inductor [30].

be observed mathematically by evaluating the inductor voltage equation, $V = L \frac{di}{dt}$. When the switch is opened the change in current, $\frac{di}{dt}$, is large due to the sudden stop in the supply current. Therefore, a large voltage spike can be observed.

The circuit used to describe the inductive kickback in Fig. 41 also applies to the Brushless DC motor. If three of the circuits found in Fig. 41 are placed in the Y configuration, a simple model of the BLDC motor is obtained. In this scenario, the switch can be thought of as a simplified model of the MOSFETs and gate drivers, whereas the coils within the motor can be modeled as inductors. Under this configuration, it is easy to imagine the large spike in voltage that will be created each time the power supply is switched. This will occur on every commutation transition. However, things are worse in practice since the motor control signals will be Pulse Width Modulated (PWM). This means that the power supply will be turned off and on very quickly during the on state of the coil. Therefore, inductive kickback will be observed at a very high frequency.

Inductive kickback for a PWM controlled motor can be seen in Fig. 42, where the ideal control signal is highlighted in red, blue, and green for Phase A, B, and C, respectively. Observing Fig. 42, it can be seen that the ideal signal is corrupted by the noise due to the inductive kickback.

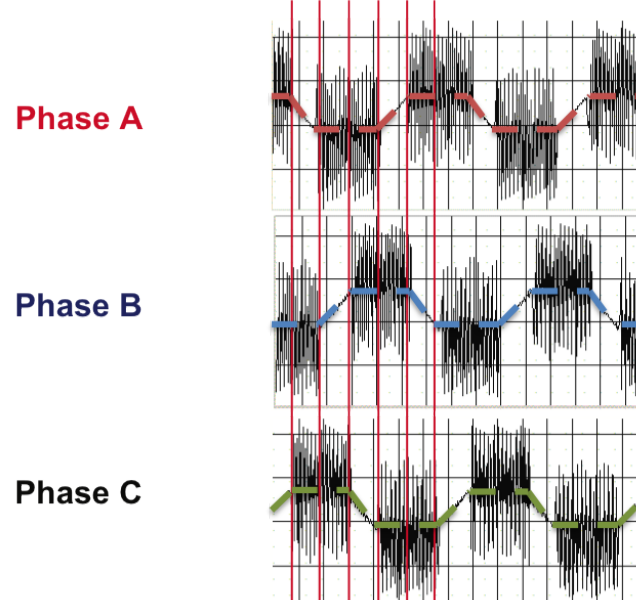


Figure 42: Example of inductive kickback, the inductive kickback creates the noise on the control signals [55].

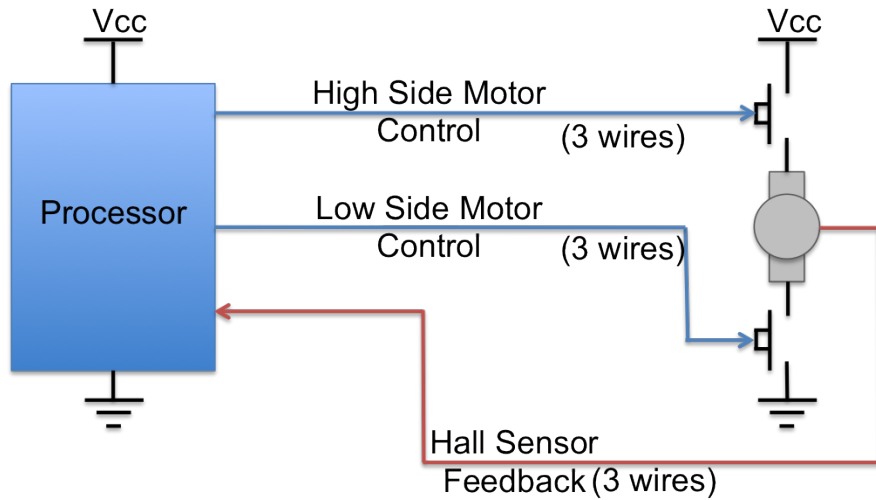


Figure 43: A simplified block diagram showing the connections between the microcontroller and the BLDC motor.

The inductive kickback noise present in Fig. 42 can disrupt other electronics by effecting the power supply and/or ground return signals. The electrical noise can alter the power signals by rapidly changing the amount of power required by the system. For instance every time the inductive kickback peaks, extra power is present in the system and every time the inductive kickback dips extra power must be supplied to the system. This means that the power supply needs to continuously alter the power output to match the system demands. However, the inductive kickback is generally too fast for the power supply to compensate and this generates fluctuations on the power supply signal.

5.2.2 Isolation

The noise seen in Fig. 42 is something that needs to be dealt with or else other components, such as the communication or processor data acquisition, could produce errors. In reference to the noise generated by the BLDC motors, the BLDC motor use the same ground reference as the processor. This means that ground noise produced by the BLDC motor can affect the processor. Fig. 43 depicts a simplified block diagram of the connections between the processor and the BLDC motor. In all, five types of connections exist between the motor and processor: power, ground, hall sensors, high, and low side motor control signals. The power signal can be ignored because power is being regulated for the processor, but the ground signal is unregulated.

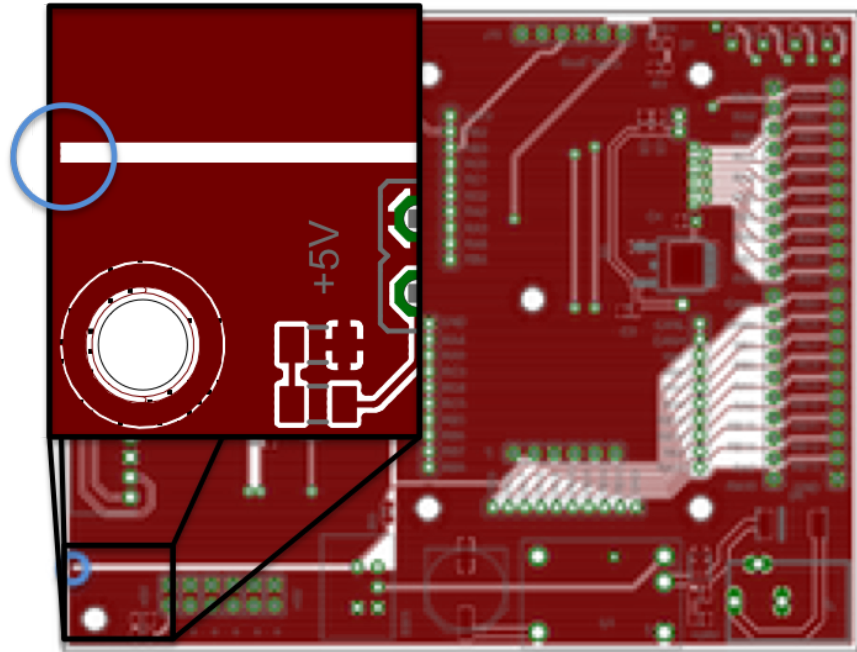


Figure 44: Eagle Layout of the top BLDC Shield, showing an enlarged view of the mecca ground, indicated by the blue circle.

The ground signal is common to both the processor and the motor, without which the three signal wires would be useless. In order to reduce the noise effects on the processor, the motor must be isolated from the processor. Optical isolation is one method of severing the connection between the processor and motor. Optical isolation was not implemented due to the fact that ten control signals are being used to communicate between the processor and motor, taking more space than is available. The complexity of the optical isolation circuitry is also increased due to the fact that the current sensing circuitry produces an analog output. This would require precise measurement of the current sensing output so that the optical isolator does not saturate.

Since, the control hardware uses a common ground reference for all its electronics, the ground references are “isolated” by using a small trace to connect the processor and motor ground planes, this is called a “mecca” ground. The small trace is seen in Fig. 44 and is indicated by the blue circle. The small trace allows for a common ground reference, but because of the small path between the two ground plane noise is “isolated”. This method does not completely isolate the noise, but does help to reduce it.



Figure 45: Image of the EC45 Flat Maxon Motor used on the hardware testbed. This motor was chosen due to the built in flywheel, making fabrication easier [38].

5.3 BLDC Motor Commutation

This section will cover the commutation algorithm required to properly rotate the BLDC motor. The BLDC motor employed in the testbed is the EC45 Flat by Maxon Motors (Fig. 45). The EC45 motor was used to overcome the limitations of the testbed, like the static friction of the ball bearing. This motor is too large for implementation in the actual CubeSat design, but were chosen because of its built in momentum wheel. Limited fabrication tools and material restricted development of the AECS momentum wheel. Once the system has been checked out, the Faulhaber 1509 motor and flywheel designed in Section 3: Hardware can be used.

In order to operate the BLDC motor, the proper commutation sequence needs to applied, otherwise the rotor will not turn. Block commutation was chosen over sinusoidal and field oriented control (FOC) due to the limited algorithm complexity and required hardware [74]. Both the sinusoidal and FOC methods require additional hardware to more accurately measure the rotor position. The commutation states can be measured with Hall Effect sensors or a measurement of the Back EMF voltage. Hall Effect sensor commutation requires the use of three sensors to create six different states; the Hall Effect sensor output states are defined in Table 5. The logic states are defined in such a way that if Sensor C is taken as the most significant bit and Sensor A is the least significant bit, the Hall states can be represented by a binary number (for example: State 3 = 0b011). Using Table 5, the correct commutation sequence can be obtained for clockwise commutation. Table 5 depicts the next commutation sequence given the current readings from the Hall Effect sensors.

For counter-clockwise rotation the high and low signals are swapped. The lower portion of the table depicts the outputs of the three MOSFET pairs used to supply power or ground signals to the inner coils of the motor. When the high signal is a logic “1” the MOSFET pair

is activated and the high side MOSFET is closed, while the low side is open (State 1 MOSFET A is connected to power). The converse applies when the low signal is a logic “1” (State 1 MOSFET C is connected to ground). When both the high and low signals are logic “0” the MOSFET is placed in a high impedance state and both the high and low MOSFETs are open (State 1 MOSFET B is in a high impedance state).

5.3.1 DRV8332 Specific Motor Control

The primary components for the motor drive circuitry are the High/Low Side Drivers and the MOSFETs. The MOSFETs need to be chosen in order to work under all operating conditions including motor startup. The MOSFETs must be large enough to source and sink the starting current of the motors. Other than the starting current, the motor requires significantly less current. For example a nominal current of 2.32A is required for the EC45Flat motor. While the start up current can be as high as 23.3A. It is extremely important to select appropriately sized MOSFETs because BLDC motors require six MOSFETs, three pairs of MOSFETs, one for each coil. If the MOSFETs are significantly large, they will occupy additional space in the CubeSat. Therefore, the size and power of the MOSFETs needs to be carefully accounted for when selecting the correct device.

The control hardware uses the DRV8332 PWM motor control chip, which incorporates both the High/Low Side Drivers and the MOSFETs. With all the circuitry built into a single chip, a significant amount of space can be saved when laying out the BLDC motor drive circuitry.

	State 1	State 3	State 2	State 6	State 4	State 5
Sensor A	1	1	0	0	0	1
Sensor B	0	1	1	1	0	0
Sensor C	0	0	0	1	1	1
C_High	0	0	0	1	1	0
C_Low	1	1	0	0	0	0
B_High	0	1	1	0	0	0
B_Low	0	0	0	0	1	1
A_High	1	0	0	0	0	1
A_Low	0	0	1	1	0	0

Table 5: Clockwise Brushless DC Motor Commutation (high and low signals are reversed for counter-clockwise operation)

The DRV8332 is capable of supplying a continuous 8A and 13A peak. The DRV8332 is therefore sufficient to control the EC45 Flat motor. The DRV8332 can be seen in Fig. 34 and occupies a 14 x 16mm area. For reference, a single high power MOSFET with a TO252 package occupies a 11 x 7mm area [56].

The DRV8332's control signals are different from the standard MOSFET control signals. The microcontroller only needs to provide three PWM signals, but three digital reset signals, are also necessary. This is in contrast to the architecture of Fig. 43, which requires six PWM signals. The three PWM signals are used to control the three MOSFET pairs while the reset signals are used to reactive each MOSFET pair by placing them into a high impedance state.

Commutation of the BLDC motor was first simulated to verify the correct commutation sequence. Simulated Hall Effect sensor signals were generated to mimic the actual hall inputs (in Fig. 46), the associated PWM and Reset signals were output using the CONTROL DSC, as depicted in Fig. 47. The first Block (S2) in Fig. 47, shows PWM_B and the Reset_A as active. This means that terminal B of the motor is connected to power while terminal C is connected to ground. This leaves terminal A in a high impedance state. Fig. 47 is a measurement taken from the control hardware board using of a Saleae Logic Analyzer [15]. Through this hardware in the loop demonstration it was shown that the correct BLDC motor commutation was being performed and the developed firmware could later be used to control the reaction wheel.



Figure 46: Simulated hall effect sensor signals produced by the control hardware, these signals were used to simulate the motor spinning and verify proper commutation of the motor's control signals.

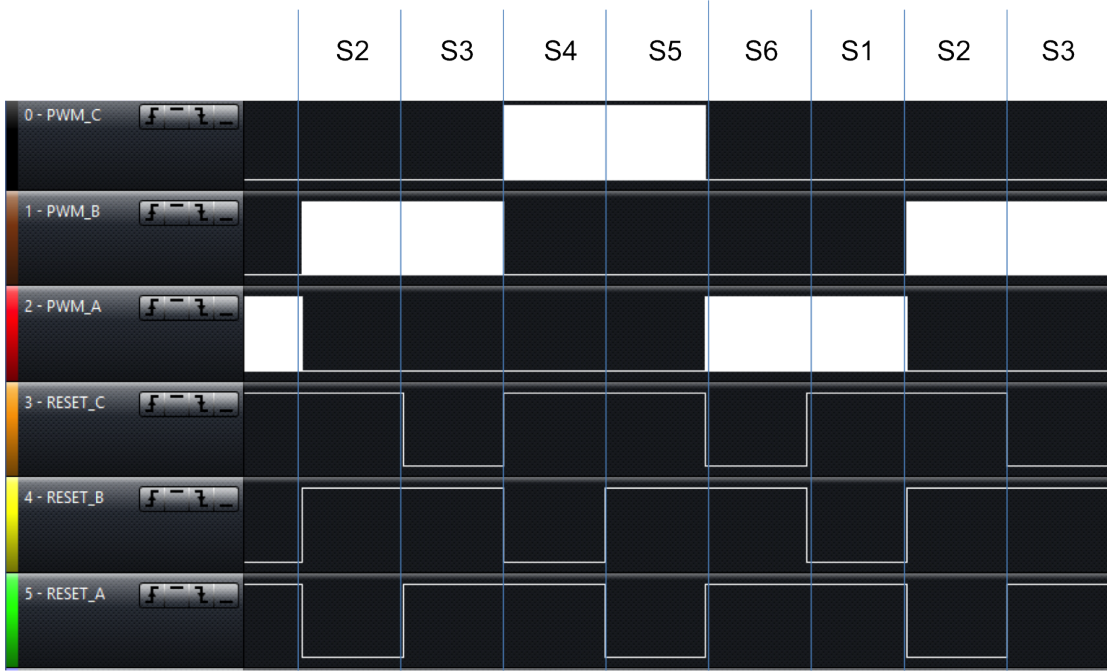


Figure 47: PWM and reset signals using simulated hall sensor signals (Fig. 46).

5.3.2 Reading the Hall Sensors

The Hall Effect sensors produce a pattern similar to that of Fig. 46. This signal pattern must be interpreted by the microcontroller to measure the position and speed of the rotor. The position of the rotor has been described earlier and is done using Table 6. The speed is determined using the Input Capture module on the dsPIC microcontroller. The Hall Effect sensor signals are input into the Input Capture (IC) Module, where a timer is activated every time a rising or falling edge is detected. By measuring the T_{ON} time of each Hall Effect sensor signal, the motor speed can be estimated.

For the EC45 motor employed on the testbed one complete rotation of the motor consists of eight electrical revolutions. An example of a complete electrical revolution can be seen in Fig. 18, which shows a single pole BLDC motor. An electrical revolution consist of six Hall Effect sensor states rotating from S1 to S5 ($S1 \rightarrow S3 \rightarrow S2 \rightarrow S6 \rightarrow S4 \rightarrow S5$) as seen in Fig. 46. A full rotation of the EC45 motor occurs every eight electrical revolutions because the EC45 motor is an eight pole Brushless DC motor [84]. The poles of the motor represent the number of magnetic poles located on the rotor [82]. Therefore, to calculate the time per rotation, the T_{ON} of the Hall Effect sensor reading must be multiplied by eight. Taking the inverse of this value gives the

	State 1	State 3	State 2	State 6	State 4	State 5
Sensor C	0	0	0	1	1	1
Sensor B	0	1	1	1	0	0
Sensor A	1	1	0	0	0	1
PWM_C	0	0	0	1	1	0
PWM_B	0	1	1	0	0	0
PWM_A	1	0	0	0	0	1
<i>RESET_C</i>	1	1	0	1	1	0
<i>RESET_B</i>	0	1	1	0	1	1
<i>RESET_A</i>	1	0	1	1	0	1

Table 6: Clockwise Brushless DC Motor Commutation using DRV8332.

number of rotation per second. Eq. 29 shows the calculation used to determine the Rotations Per Minute (RPM) of the motor. Where the time per rotation is defined as TPR and Rotations Per Second is defined as RPS.

$$TPR = T_{ON} * 8$$

$$RPS = \frac{1}{tpr} \quad (29)$$

$$RPM = rps * 60$$

$$= \frac{1}{T_{ON} * 8} * 60$$

The theoretical limit for the Maxon EC45 Flat motor is 6710RPM. This means that at maximum speed, the shortest T_{ON} time is about 1ms. In order to accurately measure the time per rotation, a timer precision of at least 0.1ms would be necessary. Using a 16 bit timer gives a measurable range of 0.1ms to 6.5s with a measurement accuracy of 0.1ms. Any rotation slower than 104s will not be registered by the IC module and be incorrectly categorized as not moving².

5.3.3 Speed Control

In order to control the torque generated by the reaction wheels, the current of the motor must be controlled. This can be done indirectly by controlling the speed of the motor. Speed control of an electric motor is accomplished by applying a greater or lesser voltage across the motor windings. The increase in the magnetic field causes an acceleration and torque. However,

²104s is the time per rotation associated with a 6.5s T_{ON} time

microcontrollers are not able to generate a voltage varying output signal, but they are capable of producing a rapidly changing binary signal, called a Pulse Width Modulated (PWM) signal. The PWM signal is a high frequency signal with a set period and a varying logic high time.

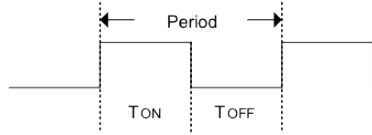


Figure 48: Sample Pulse Width Modulation (PWM) signal [8].

The varying logic high and logic low time are represented in Fig. 48 as T_{ON} and T_{OFF} , respectively. The period of the PWM signal is defined as a complete cycle from a rising/falling edge to the next rising/falling edge. The period and the duty cycle are used to describe the PWM signal, where the duty cycle is defined as the percentage of time of T_{ON} as compared to the period. The duty cycle can be used to control the output voltage, which is done by averaging the PWM signal over time. For example, if a fifty percent duty cycle is being applied to a +5V signal, then the output voltage will be equivalent to a +2.5V signal.

Averaging the PWM signal is done using a low pass filter. Due to the fact the PWM signal is a square wave, it is composed of the odd frequency harmonic and a DC term, as expressed in Eq. 30. In Eq. 30 the d_o term describes the DC offset and V represents the amplitude of the square wave. By applying a low pass filter with a cutoff frequency less than $\sin(k\omega_o t)$, all of the odd harmonics can be removed such that the square wave equation becomes, $x_{sq}(t) = d_o$. This DC term is the average voltage dictated by the PWM duty cycle. In practice, the coils of the BLDC motor act like a low pass filter, when driven by the PWM signal, so the pulse width can be used to control the average voltage across the motor windings.

$$x_{sq}(t) = d_o + \sum_{k=1}^{\infty} \frac{4V}{k\pi} \sin(k\omega_o t) \quad (30)$$

The timing diagram in Fig. 49 shows the Hall Effect sensor readings and the appropriate PWM signals. The PWM signals on the left side of the RED line are a result of a hundred percent duty cycle signal. On the right side, a seventy-five percent duty cycle is applied and therefore, the BLDC motor will be at seventy-five percent of its maximum speed. Control of the reaction wheel speed is demonstrated in Fig. 50, which shows the open loop response to a step

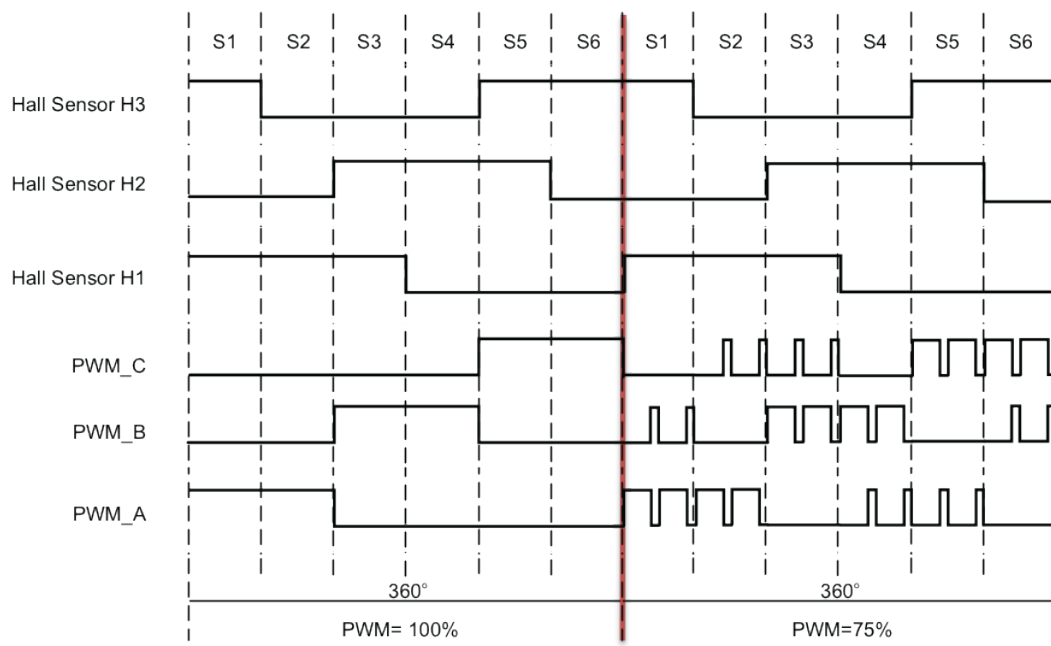


Figure 49: Timing diagram showing hall sensors output and PWM signals [24].

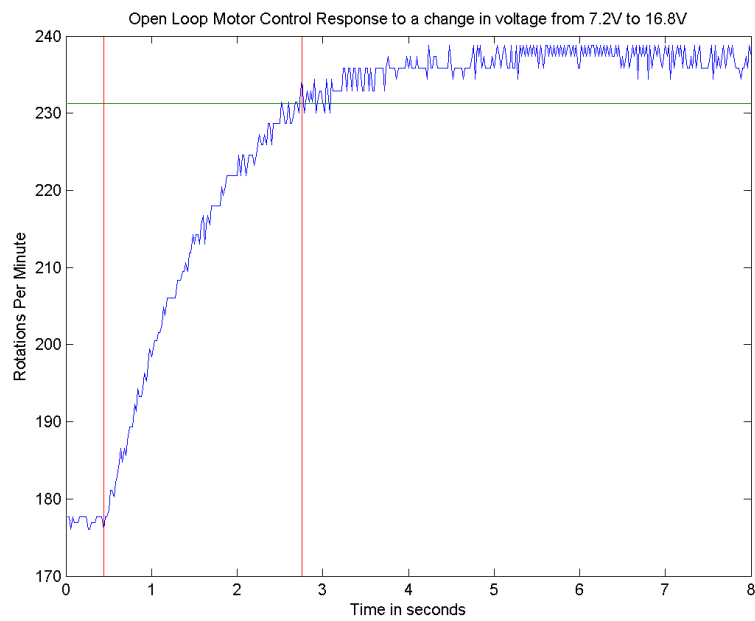


Figure 50: Open loop reaction wheel speed response for a 9.6V step input.

input into the BLDC motor. The motor was initially sped up to 177RPM @ 7.2V for 10s so that a steady state value could be reached. After 10s the input voltage was increased to 16.8V by changing the pulse width, in order to evaluate the step response of the reaction wheel.

The motor speed reached 235RPM within 2.32s. Since motor speed can also be estimated, the loop can be closed. This will be demonstrated in Section 6: System Checkout & Evaluation.

5.4 Summary

Open loop speed control of the BLDC motor was demonstrated using Block Commutation and the control shield. The control shield used a single motor driving chip (DRV8332) to commutate the motor. This chip was chosen to reduce the number of components on the control. The control shield also provided onboard regulation and a mecca ground to isolate noise generated by the motors. Application of the control shield was successful in controlling the EC45Flat motor, the reaction wheel control results can be found in Section 6: Evaluation Section.

6 System Checkout & Evaluation

As mentioned in the Introduction, the success of the hardware developed in this thesis is measured by three criteria: power consumption, volume, and attitude control accuracy (as specified in Section 1.2.1: System Requirements). Each of the design criteria will be further evaluated in this section. The specific system evaluation criteria are repeated below in Table 7.

Design Criteria	Requirement
Power Consumption	< 4.9 Watts
Hardware Volume	$\leq 1.5U$
Control Accuracy	$\leq 1^\circ$

Table 7: Summary of the Attitude Control System Criteria

6.1 Power Requirements

As previously described, a CubeSat Attitude Control System (ACS) should use less than 4.9W, otherwise there may not be enough power left over to operate the payload. The electrical power budget has been allocated into two parts: (1) control electronics and (2) motors. Table 8 shows that the Faulhaber 1509 Brushless DC motors consume most of the available power.

Table 8 also demonstrates that the power consumption of the electronics is less than the motors. The system processors (dsPIC33E) use 20mW each while operating at 20 Million Instructions Per Second (MIPS), but if more processing power is necessary, the processor can be operated at 70MIPS at the cost of an extra 82.5mW.

The measured power consumption for the control electronics also includes the accelerometer, which will only be used during ground testing. Therefore, the accelerometer needs to be replaced by a space sensor; Table 9 lists the power consumption of an accelerometer and Sun, star, and Earth trackers. In order to estimate the power consumption of the control hardware, the power consumption of the appropriate space sensor must be added. Different sensors are

Table 8: Power Consumption Table

Device	Supply	Current	Power	Total Power
Flight Electronics	15V	0.06A	0.9W	0.9W
Motors	12V	0.1A	1.2W	3.6W
Sensors	5 -12V	0.0075 - 0.044A	0.036-0.36W	0.036-0.36W

Table 9: Space Sensors Power Consumption Table

Device	Sensor Type	Supply	Current	Power
Accelerometer [3]	acceleration	3.3V	$140\mu\text{A}$	0.046mW
CubeSat Sun Sensor [7]	Sun	5V	10mA	50mW
ST-200 [92]	star	5V	44mA	220mW
Static Earth Sensor [7]	Earth	5V	360mA	360mW

useful for different applications and orbits. For instance, the orbit of the CubeSat could obscure the Sun or stars. However, assuming deployment in LEO, the Earth is always visible. The Earth sensor will be used for the power estimate, however this increases the power consumption of the AECS to 4.9W.

The power consumption for the complete system has been estimated at 4.9W, assuming that all three Faulhaber BLDC motors are operational (as seen in Table 8). This does not allow for a surplus of power if the Clyde Space solar panel system is not implemented. It is assumed that the system payload will require its own power to operate. It is also important to note that the payload may not be operating at all times; therefore, the excess power harvested from the solar panels can be used to operate the payload after sufficient energy has been stored. However, if the Clyde Space solar panels system is implemented, an excess of 15W will still be available to the system.

In comparison with other systems, the developed attitude control hardware uses the same amount of power as the Colony I Bus Platform. It has been estimated that the Colony I Bus uses 4.5W with the power consumption of the ADACS, Flight Control Processor, Flight Motherboard, and MAI-201 hardware taken into account [88] [6] [40].

6.2 Volume

If the control hardware is to be utilized within a 3U CubeSat, it must occupy less than half of the available space within the 3U CubeSat (ideally $\leq 1\text{U}$). This can be accomplished by carefully packaging the actuators within the CubeSat form factor, thereby, allowing for more space for the electronics. The final design, as seen in Fig. 51 and 52, is based on designs found in Section 3.1: Hardware Design Objectives.

Fig. 51 is a three dimensional view of the control hardware with the AECS hardware located within an isolated container where all the electronics can be stored. This container has

a volume of 210cm^3 , while the AECS control hardware with two peripheral shields occupies only 50cm^3 . The AECS control hardware can be seen as the green boards located at the bottom of the isolated container. The isolated container leaves ample room for more electronics or battery storage, as dictated by the mission's specifications. The design presented in Fig. 51 and 52 are specifically designed to fit within the Pumpkin CubeSat skeleton housing [6]. This allows the developer to easily deploy the control hardware and cater to specific mission objectives. The control hardware housing was limited to a $9.6 \times 9.6 \times 9.6$ cm size constraint allowing it to conform to the $10 \times 10 \times 10$ cm 1U CubeSat design criteria [68].

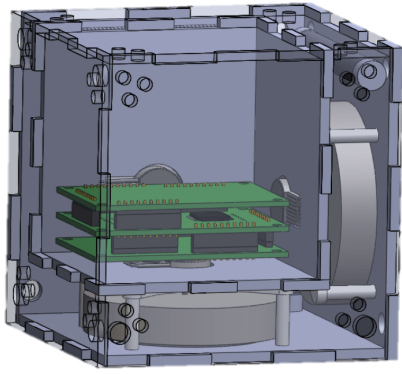


Figure 51: Model of control hardware layout with reaction wheels and magnetic torquers, showing that ample space remains for the control hardware.

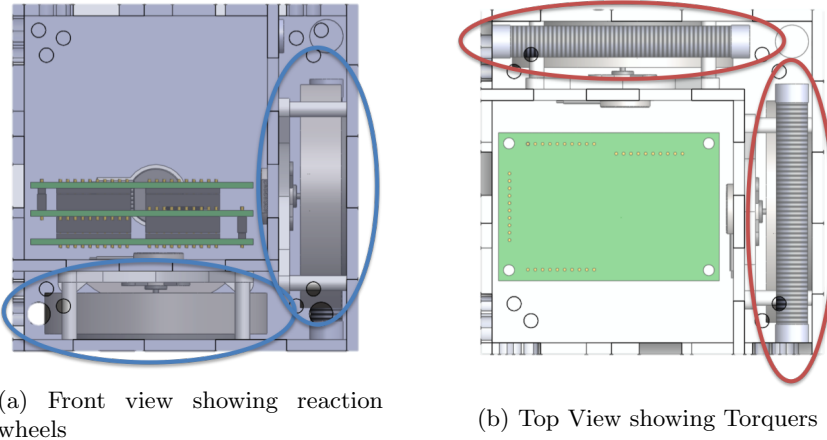


Figure 52: Different views of hardware depicting the flight control actuators (reaction wheels in Blue and Torquers in red).

The control hardware housing utilizes three reaction wheels as described in 3.1.2: Hard-

ware Section. The reaction wheels are depicted in Fig. 52a by the blue circles. The front view shows z and y-axis reaction wheels on the bottom and right side of the figure respectively. The x-axis reaction wheel is on the back wall of the model, however, view of the reaction wheel is obscured by the isolated electronics container. This design is also able to house three torque rods. The torque rods can be seen in Fig. 52b on the top and right sides of the figure as indicated by the red circles. The two depicted torquer rods are models of the “CubeSat Magnetorquer Rod” [7]. In order to control three wheels and three torques in addition to space sensors, 3 main board/shield stacks will be required. There call all fit within he available volume leaving 60cm³ of available space in the 1U form factor.

6.3 Control Accuracy

The control accuracy has been evaluated based on the accuracy of the attitude estimator and how closely the testbed can track the desired angle. The attitude estimation accuracy was measured to provide the theoretical limit of the control hardware because the demonstrated orientation accuracy is limited by the constraints of the testbed.

Due to the limited resources available, a high quality testbed like an air bearing was unavailable. This lead to the fabrication of the testbed found in Fig. 53, which was constructed from a foam core material used to reduce the mass and moment of inertia of the testbed. The testbed was designed to limit the maneuverability to the yaw axis. This was accomplished by



Figure 53: Photo of the testbed used to demonstrate yaw control; showing the reaction wheel is mounted directly above the rotating axis to maximize the transfer of angular momentum.

mounting the testbed to a single hard drive bearing, thereby limiting the rotation of the testbed to the z-axis.

Mounted directly above the hard drive bearing is the reaction wheel. By placing the reaction wheel directly on the rotating axis, the transfer of angular momentum between the reaction wheel and testbed can be maximized. Lastly, mounted directly above the reaction wheel is the control hardware. The control hardware was centered about the rotating axis to increase the stability of the testbed.

Due to the orientation of the hard drive bearing, roll and pitch maneuvers are impossible, but yaw maneuvers are unrestricted. Even with the limited mobility of the platform, it can be demonstrated that the control electronics can be used to accurately control the BLDC motor and manipulate the orientation of the testbed. Demonstrating successful yaw control, implies that control of the roll and pitch axes could be done in a similar manner.

6.3.1 Attitude Estimation Accuracy

As stated previously, in order to validate the use of reaction wheels as compared to other CubeSat actuators, a precision of at least 1° is necessary. From the table in Fig. 1, it was shown that the theoretical accuracy of reaction wheels is between $0.001 - 1^\circ$. An accuracy worse than 1° would weaken the argument for reaction wheels, since magnetic torquers can reach a theoretical accuracy of $1\text{-}2^\circ$. However, the redeeming quality of the reaction wheels are their increased maneuver speed and torque.

The dynamic yaw tracking error is expressed in Fig. 54, which shows the estimated yaw signal in blue and the actual yaw signal (measured from the magnetometer) in the red dashed lines. Three phases of the tracking error are depicted in Fig. 54. Phase A, the light blue region, demonstrates an approximate 2.5° tracking error, while the control hardware is being shaken. Phase B, the light green region, shows the estimated yaw tracking the magnetometer readings during an approximate $30^\circ/s$ clockwise rotation, which is a rate much faster than the CubeSat could command. Phase C, the light purple region, shows the control hardware held at a constant yaw angle. During Phases B and C the yaw error is almost reduced to zero. Significant error is only observed during shaking of the control hardware.

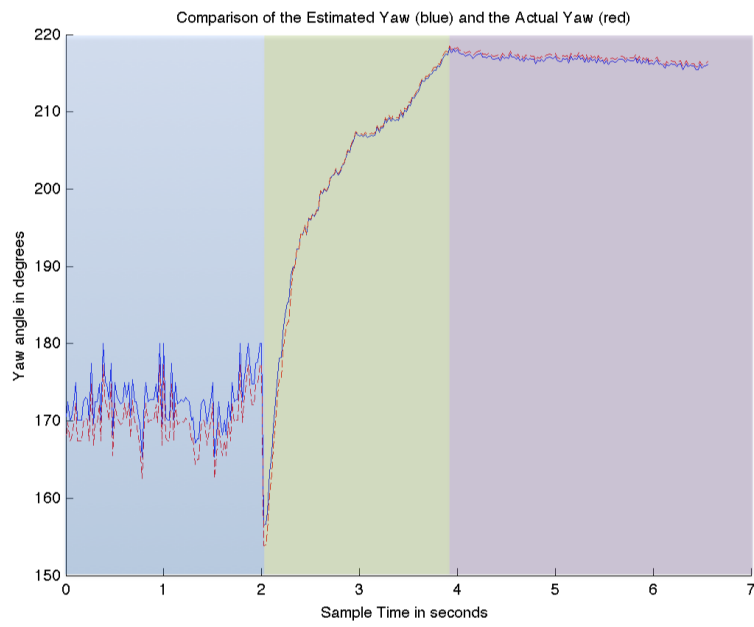


Figure 54: Depiction of the estimated yaw angle in blue and the actual yaw angle in red.



Figure 55: Depiction of the estimated yaw angle error corresponding to Fig. 54.

The error measurement between the actual yaw and estimated yaw angles can be found in Fig. 55. This shows that when the control hardware is being shaken a 2.7° yaw error can be observed. However during slow rotation the tracking error is reduced. A steady state error of approximately 0.4° can be observed in the purple region. Fig. 54 and 55 show the static and dynamic error is below 0.5° under normal operating conditions.

The Phase A response in Fig. 54 was done to represent disturbances caused by motor vibrations on the testbed. Comparison of Phase A in Fig. 54 and the steady state yaw response in Fig. 58 shows that the motor creates disturbances in the yaw measurement similar to shaking in Phase A of Fig. 54. To keep the control hardware from reacting to motor vibrations a 4° deadband was added. This means limitations of the testbed degrade the attitude control accuracy, but a theoretical accuracy of greater than 1.0° is possible with a improved testbed. This assumes the space sensors used on the CubeSat have an accuracy of 0.5° or better. The Earth sensor used for power evaluation has an accuracy of 0.5° [7].

6.3.2 Experimental Controller Design

The control algorithm implemented on the control hardware has taken several forms, however the general control algorithm for yaw control can be found in Fig. 56. In the case of the yaw controller, the input $\mathbf{U}(s)$ is the desired angle. Once the desired angle has been specified, it is sent into a summation block. This summation block is used to compare the desired angle and the measured yaw angle. The measured yaw angle is obtained from the Direction Cosine Matrix (DCM) which is evaluated on the SENSOR DSC (see Section 4). The roll, pitch, and yaw angles are extracted from the DCM and sent via I²C communication the SENSOR DSC to the CONTROL DSC. All motor control and attitude control algorithms are implemented on the CONTROL DSC. In the case of the yaw controller, the yaw angle is obtained and subtracted from the input angle. This generates an error or difference between the desired angle and the actual orientation of the system.

The error is then sent into the feedback controller, $\mathbf{k}(s)$. The controller generates a control signal which compensates for the error in the system. An offset signal is then coded to the output and used to apply a bias momentum in the system. The bias momentum is necessary because at low speeds the motor is affected by Torque Ripple associated with the Block Commutation control scheme [74]. Torque Ripple is a “periodic increase and decrease in the output torque”

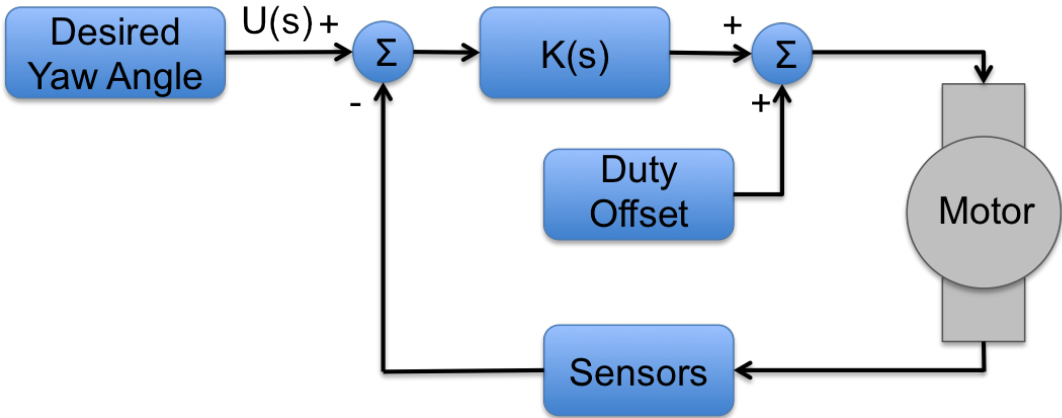


Figure 56: Block diagram of the implemented yaw controller showing the feedback control loop implemented on the control hardware.

generated by the motor [20]. A bias input of 6.6V was applied to the system to spin the motor at 2000RPM.

In designing and evaluating the control system, limitations have been placed on the control variables (testbed rotation rate, motor speed, and current consumption). Each of these control variable are limited to insure proper operation of the control hardware.

It was mentioned earlier that the speed of the motor cannot be too slow or else a speed measurement cannot be taken. The slowest measurable speed is 0.6RPM, therefore any rotations slower than this will not be measured. On the other extreme, the motor is physically limited to speeds less than 6710RPM. The motor current consumption is limited by the motor as well as the motor drivers. The drivers are limited to 8A [24], which restricts the amount of current that can be supplied to the motor.

Stabilization and correction of the yaw angle was accomplished using the three state variables of the prototype platform: testbed yaw angle (ψ_{sat}), motor current consumption (i) and, motor speed (ω_{mw}). It was discovered that the control gains needed to be set low in order to stabilize the system. When the gains were set too high, the testbed and reaction wheel would spin out of control. The empirically selected control gains are listed in Eq. 31. The first term

corresponds to the yaw angle control gain followed by the current and motor speed control gains.

$$\begin{aligned}
 k_\psi &= 0.0002859 \\
 k_i &= 0.0001716 \\
 k_\omega &= 0.0001216
 \end{aligned} \tag{31}$$

6.3.3 Experimental Control Response

In evaluating the performance of the control hardware, the system states have been measured and evaluated. Fig. 58 - 60 show the system state measurements for the testbed control response tests. These figures represent the testbed's orientation, motor angular velocity, and the motor current, respectively. Demonstration of the yaw controller can be broken into three steps. Step A is a 2° disturbance input in the clockwise direction. This is represented in Fig. 57a, which depicts the testbed as the hexagonal object and the disturbance input in green. Step A is represented in Fig. 58 - 61 as the blue region. This input is too small to register a control response because the accumulated error was too small to overcome the static friction of the ball bearing. Therefore, a second input was applied to the testbed in the counter-clockwise direction. This input, referred to as Step B in Fig. 57b, was a 14° input represented by the green region in Fig. 58 - 61. Step C is the system response to the 14° disturbance as represented using Fig. 57c as the double-sided arrow. The regulating response is represented as the purple region in Fig. 58 - 61.

The yaw orientation shown in Fig. 58 depicts a starting orientation of -38° and application of the Step A input in the blue region. This is immediately followed by application of a 14° counter-clockwise input shown in the green region. Application of the input lasts for about

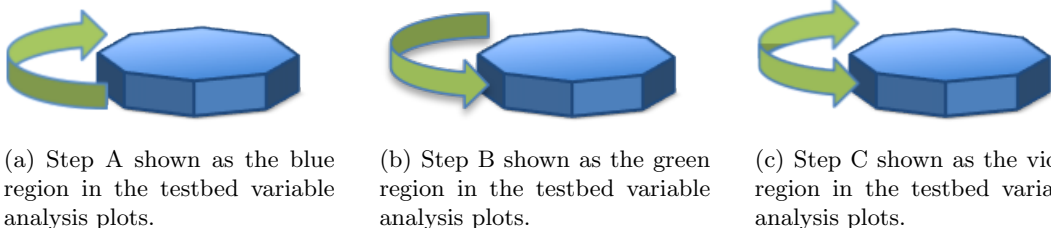


Figure 57: Diagram showing the three steps in the testbed variable analysis. Where step A is a 2° disturbance input in the clockwise direction, step B is a 14° disturbance input in the counter-clockwise direction, and step C is the regulating response to the disturbance inputs.

1s before the control error accumulates enough to affect the yaw angle. Implementation of a 4° deadband (to prevent friction induced limiting) means that the system controller is not activated until the yaw angle reads greater than -36° or less than -40° . The yaw response shows the controller corrects the yaw angle and settles around -36° , placing the yaw angle just on the edge of the deadband. Evidence of the controller trying to correct for small jitters in yaw can be found in the motor speed and control signal plots (see Fig. 59-60).

The testbed's angular velocity (Fig. 59) shows the reaction wheel speeding up for the first 0.5s, which corresponds to the change in the oriental from -38° to -40° within the first 0.5s as depicted in the yaw plot (Fig. 58). The slowing down of the reaction wheel from $t = 0.5 - 2$ s corresponds to the change in direction as seen in Fig. 58 at $t = 1.2$ s. Finally, the slowing down of the reaction wheel from $t = 3 - 5$ s is a representation of the system trying to correct for the error, but having no effect due to the friction in the bearing. This can be seen in Fig. 58 as a lack of movement in the yaw orientation.

Fig. 60 shows the current consumption of the prototype platform. Not surprisingly, the current consumption curve resembles the rotation rate curve. This is due to the relationship

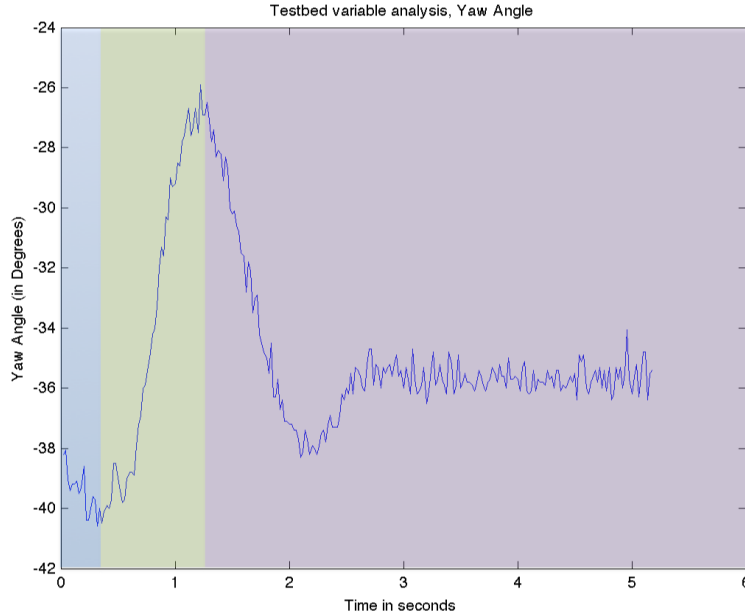


Figure 58: Experiment results showing the yaw orientation of the the testbed in response to a 14° disturbance input. The results show a steady state error of 2° .

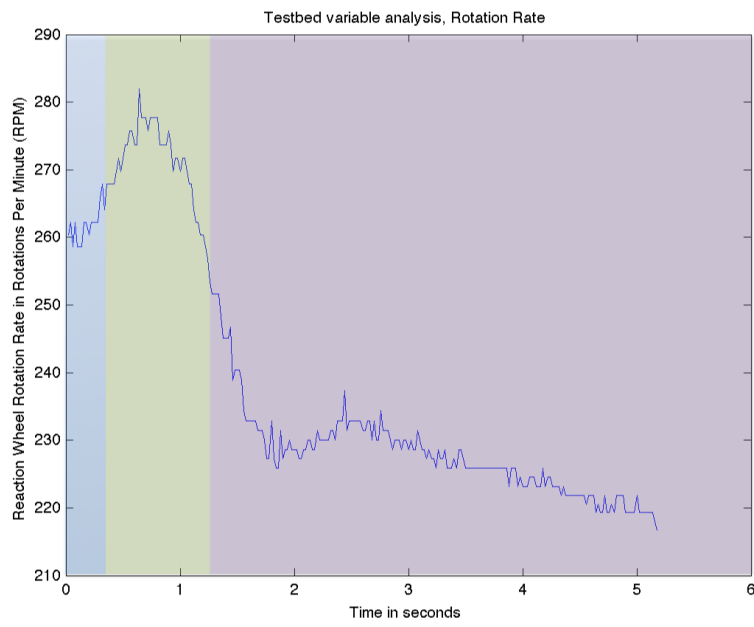


Figure 59: Experiment results showing the motor angular velocity showing that the motor is constantly decreasing in speed trying to reduce the steady state error to zero.

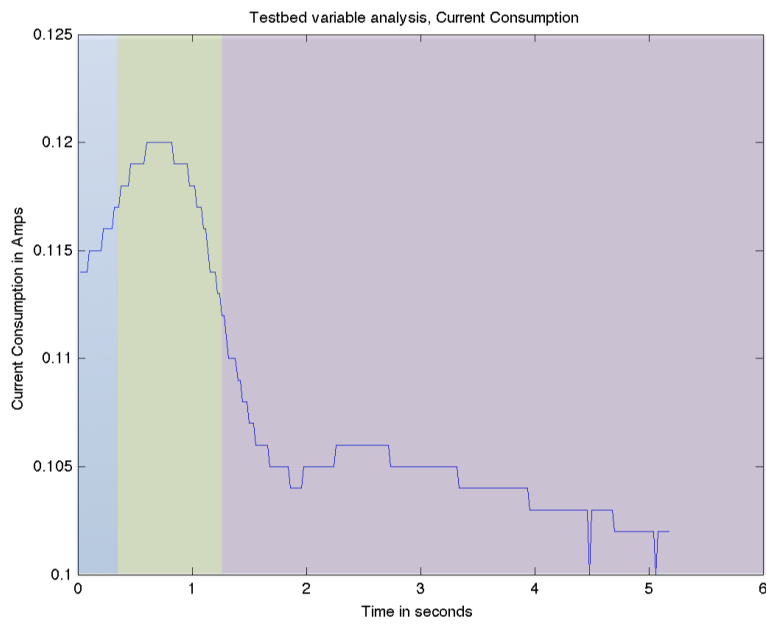


Figure 60: Experiment results showing the motor current consumption which resembles the motor speed curve. From the diagram it can be seen that the motor is operating well below its maximum rating (23A)

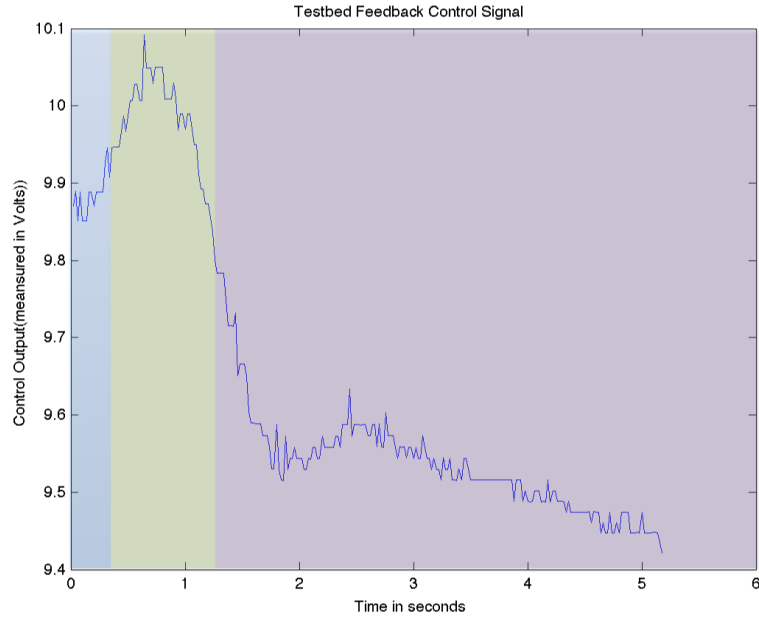


Figure 61: Experiment results showing the feedback control signal commanded by the micro-controller. Similar to Fig. 59 - 60, it can be seen that the controller is trying to slow down the motor to reduce the steady state error.

between the speed of the reaction wheel and the current applied to the system. Observing each of the figures, it is evident that each variable is operating within its acceptable parameters. The yaw orientation has no sharp spikes indicating sensor interference or numerical errors in the attitude estimator, also the angular velocity of the motor is well within its limit of 6710RPM. It is also important to notice the similarities between the angular velocity and current consumption plots, the similarity between these two plots indicates proper control of the BLDC motor. If the motor were being commutated incorrectly discrepancies would arise between the two curves. Also, the current consumption curve is well below the limits of the motor and motor driver's maximum rating. This shows that long term operations of the system should be sustainable.

Using the data found in Fig. 58 - 60, the system control signal was reconstructed and depicted in Fig. 61. The control signal is composed of a control offset of 6.6V and the additive feedback control signal. Fig. 61 shows a very small change ($\sim \frac{1}{2}V$). In the control output, this is to be expected as the control gains are extremely low, as seen in Eq. 31. Observing the control output in Fig. 61 and the wheel speed and current consumption found in Fig. 59 and 60, it can be seen that the control output resembles the wheel speed and current consumption. Fig. 59 and

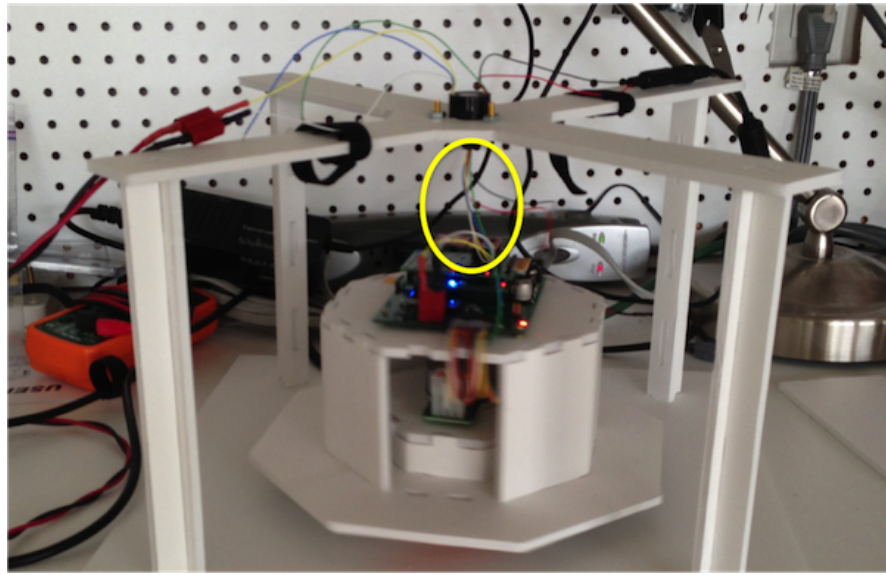


Figure 62: Image of the testbed showing the slip ring and wires in yellow connected to the control hardware. The slip ring and wires cause the steady state error on the testbed.

61 shows that over time the reaction wheel will continue to slow down due to the accumulated error.

A deadband was also added to the control algorithm to suppress vibrations from the motor causing the testbed to drift. The drift would then create an error between the desired angle and the measured angle causing the feedback controller to constantly readjust the output. Another issue was the static friction due to the slip ring (see Fig. 62) which was too great for the motor to overcome, preventing the testbed from rotating when the torque was not sufficient. It was found experimentally that a 4° deadband worked well. It should be stated that this problem is an aspect of the testbed and will not be an issue in space applications, the deadband was only necessary for ground testing.

It has been demonstrated that the control hardware was able to control and regulate the yaw orientation of the testbed. It will be left for future works to conform to the accuracy requirement of $\leq 1^\circ$. Proper evaluation of the control accuracy requires the use of an air bearing and use of the Faulhaber 1509 Big Wheel.

7 Conclusions & Future Work

7.1 Conclusions

Over the past decade, many CubeSat projects have been deployed, giving universities the opportunity to conduct space experiments. One such example is the GeneSat-1 project, which tested the effects of microgravity and solar radiation on E. Coli bacteria [73]. Without small satellites, tests like these would have to be placed on larger satellites or on the International Space Station (ISS). So only a limited number of tests would be performed. However, CubeSats offer a flexible research platform at a significantly reduced cost.

The development of a prototype Attitude Estimator and Control System (AECS) hardware was designed to demonstrate control of a reaction wheel based CubeSat Attitude Control System . A reaction wheel were chosen to increase the accuracy and the control torque available to CubeSat project. Increased accuracy allows CubeSat missions to perform more complex tasks and more accurately orient the solar panels with the Sun's rays. This becomes a huge advantage over passive systems which cannot alter their orientation. Reaction wheels provide a greater amount of torque than other available CubeSat actuations systems allowing for faster maneuvering and increased capability to handle environmental disturbances.

The hardware developed here had to conform to the strict size constraints of a 3U CubeSat, limiting the available space for the reaction wheels and control electronics. The control electronics were designed to conform to the mission's specific objectives by using shields to add and remove mission specific hardware. This allows for easy manipulation of the footprint of the control electronics.

A mockup of the reaction wheels was also designed but not built due to limitations in the fabrication tools and materials. These mockups was designed to fit within a 1U CubeSat to evaluate the amount of room available for the control hardware. Since the reaction wheels were not fabricated, a substitute motor was chosen to evaluate the hardware due to its built in momentum wheel. The Maxon EC45 motor was implemented on the testbed for proof of concept.

During testing a control accuracy of 4° was obtained. However, it is estimated that a theoretical maximum accuracy of 1° is possible due to the accuracy of the attitude estimator. The limited accuracy in the testbed was a result of friction that would not be present in a real

space system. The flight control hardware was also able to conform to the power and volume criteria specified. It was estimated that the developed hardware can operate on 4.9W leaving 15W for the payload if the Clyde Space Solar Panel System is employed [54]. In designing the flight control hardware, a system prototype was created that demonstrated the functionality of the system, while leaving room for expandability and flexibility for adaptations to other autonomous platforms.

7.2 Future Work

This work represents a very early prototype in CubeSat attitude estimation and control, using a reaction wheel system. As such, many parts of the design need a great deal of further work to bring them closer to one ready for deployment on a CubeSat mission. In order to develop the flight control hardware into a finished product, some improvements and alterations should be made. Section 6: Evaluation stated that the volume and power design criteria was feasible, but the control accuracy criteria was not achieved. This is because it was not possible to properly model the testbed, which makes it impossible to accurately evaluate the system control gains. For this reason, future efforts should focus on two key areas: improved modeling of the testbed and construction of the testbed itself.

Improvements to the system model will allow for a better understanding of the system response and the use of more modern control techniques. Additionally, improvements on the system testbed would improve the testing and could possibly remove the need for a more complex control methods. A key feature of an improved testbed would be removal of the slip ring. By using a better testbed, the size of the motors being used and the precision of the system can be better evaluated. Air bearings should ideally be considered to reduce the amount of friction between the rotating axes and the testbed. Using a three axis air bearing also allows for further testing, allowing the user to accurately demonstrate actuation in the roll and pitch axes along with the yaw axis.

Before the AECS can be finalized several other aspects of the design must be evaluated. However, due to the limitations of the manufacturing tools and materials, it was not possible to fabricate the actuator structure or momentum wheels.; as a consequence, the mass and structural integrity of the mechanical structure still need to be evaluated.

Thorough stress testing is also necessary. The structural integrity needs to be evaluated

to verify that no structural damage will be incurred while launching the CubeSat. Once the structure and the momentum wheels have been fabricated, shaker testing can be used to simulate the loads incurred during takeoff. The shaker testing is used primarily to evaluate the strength of the shaft holding the momentum wheel in place. Due to the large size of the momentum wheel the tolerances for the momentum wheels are very tight and a slight bend in the momentum wheel shaft could jam the reaction wheels, introducing unwanted disturbances or failures into the control system.

With the momentum wheels fabricated, the output torques can be evaluated. The values of the torque generated by the actuators presented in this thesis are all a gross estimate; much more actual testing would be required before deployment. Testing the torque generated by the reaction wheels requires the use of a air bearing platform, allowing for unrestricted movement in all three axes and removal of the static friction found in the current testbed.

Improvements also need to be made on the attitude control software. The attitude estimation software uses floating point arithmetic to calculate the attitude of the testbed. This hinders the system and takes between 6.5 to 9ms to evaluate. The attitude control algorithm updates every 20ms, which means that about half of the evaluation time is being used to evaluate the attitude. This is not an issue for the current attitude control system. However, if more sophisticated attitude control systems are to be implemented then steps need to be taken to optimize the computation. The progress on the control hardware made thus far provides a solid foundation towards creating a complete CubeSat attitude estimation and control system.

8 Appendix

8.1 AECS Pin Allocation

Table 10: AECS's Pin Allocation

Pin Number	Pin Name	Functions	CONTROL DSC	SENSOR DSC
1	RB9	RP41		
2	RC6	RP54	UART1 RX	UART1 RX
3	RC7	RP55	UART1 TX	UART1 TX
4	RC8	RP56		
5	RC9	RP57		
6	V_{ss}	Power		
7	V_{cap}	Power		
8	RB10	RP42	PWM3H	
9	RB11	RP43	PWM3L	
10	RB12	RPI44	PWM2H	
11	RB13	RPI45	PWM2L	
12	RA10			
13	RA7			
14	RB14	RPI46	PWM1H	
15	RB15	RPI47	PWM1L	
16	A_{vss}	Analog Power		
17	A_{vdd}	Analog Power		
18	MCLR	Reset	reset	reset
19	RA0			
20	RA1			
21	RB0	RPI32		
22	RB1	RPI33		
23	RB2	RPI34	PGEC1	PGEC1
24	RB3	RP35	PGED1	PGED1
25	RC0			
26	RC1			
27	RC2			
28	V_{dd}	Power		
29	V_{ss}	Power		
30	RA2		I/O (LED)	I/O (LED)

Pin Number	Pin Name	Functions	CONTROL DSC	SENSOR DSC
31	RA3		I/O (LED)	I/O (LED)
32	RA8	RPI24	SDA2	SDA2
33	RB4	RP36	SCL2	SCL2
34	RA4	RP20	CAN TX	CAN TX
35	RA9	RPI25	CAN RX	CAN RX
36	RC3	RPI51		
37	RC4	RPI52	SDA1	SDA1
38	RC5	RPI53	SCL1	SCL1
39	V_{ss}	Power		
40	V_{dd}	Power		
41	RB5	RP37	I/O (LED)	I/O (LED)
42	RB6	RP38	I/O (LED)	I/O (LED)
43	RB7	RP39	I/O (LED)	I/O (LED)
44	RB8	RP40	I/O (LED)	I/O (LED)

8.2 BLDC Specificaitons

Table 11: EC45Flat Motor Pinout

Pin Number	Connection
Pin 1	Hall Sensor 1
Pin 2	Hall Sensor 2
Pin 3	VDC (4.5 - 18V)
Pin 4	Motor winding 3
Pin 5	Hall Sensor 3
Pin 6	Ground
Pin 7	Motor Winding 1
Pin 8	Motor Winding 2

Table 12: Maxon EC45Flat Summary

Maxon EC45 Flat	Value
Voltage	24 volts
Power	4.44 Watts
Speed	6710 rmp
Torque	82.7 mNm

Table 13: Faulhaber 1509 Summary

Faulhaber 1509	Value
Voltage	12 volts
Power	0.3 Watts
Speed	14,700 rmp
Torque	0.51×10^{-5} mNm

8.3 Experimental Power Consumption

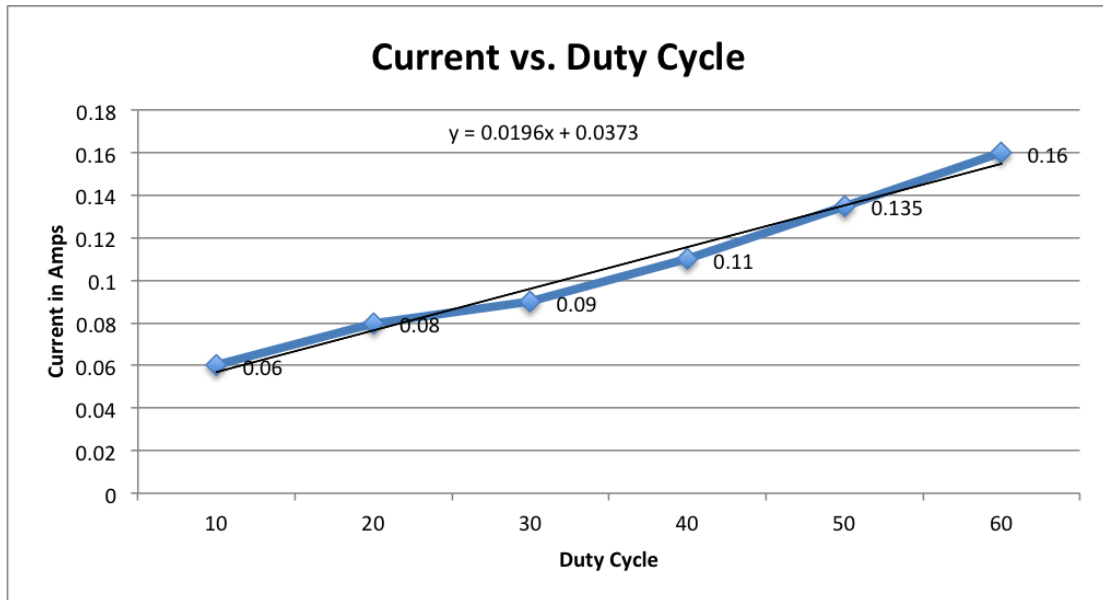


Figure 63: Data comparing the applied duty cycle and the current consumption of the motor.

Nomenclature

General CubeSat Nomenclature

Symbol	Units	Description
1U	$10 \times 10 \times 10\text{cm}^3$	1 Unit for CubeSat
T_{mag}	N.m	magnetic Torque
M	A.m ²	magnetic moment
B	T	magnetic field
V(r)	$\frac{V.s}{m}$	Earth Magnetic Potential
τ	N.m	torque
α	$\frac{rad}{s^2}$	angular acceleration
I	kg m ²	Moment of Inertia
L	N.m.s	angular momentum
ρ	$\frac{kg}{m^3}$	density
\mathcal{L}		Laplace Transform

Attitude Estimation Nomenclature

Symbol	Units	Description
R_i^b		Direction Cosine Matrix
c_i		Inertial Vector
c_b		Body Vector
$\omega(t)$	$\frac{rad}{s}$	rotation rate vector
$\theta(t)$	rad	angle vector
ΔT	s	sample time
ψ	rad	roll
θ	rad	pitch
ϕ	rad	yaw
$k[]$		gain vector
P	W	power
R	ω	resistance
i	A	current
L	H	inductance
b	M.m.s	motor viscous friction
k_t	$\frac{N.m}{A}$	torque constant
k_e	$\frac{V}{rad/s}$	Back EMF constant
ψ_{error}		Yaw Error vector
θ_{error}		Roll and Pitch Error vector

References

- [1] 304/304l stainless steel. Technical report, AK Steel.
- [2] 3d cad design. <http://www.cubesatkit.com/content/design.html>.
- [3] Adxl345 digital accelerometer. Technical report, Analog Devices.
- [4] Arduino. <http://arduino.cc/>.
- [5] Atxmega16a4 datasheet. Technical report, Atmel.
- [6] Cubesat kit - design & cad models. <http://www.cubesatkit.com/content/design.html>.
- [7] Cubesat shop. <http://www.cubesatshop.com>.
- [8] dspic33ep/pic24e family reference manual. Technical report, Microchip Technology Inc.
- [9] Earth centered inertial coordinate system. http://en.m.wikipedia.org/wiki/File:Earth_Centered_Inertial_Coordinate_System.png.
- [10] Geomagnetism. <http://www.ngdc.noaa.gov/geomag/geomag.shtml>.
- [11] Gps module for high altitude unmanned balloon. <http://diydrones.com/forum/topics/gps-module-for-high-altitude>.
- [12] Introduction to orbital propagation library. <http://www.agi.com/resources/help/online/agicomponents/Programmer's%20Guide/Overview/Orbit%20Propagation/OrbitPropagation.html>.
- [13] Phonesat 1.0 and phonesat 2.0 beta satellite technical description. Technical report.
- [14] Reaction wheel. http://www.ssbv.com/resources/Datasheets/SSBV_Reaction_Wheel_Datasheet_1c-.pdf.
- [15] Saleae logic. <http://www.saleae.com/logic/>.
- [16] Spacecraft reaction wheel. http://bluecanyontech.com/all_products/reaction-wheels/.
- [17] Spark fun. <http://www.sparkfun.com>.

- [18] Tiny operationally-responsive cmg. <http://www.honeybeerobotics.com/aeromechanical-systems/12-cmg>.
- [19] Van allen radiation belt. http://en.wikipedia.org/wiki/Van_Allen_radiation_belt.
- [20] Wikipedia. <http://www.wikipedia.org>.
- [21] Space transportation costs: Trends in price per pound to orbit 1990-2000. Technical report, Rutron Corporation, September 2002.
- [22] dspic30f math library. Technical report, Microchip Technology Inc., 2004.
- [23] dspic33fj datasheet. Technical report, Microchip Technology Inc., 2009-2012.
- [24] Three phase pwm motor driver. Technical report, Texas Instruments, May 2010.
- [25] Team jatayu. <http://teamjatayu.blogspot.com/2011/10/advent-of-ardupilot.html>, October 2011.
- [26] dspic33ep datasheet. Technical report, Microchip Technology Inc., 2011-2012.
- [27] Cubesat developers' workshop. Cal Poly, San Luis Obispo, August 2012.
- [28] Arsov rc technology. http://arsovtech.com/?page_id=20, March 2013.
- [29] Atlas v - specifications. www.spaceandtech.com, February 2013.
- [30] Back emf suppression. <http://www.progeny.co.uk/Back-EMF-Suppression.aspx>, March 2013.
- [31] Colony-1. <https://directory.eoportal.org/web/eoportal/satellite-missions/c-missions/colony-1>, February 2013.
- [32] Colony-1. <https://directory.eoportal.org/web/eoportal/satellite-missions/c-missions/colony-1>, February 2013.
- [33] Cubesat-introduction. http://www.triy.org/ENG/CubeSat_Intro.htm, Februrary 2013.
- [34] Diy drones. <http://diydrones.com/>, March 2013.
- [35] Falconsat-7. http://space.skyrocket.de/doc_sdat/falconsat-7.htm, February 2013.

- [36] gentlenav. <http://code.google.com/p/gentlenav/wiki/ProjectStatus>, February 2013.
- [37] Geomagnetism: The magnetic field of the earth. http://nationalatlas.gov/articles/geology/a_geomag.html, January 2013.
- [38] Maxon motors. <http://www.maxonmotorusa.com/maxon/view/content/index>, March 2013.
- [39] Ors, university of hawaii team up on new small satellite launcher. Technical report, February 2013.
- [40] Products and services: Space. <http://www.imicro.biz/space.html>, February 2013.
- [41] Qbx1, 2. http://space.skyrocket.de/doc_sdat/qbx-1.htm, February 2013.
- [42] Sparkfun - ardupilot mega. <https://www.sparkfun.com/products/9710>, February 2013.
- [43] Sparkfun udb4. <https://www.sparkfun.com/products/10582>, February 2013.
- [44] Ucs satellite database. http://www.ucsusa.org/nuclear_weapons_and_global_security/space_weapons/technical_issues/ucs-satellite-database.html, February 2013.
- [45] George Adcock. Uses of reaction wheels on satellites, May 2012.
- [46] Elwood F. Agasid. Phonesat 2.0. Cal Poly, San Luis Obispo, 2012.
- [47] Richard M. Allen. The earth's magnetic field. Lecture.
- [48] Sharan Asundi, Matthew Mahin, Vivek nagabhushan, Tzu Yu Lin, and Norman Fitz-Coy. Composite and pcb based implementations of a solar panel design for swampsat. In 24th Annual AIAA/USU Conference on Small Satellites. University of Florida, 2010.
- [49] Gavrilo Bozovic, Omar Scaglione, Christian Koechli, Muriel Noca, and Yves Perriard. Swisscube: development of an ultra-light and efficient inertial wheel for the attitude control and stabilization of cubesat class satellites. Internation Astronautical Federation (IAF), 2008.
- [50] Ward Brown. Brushless dc motor control made easy. Technical report, Microchip Technology Inc., 2002.

- [51] Bruce Carlson. Nro's historica, current, and potential future use of small satellites. Technical report, National Reconnaissance Office, August 2001.
- [52] Robert Taylor Casey. A comparison of attitude propagation and parameterization methods for low-cost uavs. Master's thesis, UC Santa Cruz, December 2012.
- [53] NDT Resource Center. Measuring magnetic fields. <http://www.ndt-ed.org/EducationResources/CommunityCollege/MagParticle/Physics/Measuring.htm>, March 2013.
- [54] Craig Clark. Off-the-shelf deployable solar panels for cubesats. Cal Poly, San Luis Obispo, 2012.
- [55] Reston Condit. Sensorless bldc control with back-emf filtering. Technical report, Microchip Technology Inc., 2007.
- [56] Diodes Incorporated. 60V N-channel Enhanced Mode MOSFET, rev 4-2 edition, May 2013.
- [57] Jamie Dunn. Determining mosfet driver needs for motor driver applications. Technical report, Microchip Technology Inc., 2003.
- [58] Gabriel Elkaim. Attitude estimation lecture, Spring 2011.
- [59] Mitra Farahmand. Orbital propagators for horizon simulation framework. Master's thesis, California Polytechnic State University, San Luis Obispo, 2009.
- [60] Faulhaber. Brushles flat dc-mircomotors. Technical report, 2011-2012.
- [61] Sanjay Fayaram. Design and analysis of nano momentum wheel for picosatellite attitude control system. Aircraft Engineering and Aerospace Technology: An International Journal, Emerland Group Publishing Limited, 2009.
- [62] Andrew Fleming. Real-time optimal slew maneuver design and control. Master's thesis, Naval Postgraduate School, Monterey California, 2004.
- [63] Laboratory for Atmospheric and Space Physics. <http://lasp.colorado.edu/home/csswe/>.

- [64] David T. Gerhardt and Scott E. Palo. Passive magnetic attitude control for cubesat space-craft. In 24th Annual AIAA/USU Conference on Small Satellites. University of Colorado, Boulder, 2010.
- [65] Douglas C. Giancoli. Physics for Scientist & Engineers. Prentice Hall, 3 edition, 2005.
- [66] Allan R. Hambley. Electrical Engineering Principles and Applications, volume 4. Prentice Hall, 2008.
- [67] Brian Howley. Aa236: Overview of spacecraft attitude determination and control. Lockheed martin.
- [68] Robert Twiggs Isaac Nason, Jordi Puig-Suari. Development of a family of picosatellite deployer based on the cubesat standard. volume 1, pages 1–457. Aerospace Conference Proceedings, 2002. IEEE.
- [69] Andrew E. Kalman. Pumpkin’s colony i cubesat bus: Past, present and future. Presentation.
- [70] M. A. Karami. Spacecraft momentum dumping using less than three external control torques. University of British Columbia, Vancouver, Systems, Man and Cybernetics IEEE, October 2007.
- [71] Safa O. Kasap. Principles of Electronic Materials and Devices. McGraw-Hill, 3 edition, 2003.
- [72] Lubin Kerhuel. Simulink - embedded target for pic. http://www.kerhuel.eu/wiki/Simulink_-_Embedded_Target_for_PIC.
- [73] Eric Lee. *.sat & genesat-1 overview. In AIAA/USU Conference on Small Satellites, August 2004.
- [74] Shiyoung Lee and Tom Lemlery. A comparison study of the commutation methods for the three-phase permanent magnet brushless dc motor. Technical report, Pennsylvania State University and Moog Inc.
- [75] Jim Lepkowski. Motor control sensor feedback circuits. Technical Report AN894, Microchip Technology Inc., 2003.

- [76] Dr. Walter Lewin. 24: Rolling motion, gyroscopes. <http://ocw.mit.edu/courses/physics/8-01-physics-i-classical-mechanics-fall-1999/video-lectures/lecture-24/>, November 1999.
- [77] Mariano Lizarraga, Ren Curry, and Gabriel Elkaim. Reprogrammable uav autopilot system (part 1) - system hardware and software. *Circuit Cellar*, 249(24-35), April 2011.
- [78] Mariano Lizarraga, Ren Curry, and Gabriel Elkaim. Reprogrammable uav autopilot system (part 2) - testing and results. *Circuit Cellar*, 250:36–46, May 2011.
- [79] Mariano Lizarraga, Ren Curry, Gabriel Elkaim, and Isaac Kaminer Vladimir Dobrokhodov. Design, Implementation and flight verification of a versatile and rapidly reconfigurable UAV GNC reach platform. PhD thesis, UC Santa Cruz, 1156 High St Santa Cruz, CA 95064, December 2009.
- [80] Robert Mahony, Sung-Han Cha, and Tarek Hamel. A coupled estimation and control analysis for attitude stabilisation of mini aerial vehicles. November 2006.
- [81] Michael. Michael's list of cubesat satellite missions. <http://mtech.dk/thomsen/space/cubesat.php>, September 2005.
- [82] EDN Network. Brushless dc motors – part i: Construction and operating principles. <http://www.edn.com/design/sensors/4406682/Brushless-DC-Motors---Part-I---Construction-and-Operating-Principles>.
- [83] Espen Oland and Rune Schlanbusch. Reaction wheel design for cubesat. Narvik Norway, 2009. Narvik University College, Institute of Electrical and Electronics Engineers (IEEE).
- [84] Sithambaran Palaniappan. Commutation of a bldc motor with various pole-paris can be simplified by using absolute encoder feedback. Technical report, Avago Technologies, Malaysia, 2010.
- [85] J. Peraire. Lecture d14 - accelerometers. newtonian relativity.
- [86] William Premerlani and Paul Bizard. Direction cosine matrix imu: Theory. May 2009.
- [87] Li Qiao, Chris Rizos, and Andrew G. Dempster. Analysis and comparison of cubesat lifetime. Technical report, University of New South Wales, Sydney.

- [88] Sharing Earth Observation Resources. Satellite missions database. <https://directory.eoportal.org/web/eoportal/satellite-missions>.
- [89] Paul G Savage. What do accelerometers measure. Technical report, StrapdownAssociates, Inc., 2005.
- [90] Chester Simpson. Linear and switching voltage regulator fundamentals. Technical report, National Semiconductor.
- [91] Kristian Svartveit. Attitude determination of the ncube satellite. Master's thesis, Norwegian University of Science and Technology, June 2003.
- [92] Berlin Space Technologies. Star tracker st-200. <http://www.berlin-space-tech.com/index.php?id=42>.
- [93] USASMDC. Kestrel eye. <http://www.smdc.army.mil/FactSheets/KestrelEye.pdf>.
- [94] Ronny Votel and Doug Sinclair. Comparison of control moment gyros and reaction wheels for small earth-observing satellites. In 26th Annual AIAA/USU Conference on Small Satellites, volume SSC12-X-1. Skybox Imaging, Inc and Sinclair Interplanetary, 2012.
- [95] Jim Williams. Step-down switching regulators. Technical report, Linear Technology.
- [96] Padmaraja Yedamale. Brushless dc (bldc) motor fundamentals. Technical Report AN885.